
Few-cycle phase-stable infrared OPCPA

Alexander Hermann Schwarz



Garching bei München 2014

Few-cycle phase-stable infrared OPCPA

Alexander Hermann Schwarz

Dissertation
an der Fakultät für Physik
der Ludwig–Maximilians–Universität
München

vorgelegt von
Alexander Hermann Schwarz
aus Schrobenhausen

München, den 30. April 2014

Erstgutachter: Prof. Dr. Ferenc Krausz

Zweitgutachter: Prof. Dr. Eberhard Riedle

Tag der mündlichen Prüfung: 16. Juli 2014

Contents

List of Figures	xi
List of Tables	xiii
Abstract	xv
Introduction	1
List of publications by the author	7
1 Theoretical foundations of OPCPA	9
1.1 Ultrafast optics	9
1.1.1 Mode-locked oscillators	9
1.1.2 Ultrafast pulses	12
1.2 Nonlinear optics	14
1.2.1 Second order processes	14
1.2.2 Phase-matching	17
1.2.3 Higher order processes	19
1.2.4 OPCPA	22
2 Seeding OPCPA	23
2.1 The seed laser	23
2.2 Spectral broadening for seeding ultrabroadband OPCPA	26
2.2.1 Spectral broadening by filamentation	26
2.2.2 Spectral broadening in a hollow core fiber	27
2.3 Compression and characterization of the broadened spectra	29
2.4 Phase-stable infrared seed generation	31
2.4.1 DFG using PPLN	31
2.4.2 DFG using BBO	35
3 Pumping OPCPA	39
3.1 Pump laser for OPCPA	40
3.1.1 Motivation of the thin-disk concept for pumping OPCPA	40
3.1.2 Pump laser setup	40

3.1.3	Chaotic behavior of cw pumped regenerative amplifiers	43
3.2	Short characterization of the pump laser	44
3.2.1	Consequences of high B-integral	44
3.2.2	Beam profiles, M^2	47
3.2.3	Beam pointing	49
4	Synchronizing OPCPA	51
4.1	Electronic synchronization	51
4.1.1	Timing hardware used	51
4.1.2	Seed laser	52
4.1.3	Pump laser	52
4.2	Dazzler (AOPDF)	53
4.2.1	Electronic triggering	53
4.2.2	Dispersion calibration	54
4.2.3	CEP control	55
4.3	Optical synchronization	56
4.3.1	Setup	56
4.3.2	Limits of optical synchronization	57
4.3.3	Measuring technique	58
4.3.4	Software-based feedback loop	59
4.3.5	Hardware-based feedback loop	62
4.3.6	In-loop and out-of-loop performance	65
4.3.7	Conclusions and outlook	67
5	Building an infrared few-cycle OPCPA	71
5.1	Overview	71
5.2	Stretching	71
5.3	Amplification	74
5.4	Compression	77
5.5	CEP characterization	81
6	First prototype experiment: controlling currents in a dielectric using IR few-cycle pulses	85
6.1	Current control theory	85
6.2	Experimental setup	87
6.3	Experiment	89
6.4	Discussion and conclusions	91
7	Generation of phase-stable continua spanning three octaves	93
7.1	Motivation for super-octave spectra centered in the NIR	93
7.2	Boosting the OPCPA output to mJ level	94
7.2.1	Broadband amplification using bulk lithium niobate	94
7.2.2	Narrow band amplification for more efficient super-octave generation	98

7.3	Indications of spectral broadening in the NIR	99
7.3.1	Onset of THG	99
7.3.2	Onset of fifth harmonic and blue white light	100
7.4	Generation of a super-octave continuum	101
7.4.1	Experimental setup	101
7.4.2	Issues with beam profile	101
7.4.3	Increasing the pressure	102
7.4.4	Phase stability	104
7.4.5	Pulse characterization	105
7.4.6	Brief results in a filament and differences	106
7.4.7	Discussion and conclusions	108
Conclusions and Outlook		112
A Used Acronyms		117
B Optics used in the manuscript		119
B.1	Linear and nonlinear materials	119
B.2	NIR filters	120
B.3	Silicon compressor	121
C Calibration		123
C.1	Calibration of PSDs	123
C.2	Spectrometer calibration procedure	124
C.2.1	Additional diagnostics	124
D Self-diffraction in QPM OPCPA		125
Data archiving		127
Bibliography		129
Acknowledgments		138
Curriculum Vitae of the author		141

List of Figures

1	Overview of MS (illustration)	6
1.1	DFG seed generation (illustration)	12
1.2	Coupled wave equations (OPACWEpic)	16
1.3	OPA gain (OPCAgainspectrumpic)	18
2.1	Seed generation (illustration)	24
2.2	FROG of seed amplifier (frogfp2pic)	24
2.3	Beam pointing of seed amplifier (fp2beampointingpic)	25
2.4	Spectrum of filamentation (filamentspectrumpic)	27
2.5	Spectrum of HCF (HCFplot)	28
2.6	XFROG of filament and HCF (XFROGpic)	30
2.7	Stability of PPLN DFG signal (instabilityofDFG)	32
2.8	Interference between DFG and SPM (spmdfgbeating)	33
2.9	DFG signal and distortion (dfgsignalanddistortion)	34
2.10	XFROG of PPLN DFG (PPLNDFGXFROG)	35
2.11	BBO DFG output (BBODFGXFROG,BBODFGBEAM)	36
2.12	f - $2f$ BBO DFG (BBODFGf-2f)	37
3.1	Pump laser scheme (illustration)	41
3.2	Buildup in cavity (diskpulsebuildup)	42
3.3	The Route to chaos (illustration)	43
3.4	Bifurcation of pulse energy (bifurcationpic)	44
3.5	FROG of pump laser (disklaserFROG)	46
3.6	Beam profiles pump laser (beamprofilesdisklaserpic)	48
3.7	M^2 measurement of pump laser (m2measurementpic)	49
3.8	Beam pointing of pump laser (diskbeampointingpic1)	50
4.1	Electronic synchronization (illustration)	52
4.2	Effect of electronic jitter (DazzlerPLL)	54
4.3	GD compensation (DazzlerSI)	55
4.4	CEP modulation with AOPDF (DazzlerCEP)	56
4.5	Optical synchronization (illustration)	57
4.6	Jitter measurement method (illustration)	59

4.7	Setup PC-based synchronization (illustration)	60
4.8	Long-term drift (slowdriftpic)	60
4.9	Timing jitter using PC (LVjitterpic)	62
4.10	Hardware based synchronization (illustration)	63
4.11	Temporal jitter on PSD (jitterpsd)	65
4.12	FFT of timing jitter (jitterpsdfft)	66
4.13	Out-of-loop jitter setup (illustration)	67
4.14	Out-of-loop timing jitter (externalandinternal)	68
5.1	OPCPA setup (illustration)	72
5.2	XFROG of chirped seed (chirpedXFROG)	73
5.3	Beam profile seed (1ststageseed)	74
5.4	Pump and output of first stage (1ststagepump,1ststageoutput)	75
5.5	Pump profile second stage, OPCPA spectra (2ndstagepump, OPCPAspec)	76
5.6	XFROG of compressed OPCPA (xfrogcompressed)	77
5.7	SH FROG of compressed OPCPA (SHFROG2ndstage)	78
5.8	Phase applied by AOPDF (Dazzlerphase)	80
5.9	CEP of OPCPA with synchronization (f-2fdelaystabon)	83
5.10	CEP of OPCPA without synchronization (f-2fdelaystaboff)	84
6.1	Setup of Experiment (illustration)	87
6.2	OPCPA focus profile (currentcontrol)	88
6.3	Measured current (currentpic)	89
6.4	Scan over power (currentpowerscan)	91
7.1	Bandwidth of 3rd stage (longandshortopa)	95
7.2	Stability third stage (3rdstagestabilitybeamprofilepic)	96
7.3	Pump and seed profile 3rd stage (3rdstagepumpseed)	97
7.4	SF level 3rd stage (3rdstageSF)	97
7.5	Spectrum of TH (MIRHCFTHFH)	100
7.6	Fifth harmonic (UVbehaviour)	100
7.7	Setup spectral broadening (illustration)	102
7.8	Spectrum over pressure (pressurescan/software_calibration)	103
7.9	Cumulative sum (pressurescan/software_calibration, HCFoutputmodeIR)	103
7.10	CEP of broadened spectrum (HCFMIRf-2f)	104
7.11	SH FROG of broadened spectrum (MIRHCFSHFROG)	106
7.12	XFROG of filament broadening (XFROGIRfilamentpic)	107
7.13	Spectrum of filament broadening (filamentspectrum)	108
B.1	NIR filter transmissions (FEL1500)	120
B.2	Compressor transmissions (siliconcompressor)	121
C.1	PSD calibration (PSDcalibration)	123

D.1 OPA Spectrogram (nicksaturationsimulation)	126
D.2 OPCPA Spectrogram (nicksaturationsimulation)	126

List of Tables

B.1	Nonlinear materials	119
B.2	Linear optical media	120

Abstract

Few-cycle laser pulses are an important tool for investigating laser-matter interactions. Apart from the mere resolution used in time-resolved processes, owing to this approach table-top sources nowadays can reach the limits of the perturbative regime and therewith enable extreme nonlinear optics. In the visible domain, femtosecond technology over the last decades has quickly developed, in recent years leading to the routine generation of carrier-envelope phase (CEP) stable few-cycle laser pulses at high energies, using ubiquitous Ti:Sapphire amplifiers.

Near to mid-infrared few-cycle pulses in contrast can be employed for investigating interactions in the tunneling regime. The ponderomotive potential of the infrared light field allows quivered charged particles to acquire large energies, leading to applications like the generation of isolated attosecond pulses in the water window. In this wavelength regime however, the required sources are yet to be demonstrated or at least matured. The best candidate for few-cycle pulses in this domain is optical parametric amplification.

This work describes the development of an optical parametric chirped pulse amplifier (OPCPA), used to create CEP-stable few-cycle pulses in the near infrared (NIR).

It covers all essential parts of the system. First the signal pulses are generated from ultrashort lasers using spectral broadening techniques in chapter 2. After compression of these white light continua, intra-pulse broadband difference frequency generation yields CEP stable infrared pulses spanning over more than one octave.

A thin-disk-based pump laser provides ample pump energy (20 mJ) at pulse durations around 1.5 ps. Its characterization and optimization for OPCPA is performed in chapter 3. The high peak energy of this pump laser leads to the buildup of optical nonlinearities and consequently shows distinct influence on the OPCPA system performance.

The synchronization of the OPCPA pump and seed laser system is the topic of chapter 4. This chapter is not limited to NIR systems, but demonstrates enhanced (actively stabilized) synchronization of the jitter between pump and seed pulses to $\sigma = 24$ fs, which later results in improved output stability.

The NIR OPCPA centered at $2.1 \mu\text{m}$ is described in chapter 5. This combines the efforts of the previous chapters and describes the generation and characterization of $100 \mu\text{J}$ sub-two-cycle CEP-stable pulses, the shortest published to date at this energy level.

As a first prototype (cutting edge) experiment, CEP dependent sub-fs currents in a dielectric are generated in chapter 6 using the developed light source. The results compared well to visible few-cycle laser sources and demonstrate the usability of the OPCPA system (beyond the characterizations of chapter 5) for investigating sub-cycle carrier dynamics in dielectrics.

For the same purpose, to generate the currently most broadband NIR continua at kHz repetition rates and mJ-level pulse energies, the OPCPA system is further boosted and efficiently broadened to three optical octaves using a hollow core fiber setup (described in chapter 7). The spectral phase is characterized and demonstrates self-compression in the NIR around $1.3\ \mu\text{m}$. The process provides CEP-stable sub-2-cycle pulses in this regime directly, the shortest and most powerful reported to date.

Furthermore, the spectral broadening in the infrared shows enhanced low-order harmonic generation and cross-phase-modulation as the dominant mechanism. Experimentally the limited influence on the driver bandwidth is investigated. It is found that the processes allow using more efficient many-cycle infrared sources to generate several-octave spanning, compressible continua in the future. Even partial compression of these would then provide NIR transients for high-field experiments.

Zusammenfassung

Die Femtosekunden-Technologie hat sich in den letzten Jahrzehnten schnell fortentwickelt, vor allem im sichtbaren Wellenlängen-Bereich. Speziell moderne Titanium-Saphir Verstärker haben zuletzt zu (Träger-Einhüllenden-) phasenstabilen und hochenergetischen Laserpulsen geführt, die nur noch aus einzelnen optischen Zyklen bestehen. Diese erlauben die Investigation extrem nichtlinearer optischer Prozesse im Regime der Multiphotonenionisation.

Um weiter im Infraroten Prozesse im Regime der Tunnelionisation zu untersuchen, fehlt es jedoch nach wie vor an Lichtquellen mit ähnlichen Charakteristiken für Anwendungen wie die Generation von isolierten Attosekunden-Pulsen im Wasser-Transmissions-Fenster. Hier bietet die optische parametrische Verstärkung bisher die größten Perspektiven.

Diese Arbeit beschäftigt sich mit der Entwicklung eines optischen parametrischen Verstärkers mit gestreckten Pulsen (engl.: optical parametric chirped pulse amplifier, OPCPA), der TE-phasen-stabile Pulse mit wenigen optischen Zyklen im nahen Infraroten erzeugt.

Alle wesentlichen Teile des Systems werden beschrieben. Zuerst wird der Saat-Puls durch die spektrale Verbreiterung eines Titanium-Saphir Verstärkers gewonnen. Nach der Kompression des generierten Weißlichts führt die breitbandige Differenz-Frequenz-Generation (DFG) des Pulses mit sich selbst zu TE-phasen-stabilen Infrarot-Pulsen, deren Spektrum mehr als eine optische Oktave aufspannt.

Ein Scheiben-Laser liefert die Pumpenergie (20 mJ) bei einer Pulsdauer von ca. 1.5 ps. Seine Charakterisierung und Optimierung für die OPCPA erfolgt in Kapitel 3. Die hohen Spitzenintensitäten dieses Pumpasers führen zum Akkumulieren optischer Nichtlinearitäten und beeinflussen die OPCPA im Folgenden negativ.

Die Synchronisation von OPCPA Pump- und Saat-Lasern ist das Thema von Kapitel 4. Es demonstriert eine aktive Stabilisierung des zeitlichen Überlapps beider Pulse, der den gesamten Prozess im Folgenden stabilisiert, und ist nicht auf den Einsatz im Infraroten beschränkt, sondern für die meisten OPCPA Systeme anwendbar.

Die in Kapitel 5 beschriebene infrarote OPCPA hat ihre Zentralwellenlänge bei $2.1 \mu\text{m}$ und baut auf den vorherigen Kapiteln auf. Die Erzeugung und Charakterisierung von Pulsen mit weniger als zwei optischen Zyklen, den bisher kürzesten in diesem Wellenlängen-Bereich und einer Energie von $100 \mu\text{J}$, werden beschrieben. Ferner erweist sich die TE-Phase der verstärkten Pulse

als außerordentlich kurz- und langzeitstabil.

Kapitel 6 demonstriert dann die Möglichkeiten des neuen Systems mit einem technisch anspruchsvollen Experiment. TE-phasen-abhängige Ströme mit einer Lebenszeit auf der Skala von Attosekunden werden in einem Dielektrikum erzeugt und gemessen. Die Resultate stimmen gut mit den bereits gemessenen Werten im sichtbaren Bereich überein und demonstrieren die Möglichkeiten und Einsetzbarkeit des Systems.

Für ähnliche Anwendungen, allerdings bei noch höheren Intensitäten, wird in Kapitel 7 das OPCPA-System weiter verstärkt. Die spektrale Verbreiterung in einer gas-gefüllten Hohlleiter erzeugt ein Kontinuum über drei optische Oktaven. Dessen spektrale Phase wird im Folgenden charakterisiert und zeigt Selbstkompression bei einer Wellenlänge von $1.3 \mu\text{m}$. Der Prozess erzeugt TE-phasen-stabile Pulse kürzer also zwei optische Zyklen, welche die kürzesten und intensivsten darstellen, die in diesem Bereich bislang erzeugt wurden.

Weiterhin zeigt die spektrale Verbreiterung im Infraroten besondere Merkmale. Speziell die Generation von ungeraden Harmonischen niedriger Ordnung und deren Kreuz-Phasen-Modulation zeigen sich als dominante Prozesse, welche den Einfluss der Eingangsbandbreite minimieren. Eine experimentelle Untersuchung demonstriert dann, dass auch potentiell effizientere infrarote OPCPA Systeme mit deutlich längeren Pulsen ähnliche spektrale Bandbreiten erzeugen können. Die Komprimierung dieser sollte in der nahen Zukunft zu Hochfeld-Anwendungen mit infraroten Feldtransienten und synthetisierten elektrischen Feldern mit Sub-Zyklus Merkmalen führen.

Introduction

Applications of phase-stable infrared few-cycle sources

Few-cycle laser pulses have developed into one of the most powerful tools to gain insight into the dynamics of electrons in solids and atoms. However, they are not young as one might expect. In fact, the first pulses below 10 fs were already achieved in 1985 [75] by broadening the spectrum of an amplified dye laser in a single-mode fiber. For modern solid-state Ti:Sapphire technology however, it took until 1995 [130] to obtain equally short pulses, nevertheless this was achieved without the need for extra-cavity self-phase-modulation.

Thanks to the tremendous energy scaling of this technology, the intensities attainable using this approach are over 10^{14} W/cm² and allowed the generation of XUV attosecond pulses in 2001 for the first time [53]. Isolated attosecond pulses are generated by spectral filtering of high harmonic generation (HHG) produced by sub-two-cycle pulses [78]. Relying on the very same approach, nowadays phase-stable, sub-two-cycle sources are routinely employed to generate isolated attosecond pulses, used for time-resolved XUV spectroscopy of electrons from atomic photo-emission [117] and the surfaces of solids [17]. So again, broadening in a fiber after more narrowband amplification proved to be the ultimate solution in short pulse generation. Unfortunately, like in 1985, this approach is not scalable in energy (and power) indefinitely.

One path to higher energy ultra-broadband sources is optical parametric amplification (OPA). In 2002 4 fs pulses were achieved by Baltuska et al. [5] in a non-collinear optical parametric amplifier (NOPA). This early demonstrated the bandwidth potential of OPA. Nowadays, the record for OPA sources is 2.2 fs compressing the second harmonic of the idler of a visible NOPA [95]. This is very close to the shortest visible pulses attained (and published) to date at 2.08 fs using waveform synthesis of a Ti:Sapphire-generated hollow-core-fiber-broadened white light continuum [50]. Furthermore, OPCPA can push not only the bandwidth, but also energy and average power limits by using chirped pulse amplification, no energy storage in the crystal and high gain. Using favorable phase-matching conditions it offers bandwidths of one octave [95, 111] (or even 1.5 octaves [49] using two-color pumping). This allows sub-cycle pulses (in the VIS to NIR) directly out of a scalable laser source when using appropriate waveform synthesis. Nowadays, in the visible regime, energy scaling [54, 120] and field synthesis [50, 104] are obviously more of a challenge than the bare bandwidth to be generated.

Apart from pursuing HHG for actual experiments, attosecond methods [40, 71] are to date the

ultimate pulse characterization methods as they allow the direct reconstruction of the temporal electric field with unmatched bandwidth of up to 1 PHz [71], which trumps low-order nonlinear pulse and phase characterization methods. The downside however, is that they require ample intensity to generate attosecond pulses for their characterization.

While HHG flux can be scaled up with increasing pulse energies [120], the filtered cut-off frequency for isolated attosecond pulses scales as $h\nu_{cutoff} = I_p + 3.17U_p$, where

$$U_p = \frac{e^2 E^2}{4m_e \omega^2} \quad (1)$$

is the ponderomotive energy and I_p is the ionization potential. In order to shift the cut-off towards higher energies, the electric field and wavelength can be scaled. However, simply increasing the fluence with conventional Ti:Sapphire based sources produces a lot of ionization of the noble gas, which was observed as very detrimental to the process. In fact, loss of coherence was observed by mere energy scaling of the attosecond driver, using an OPCPA system around 800 nm [61]. Furthermore, the lack of phase-matching for high energy HHG with these short-wavelength drivers only permits low flux [102, 121].

While pure energy scaling does therefore not appear promising, as $U_p \propto I_L \lambda_L^2$, scaling the wavelength is a method of extending the HHG cut-off to the so-called “water window” between the K-absorption edges of carbon and oxygen (280 eV and 540 eV) [102]. This spectral region is especially attractive for biological samples, since the difference in absorption of water and carbon is large there and results in good contrast for (sub-fs) time-resolved soft X-ray microscopy. Also these highly energetic photons could eventually probe inner shell electron dynamics with few-as precision. The quest for a suitable driver of soft x-ray attosecond pulses however is still ongoing. As much as nature uses the very large trajectories of long-wavelength drivers [102] to gain high photon energies, it punishes them at the same time with a heavily reduced single-atom HHG yield proportional to $\approx \lambda^{-6.5}$ [122]. Only very recently it was shown [102] that this low single-emitter yield could be compensated by scaling of the harmonic emitter density in fiber geometries, as higher photon energies suffer less from re-absorption and ionization of the medium.

To generate isolated attosecond water window XUV pulses, so far no powerful enough sub-two-cycle driver laser was available. As laser crystals with a suitable amplification bandwidth are lacking in the MIR, the pulse durations in this regime generated by conventional lasers are far away from being reduced to a few field cycles. What makes OPA very attractive in this regard are phase-matchable regions in the NIR and MIR, where parametric sources are the only method of gaining broad compressible spectra. Therefore IR OPCPA seems to be the only path to obtain these potential attosecond drivers, at least until attosecond pulses from techniques like coherent wake emission or relativistically oscillating mirrors [51] (and their corresponding driver lasers) are available and matured enough to be suitable for attosecond experiments.

The IR OPCPA approach was also recently confirmed in [102], where an OPCPA source, centered around 3.9 μm yielded significant HHG yield (compared to [121]). However the 6-cycle long pulses led to several attosecond bursts and no isolated attosecond pulses could be generated.

Furthermore the emitted bursts were broadened to femtosecond durations, requiring further lossy attosecond chirped mirrors [47] in order to generate few-as pulses.

An interesting feature discovered in [102] is that IR pulses can self-compress (temporally and spatially) inside the fiber geometry. Since even the most favorable OPA phase-matching schemes are limited to about one octave, the generation of sub-cycle features (also called light-wave engineering) in the NIR and MIR to probe the most delicate electron dynamics requires either synchronization of several OPA sources [59] or further spectral broadening after amplification [50]. While long-wavelength extension of common Ti:Sapphire based sources is limited, long-wavelength drivers were recently shown to be easily expandable down to the UV with well known schemes like filamentation (in gases [68] and solids [124]). Using hollow core fibers, temporal self-compression was observed in chapter 7 as well while broadening our amplified spectra around 2.1 μm to three octaves from MIR to UV. Combined with a target geometry similar to the one used in [102], this should be the ideal driver for isolated attosecond pulses in the soft X-ray regime. Furthermore, after waveform synthesis, it should enable even sub-cycle dynamics to be investigated.

Apart from HHG, there are other highly nonlinear applications that demand few-cycle phase-stable pulses as well. Recently, electrons emitted by a nanoscale tungsten tip were accelerated up to 13 eV [81] using a standard Ti:Sa oscillator. The process showed to be extremely phase-dependent, motivating the use of inherently phase-stabilized sources [19]. Scaling of the wavelength [55] would enable energies of several tens of eV and eventually time-resolved surface science techniques with attosecond temporal and nanometer spatial resolutions.

A tool for not only the observation of electrons but also their control inside solids is the motivation for this manuscript. At the same time ample pulse energy is needed to reach intensity levels allowing for the before-mentioned attosecond-based pulse characterization techniques. After all, controlling the system under investigation first needs perfect control of the light source. As the interesting electron dynamics are expected to happen on a few-femtosecond to attosecond timescale these experiments demand extremely short pulses. In dielectrics and wide-gap semiconductors the possible wavelength-range is however limited to visible and infrared light sources, due to linear and nonlinear absorption processes that would otherwise damage the system under investigation. Generating NIR to MIR electrical fields with sub-cycle control should enable us to push the limits of high-speed metrology [71] and solid-state signal processing [50] towards the petahertz realm.

In this regard, only recently light induced fs-scale current using few-cycle VIS driver pulses was discovered [114]. After being injected into the conduction band of the dielectric, electrons were accelerated by phase-stable sub-two-cycle VIS driving fields. Using higher vector potential sources the electron could gain energies large enough to scatter at the edge of the Brillouin zone. The resulting Bloch oscillations before were only observed in superlattices and optical lattices, as the strong scattering by lattice defects and small lattice constants would have required electrical fields beyond the breakdown threshold. Very recently, infrared few-cycle waveforms enabled systematic studies of Bloch oscillations in bulk solids [116]. Since the dephasing time of these oscillations are up to 10 fs [7] (the electronic wave-packet loses coherence due

to electron-phonon scattering, depending on material parameters), the half-cycle of the driving field should be shorter, dictating IR sub-two-cycle sources. The direction of NIR OPCPA as pursued in this manuscript has led to the generation of sub-two-cycle pulses around $2.1 \mu\text{m}$ (without external broadening). And in chapter 6 this source demonstrates its capability in a first prototypical ultrafast current control experiment.

General broadband OPCPA considerations

Apart from concentrating on the IR domain, also some general employable techniques for broadband OPCPA are demonstrated in this manuscript.

First, to ensure that the generated ultrabroadband (and therefore usually ultrashort) seed pulse can be amplified using a significant pump pulse window, it is usually chirped to a fraction of the pump pulse duration (depending on the total gain, see [91]) in OPCPA. Rare-earth doped high power pump sources exhibit a narrow emission cross section, leading to pulse durations around 1 ps [57, 74, 88, 118]. Gain-narrowing will limit the spectral bandwidth even further in high-gain amplifiers. Generating octave-spanning spectra by SPM with a well-behaved phase is difficult to achieve with such long pulses. For short enough pump laser pulses (typically < 800 fs), sometimes white light continua can be generated [12, 118] directly from the pump source and even frequency converted [55] to cover different spectral regions. For ps-duration pump sources, usually a traditional broadband seed laser (as mentioned above) needs to be synchronized to the OPCPA. This may be achieved by electronically [64] or optically [144] locking two individual oscillators, or by using the same broadband oscillator to seed pump and seed amplifiers simultaneously [62]. The latter approach (in the following called optical synchronization) is an inherently stable and passive technique and does not rely on complicated electronic or optical setups. Therefore it is the method used for the work of this thesis and will be further actively enhanced in chapter 4.

Second, the gain bandwidth for OPA is limited by the crystal thickness, which in turn can be reduced when using larger pump intensities. As the damage intensity of dielectrics grows with shorter pulses (down to the few ps level) [132], the use of few ps pump laser pulses is therefore highly advantageous in this regard. Even shorter pulses would limit the usable pump fluence however. Chapter 3 describes such a high power 1.6 ps regenerative amplifier built for pumping sub-two-cycle OPCPA.

Structure of the thesis

Figure 1 sketches out most of the contents of this thesis. Chapter 1 gives an introduction into few-cycle pulses and OPCPA. Chapter 2 will describe the seed generation of super-octave phase-stable NIR/MIR continua. As their energies are still below the μJ level, further amplification in OPCPA is pursued in the following chapters:

As the pump source is one of the most critical points in OPCPA, chapter 3 will describe the pump laser setup (Yb:YAG thin disk regenerative amplifier in fig. 1), its limitations and how it was applied in pumping OPCPA. As ultrashort pump pulses demand low-jitter synchronization, chapter 4 will cover this topic (synchronization unit in fig. 1). These two chapters lay the groundwork for chapter 5, where the setup of a sub-two-cycle phase-stable IR OPCPA is described. To complete this work, chapter 6 first demonstrates the applicability of this unique light source in a showcase current control experiment (not shown in fig. 1). Finally, in chapter 7 the OPCPA is broadened further to multiple-octave-spanning MIR-NIR-VIS pulses for future light-wave synthesis, opening the door to mJ-level sub-cycle light transients in the IR realm for the first time.

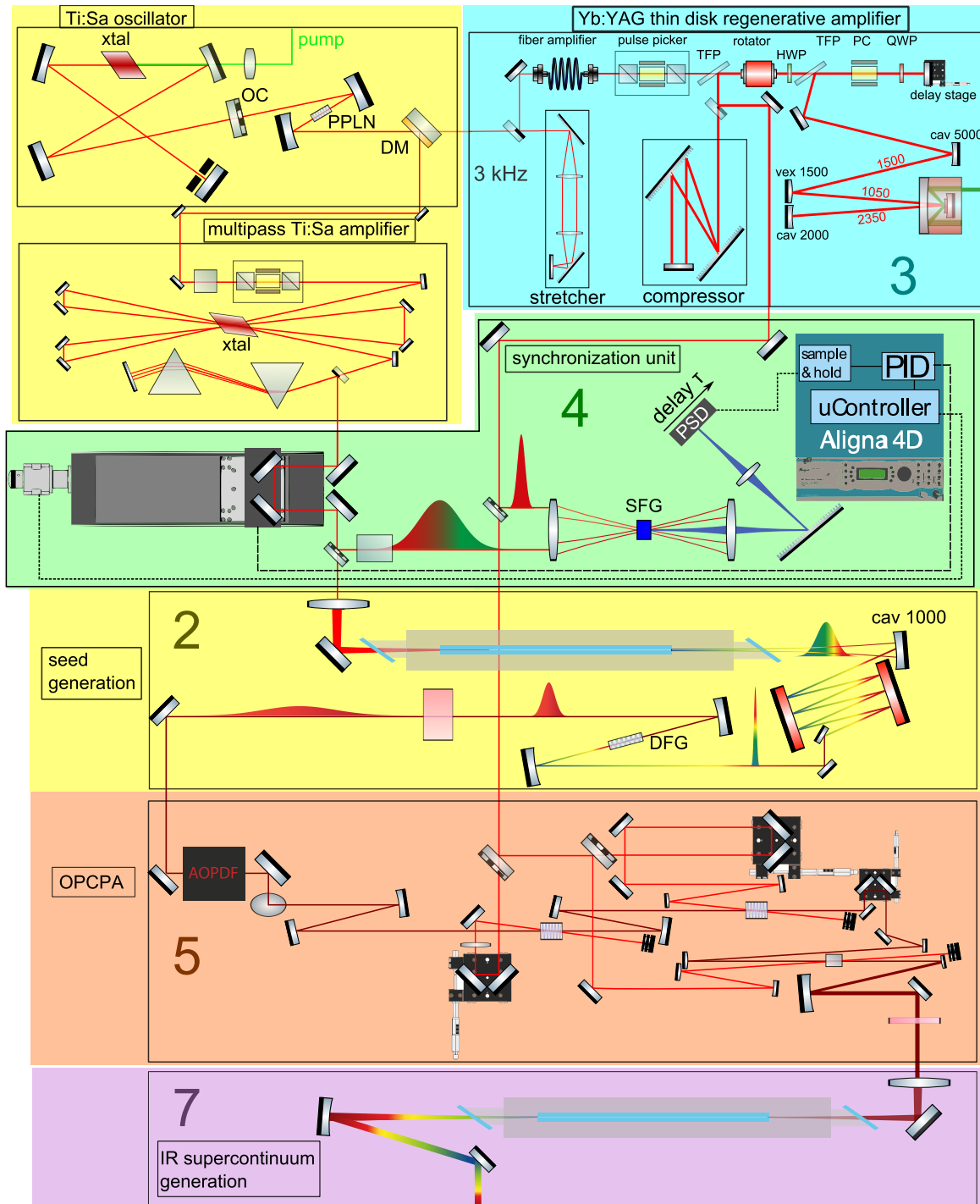


Figure 1: Overview of the manuscript contents, numbers indicate the corresponding chapters.

List of publications by the author

This thesis is based on the following journal papers:

T. Metzger, **A. Schwarz**, C.Y. Teisset, D. Sutter, A. Killi, R. Kienberger und F. Krausz, *Opt. Lett.* **34** (2009), 2123.

Thomas Metzger performed the experimental setup and laser characterization together with me (who joined the project later) and Catherine Teisset (who left the project before), I analyzed measured data, wrote Matlab evaluation scripts and assisted in the preparation of the manuscript.

A. Schwarz, M. Ueffing, Y. Deng, X. Gu, H. Fattahi, T. Metzger, M. Ossiander, F. Krausz und R. Kienberger, *Opt. Express* **20** (2012), 5557

I performed the first experimental measurements for this publication together with Xun Gu. The idea for the synchronization method was devised by me and setup together with Moritz Ueffing in the course of his Diploma thesis [140]. The final characterization of the system for the manuscript was performed by both Moritz and me with the help of other authors. The manuscript itself was prepared by me with the support of Moritz and the other authors.

Y. Deng, **A. Schwarz**, H. Fattahi, M. Ueffing, X. Gu, M. Ossiander, T. Metzger, V. Pervak, H. Ishizuki, T. Taira, T. Kobayashi, G. Marcus, F. Krausz, R. Kienberger und N. Karpowicz, *Opt. Lett.* **37** (2012), 4973.

The experimental work was performed by Yunpei Deng and me together with temporary support of Xun Gu, Gilad Marcus, Moritz Ueffing and Hanieh Fattahi (in chronological order). The data was analyzed by both Yunpei Deng and me and I contributed in the preparation of the manuscript.

The following publication is not in the scope of this thesis:

H. Fattahi, **A. Schwarz**, S. Keiber, and N. Karpowicz, *Opt. Lett.* **38** (2013), 4216.

I assisted in the first experimental work and the preparation of the manuscript. The work is tightly connected with chapter 2, as the principal DFG process is employed there as well. However the focus is not on the topic covered by this publication (type I/II configuration comparison in efficiency), but rather on the spectral phase and amplitude of the DFG spectrum and the carrier

envelope stability, as well as the onset of SPM. Therefore the paper was a by-product of the investigations conducted for chapter 2.

Chapter 1

Theoretical foundations of OPCPA

1.1 Ultrafast optics

1.1.1 Mode-locked oscillators

The fundamental source of all the ultrashort pulses generated, characterized and applied in this manuscript is a mode-locked oscillator. Different kinds of intensity-dependent modulations were developed over the years to force an optical cavity into producing short pulses. Nowadays, Kerr lens mode-locking (KLM) is the fastest mechanism employed, leading (together with Ti:Sa as gain material) to the shortest generated pulses (without extra-cavity spectral broadening) [105] between one and two optical cycles.

What happens in mode-locking is that the cavity modes (defined by the cavity roundtrip time τ_{RT}) are spaced by $\frac{1}{\tau_{RT}}$ and are excited in phase. Now as opposed to CW lasing, where several of these modes are lasing (due to broadening mechanisms of the gain material) in an incoherent fashion (meaning there is not fixed phase relationship between these modes), for mode-locking the phase of the modes on this "frequency comb" are locked together. In Fourier space (time), this then leads to pulses being generated at a repetition rate of $\frac{1}{\tau_{RT}}$.

The emission spectrum of the titanium doped sapphire crystal is extremely broad. It is also called a vibronic medium, since the electronic energy levels of Ti³⁺ couple with the vibrational energy levels of the sapphire host; this is what makes it lase [141]. It allows locking many modes in frequency (from 660 to 1180 nm) and therefore the generation of the shortest pulses (since pulse duration $t_p \propto \frac{1}{2\pi\Delta\nu}$) of any gain material so far. However, the mismatch between supported cavity modes and frequency comb modes (that do lead to a coherent pulse being generated) is given by the dispersion inside the oscillator and that limits the number of modes to be locked. Therefore the broadest bandwidth and consequently shortest pulses are obtained for very low-dispersion oscillators with chirped mirrors in the cavity, like the one employed in section 2.1.

The carrier-envelope-phase (CEP)

The consequence of locking these modes together in the time domain is that an ultrashort pulse is traveling inside the cavity. A part of it is ejected through an output coupler every round trip. Although the pulse needs to retain its duration after every round trip (in order to not cease the mode-locking induced by Kerr-lensing; this mechanism takes care of the soliton-like behavior of the pulse by nonlinear optical effects like self-steepening and self phase modulation), it still experiences material dispersion inside the cavity. This leads to a mismatch between phase experienced by the carrier and envelope of the pulse, effectively changing the shape of the electrical field every round trip, in a manner characterized by the carrier envelope phase. In the frequency domain it is represented by the carrier-envelope offset frequency f_{ceo} , the offset in the frequency comb of the laser modes with respect to zero frequency. To understand this, we have to consider that all generated fundamental continua in the following chapters were derived from amplified mode-locked seed pulses. As mentioned earlier, the process of mode-locking leads to equally spaced cavity modes $f_i = f_{ceo} + if_{rep}$, obviously separated by the inverse repetition rate of the laser (being the time the pulse takes to finish one round trip). Spectra for stable, repetitive pulses need to be not continuous, but actually consist out of (very many) equally spaced frequencies. For CW lasers, the continua would still consist out of cavity modes, but there the mode-spacing is determined by the refractive index at each individual frequency. f_{ceo} is the carrier frequency offset that this so-called frequency comb experiences, given by ([100]):

$$f_{ceo} = \frac{\Delta\phi_{cep} \bmod 2\pi}{2\pi} f_{rep} \quad (1.1)$$

It can assume values from 0 to f_{rep} and leads to the definition of the carrier envelope phase $\Delta\phi_{cep}$, as being the change in carrier envelope phase between two adjacent pulses that is acquired each round trip (during the period $\frac{1}{f_{rep}}$) in the mode-locked oscillator. Therefore each pulse from the pulse-train of the laser has a different CEP, unless actively controlled (i.e. stabilized to $f_{ceo} = 0$). Whereas the absolute phase of the pulse is not interesting (since it is oscillating over propagation anyway), the relative phase between the carrier frequency and the pulse envelope defines the shape of the electric field of the pulse. Note that $\Delta\phi_{cep}$ is a relative value, so both a change in the envelope (with respect to the carrier), for example by dispersion of the pulse, as well as a pure shift of the carrier (without changing the envelope at all, used for example in section 4.2.3) can lead to a CEP shift. This is also obvious in eq. (1.2), where τ is the group delay.

As for short laser pulses the electrical field amplitude is often desired to stay constant for every laser pulse (especially for high fields where the field rather than the envelope becomes the decisive quantity, like in chapter 6), one is interested in locking the carrier envelope phase.

The good news is that the CEP is preserved in typical (laser and OPA) amplification (see eq. (1.16), where the phase of the signal only depends on its initial phase, not on pump or idler phase) and broadening concepts (broadening by self phase modulation does not influence the CEP, when all fields taking part are phase-locked, see eq. (1.22)).

However, thermal effects can cause the CEP to drift slowly. This is why nonlinear interferometers are used to measure and slowly correct this CE shift. We will also see how jitter inside an OPCPA

(section 4.3.2) or beam pointing fluctuations when coupling to a HCF (section 7.4.4) will degrade the phase stability.

The carrier-envelope offset can be measured relatively easy with nonlinear interferometers. Since frequency conversion works on the frequency axis, processes like SHG will exactly double the frequency, therefore also double the CE offset. Whenever components of both (fundamental $I_{FF}(\omega)$ and second harmonic $I_{SH}(\omega)$) frequency combs are interfering (in this f - $2f$ interferometer), the fringes that are visible at a delay τ contain information about the relative CEP $\Delta\phi_{cep}$. This leads to interference for frequencies around ω like given in [19]:

$$I(\omega) = I_{FF}(\omega) + I_{SH}(\omega) + 2\sqrt{I_{FF}(\omega)I_{SH}(\omega)}\cos(\omega\tau + \Delta\phi_{cep}) \quad (1.2)$$

Similarly, one can build f - $3f$ and f - 0 interferometers using THG and DFG. Since the spectral width is not always sufficient for both combs to overlap, there is often another broadening stage integrated into the setup. Furthermore (as illustrated in fig. 1.1), when the input spectral bandwidth reaches one octave, difference frequencies will overlap with fundamental ones. Spectral interference will then lead to beating between both continua (given that their relative CEP is unstabilized) in this f - 0 interferometer, as shown in fig. 2.8 or described in eq. (1.2).

Difference frequency generation (DFG) also allows for a very easy self-stabilization of the CEP; when the pulse mixes with itself, both input frequencies are derived from the same oscillator (and its frequency comb) and consequently the offsets will cancel out for the difference frequency. This is called intra-pulse DFG, whereas inter-pulse DFG can be employed when two synchronized seed pulses (with a CEP relationship) are mixed. The latter one is advantageous when a stronger and less broadband "pump" pulse can be used to achieve more phase-matched bandwidth for the same crystal thickness [55]. Pumping DFG is nothing different from optical parametric amplification (OPA) however, so deriving pump and seed pulses from the same source is equivalent [19]. Intra-pulse DFG however is potentially more stable (as fluctuations of the CEP between two arms are avoided) and much less complicated to set up. Effectively, the DFG process for two waves (pump and signal) with equal phase leads to an idler wave with a CEP of $\pi/2$ [19]. This scheme minimizes the technical effort in generating CEP-stable pulses. Also, it does not require any active locking of the CEP for signal and pump and therefore works with a standard oscillator.

With CEP stability a constant CEP over time (for different pulses of the same pulse train) is meant, as the phase still naturally changes with propagation through any kind of dispersive material. As inherently CEP-stable pulses from DFG do not suffer from limited regulation bandwidths or amplitudes (like active phase-locking schemes), they are potentially able to run stably over infinite periods of time. Every generated pulse has the same CEP with this scheme ($f_{ceo} = 0$ Hz), which is often harder to achieve using active techniques.

The described passive techniques on the other hand allow long-term CEP-stable measurements over virtually unlimited durations (e.g. for the source described in [136], over 21 hours in [30]).

As for any nonlinear process with broadband pulses, the phase-mismatch of fundamental and difference frequency needs to be limited to avoid destructive interference and stay effective.

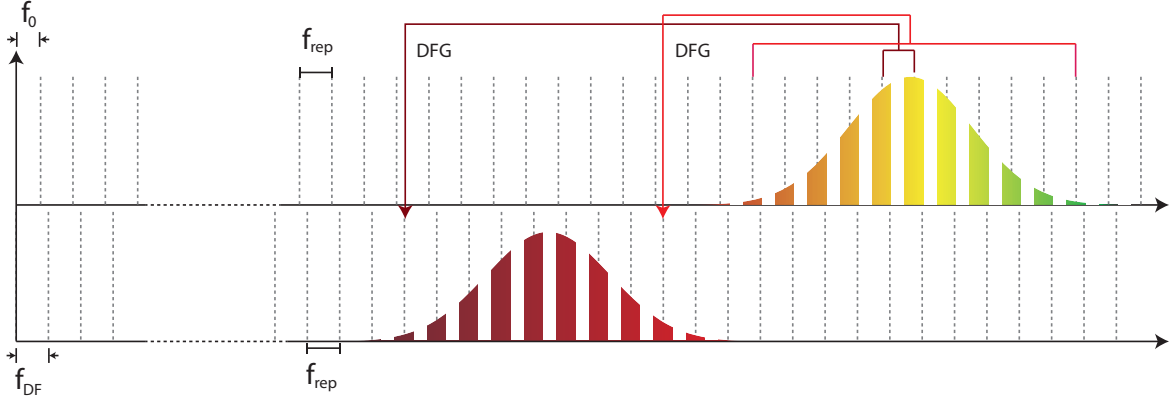


Figure 1.1: DFG seed generation of a broad continuum.

Therefore the DFG process needs to be phase-matched (see section 1.2.2). However for the most broadband seed (and consequently idler) pulses, the group velocity mismatch still limits the efficiency.

1.1.2 Ultrafast pulses

Dispersion

The close-to-compressed pulses inside a mode-locked cavity are stretched by material dispersion as soon as they are coupled out. As the frequency components within the pulse experience different phase velocities, some of them will be delayed with respect to the center frequency. This chirp below the envelope of the pulse can be approximated as the frequency-dependent group delay ($GD(\omega)$). It is a part of the spectral phase $\phi(\omega)$ of the pulse, given by

$$\phi(\omega) = GD(\omega - \omega_0) + \frac{GDD}{2}(\omega - \omega_0)^2 + \frac{TOD}{6}(\omega - \omega_0)^3 + \frac{FOD}{24}(\omega - \omega_0)^4 + \dots \quad (1.3)$$

The constant phase offset (important for the CEP) is neglected here, since it is not of interest in the compression of an optical pulse. Also the GD (which is a constant in eq. (1.3)) is not interesting in this regard, as it only translates the pulse in time. In a frame moving with the traveling pulse, the next derivative is more important. Consequently, in this frame we can also define $GD(\omega)$ (where GD varies with frequency). For very broadband pulses the higher orders in eq. (1.3) become more important. In fact, when phase-modulation processes become dominant, the low-order expansion at the center wavelength ω_0 is often not sufficient to describe the resulting spectral phase.

There exist different techniques for introducing a wavelength dependent group delay. Simple geometrical compression schemes like grating and prism compressor sequences offer very high to moderate overall GDD and high efficiency. However they are very limited in their ability to control GDD and TOD/FOD separately, since they have only one degree of freedom (their

distance). However, more ingenious devices [20, 67] do exist that allow tuning of two degrees of freedom (GDD and TOD).

Chirped mirrors are photonic crystal structures with a wavelength-dependent $GD(\omega)$ for a defined incidence. This tailored GD can compensate for higher order chirp (TOD and FOD). However, since they are static, they cannot easily be adapted to the setup and proper customized compression demands at least one costly coating run. Furthermore, the GD of chirped mirrors does usually contain oscillations (although several techniques strive for minimizing them), leading to satellite pulses. For larger bandwidths, these are getting more pronounced and decrease the usable bandwidth and achievable peak power [9]. Also the dispersion per bounce is limited (and decreases with larger bandwidth), therefore overall dispersion with decent contrast is quite limited.

Adaptive pulse shapers offer a more convenient control of the GD. There are two important kinds:

The 4f shaper uses a spatial light modulator (SLM) in the Fourier plane of a 4f setup [143]. This SLM is based on liquid crystals and can induce a phase that depends on the wavelength (pixel position). The maximum shaping window (or GD) is given by the spatial resolution of the modulator and the maximum GDD is limited by the maximum GD and the bandwidth to be shaped [9]. As the modulator is usually discrete (pixelated), it will lead to artifacts in time outside of its shaping window. However it can be used at virtually any repetition rate and provides high throughput. Unfortunately, these modulators are usually not available above $2\ \mu\text{m}$.

The other kind of adaptive pulse shaper is called Acousto-optic programmable dispersive filter (DAZZLER, Fastlite), where a AOM is used in both its polarizations. The optical pulse enters in the fast axis of the crystal (TeO_2 in our case) and interacts with an acoustic wave by diffraction. The phase-matching of this process between acoustic and optical pulse is adapted to diffract different spectral components of the optical pulse at different crystals positions onto the slow axis. As the AOM shows large birefringence along both of its axes, this leads to a spectral dependence of $GD(\omega)$ that can be programmed by the acoustic wave. The spectral shaping window is given by the birefringence, whereas the resolution is determined by both length and birefringence of the AOM crystal. As we are employing a diffracted wave, the contrast is not impaired, however the efficiency depends on the shape of the acoustic pulse and the bandwidth and is rather low compared to 4f shapers. As the acoustic wave is pulsed, the speed of sound limits the repetition rate usually to about 20 kHz, making it only useful for medium repetition rate systems. Another feature of AOPDFs is the ability to manipulate the CEP of the optical pulse by changing the CEP of the acoustic wave. Since the acoustic propagation inside the crystal is much slower than in the optical regime, the acoustic wave only needs to be triggered with a delay jitter less than a few 100 ps, to operate without impairing the CEP stability (see section 4.2.1).

Measuring ultrafast pulses

The characterization of ultrashort pulses (i.e. measuring their spectral amplitude and phase) is usually performed using optical methods. An intensity autocorrelation of a pulse, delaying it with

respect to its exact copy (obtained from a balanced beam splitter) and mixing it inside a nonlinear crystal (using SHG, THG, etc.), results in a delay-dependent intensity that can be used (given some assumptions about the pulse shape) to estimate the pulse duration [2]. Much later it was found that spectrally resolving the measurement allows for retrieval of the spectral phase without any additional assumptions [66]. The technique is consequently called frequency resolved optical gating (FROG) and can also be adapted in a cross-correlation (XFROG, using SFG or DFG) with a previously characterized pulse. For the obtained spectrograms, standard software packages are available nowadays, and the method is very well documented by its inventor [138, 139]. It should be mentioned that there are other techniques to characterize ultrashort pulses [10, 60], but these are beyond the scope of this thesis and not used therein.

However, for ever shorter pulses, the supported bandwidth in the nonlinear processes is limited by phase-matching (see section 1.2.2). Attosecond methods [40, 71] of retrieving the electric field directly aim to overcome this limitation in the future.

1.2 Nonlinear optics

The following section is largely adapted from [11] and [133], where derivations are given in more detail.

1.2.1 Second order processes

Whereas linear optics is only concerned about the linear response of the polarization to an electric field ($\tilde{P}(t) = \epsilon_0 \chi^{(1)} \tilde{E}(t)$), nonlinear optics needs to be considered for higher electric fields, where the nonlinear response of the medium gives rise to new polarization contributions, expandable by a power series of

$$\tilde{P}(t) = \underbrace{\epsilon_0 \chi^{(1)} \tilde{E}(t)}_{\tilde{P}^{(1)}(t)} + \underbrace{\epsilon_0 \chi^{(2)} \tilde{E}^2(t)}_{\tilde{P}^{(2)}(t)} + \underbrace{\epsilon_0 \chi^{(3)} \tilde{E}^3(t)}_{\tilde{P}^{(3)}(t)} + \dots \quad (1.4)$$

where time varying fields are indicated with the tilde. Here we are only interested in second ($\tilde{P}^{(2)}$) and third order ($\tilde{P}^{(3)}$) polarization. For two different frequencies ω_1 and ω_2 , the electric field is given by

$$\tilde{E}(t) = E_1 e^{-i\omega_1 t} + E_2 e^{-i\omega_2 t} + c.c. \quad (1.5)$$

so that the second order polarization can be divided into the resulting frequency components

$$\tilde{P}^{(2)} = \sum_n P(\omega_n) e^{-i\omega_n t} \quad (1.6)$$

given by

$$P(2\omega_1) = \epsilon_0 \chi^{(2)}(\omega_3 = \omega_1 + \omega_1) E_1^2 \quad (\text{SHG}) \quad (1.7)$$

$$P(2\omega_2) = \epsilon_0 \chi^{(2)}(\omega_3 = \omega_2 + \omega_2) E_2^2 \quad (\text{SHG}) \quad (1.8)$$

$$P(\omega_1 + \omega_2) = \epsilon_0 \chi^{(2)}(\omega_3 = \omega_1 + \omega_2) E_1 E_2 \quad (\text{SFG}) \quad (1.9)$$

$$P(\omega_1 - \omega_2) = \epsilon_0 \chi^{(2)}(\omega_3 = \omega_1 - \omega_2) E_1 E_2^* \quad (\text{DFG}) \quad (1.10)$$

Here the polarization components for second harmonic generation (SHG), sum frequency generation (SFG) and difference frequency generation (DFG) will lead to radiation, while DC components are not considered.

Since polarization and electric field inside a crystal need to be represented as vectors with indices i, k, j (and not scalars as above) to take the crystal geometry into account, the nonlinear susceptibility $\chi^{(2)}$ is then represented by a tensor

$$P_i(\omega_n + \omega_m) = \epsilon_0 \sum_{jk} \sum_{(mn)} \chi_{ijk}^{(2)} E_j(\omega_n) E_k(\omega_m) \quad (1.11)$$

however, for a given frequency mixing, crystal orientation and field polarizations, we may reduce it to an effective nonlinear susceptibility d_{eff} like

$$P(\omega_1 + \omega_2) = 4\epsilon_0 d_{\text{eff}} E(\omega_1) E(\omega_2) \quad (1.12)$$

for SFG. This allows for easy calculation of the fields and an easy comparison between different crystals and their orientations.

DFG (OPA)

The coupled wave equations for difference frequency generation describe the dependence of the field amplitudes (for signal, idler and pump) A_s , A_i and A_p on z during propagation through a nonlinear medium. Note that in DFG, the idler is generated as the difference between pump and signal wave. While this is equivalent to OPA¹, the pump wave there is typically a lot more intense and in most cases the amplified signal wave is used. For all cases treated in this manuscript, the medium is assumed to be non-magnetic and non-absorbing at the angular frequencies ω_i , ω_s or ω_p). Also it contains no free charges or currents, so that $\nabla \cdot \tilde{E} = 0$ and $j = 0$. The displacement vector $\tilde{D} = \epsilon_0 \tilde{E} + \tilde{P}_L + \tilde{P}_{NL} \equiv \tilde{D}_L + \tilde{P}_{NL}$ can be separated into a linear and nonlinear polarization part, where the linear part is simply $\tilde{D}_L = \epsilon_0 \epsilon_L \tilde{E} \approx \epsilon_0 n(\omega)^2 \tilde{E}$ and represents the linear (wavelength dependent) response of the material. Using Maxwell's equations we obtain a source term in the wave equation that is proportional to the nonlinear polarization:

$$\nabla^2 \tilde{E} - \frac{n(\omega)^2}{c^2} \frac{\partial}{\partial t^2} \tilde{E} = \frac{1}{\epsilon_0 c^2} \frac{\partial}{\partial t^2} \tilde{P}_{NL} \quad (1.13)$$

¹In this manuscript, OPA will be used synonymously for OPCPA, unless the context is only applicable to OPCPA.

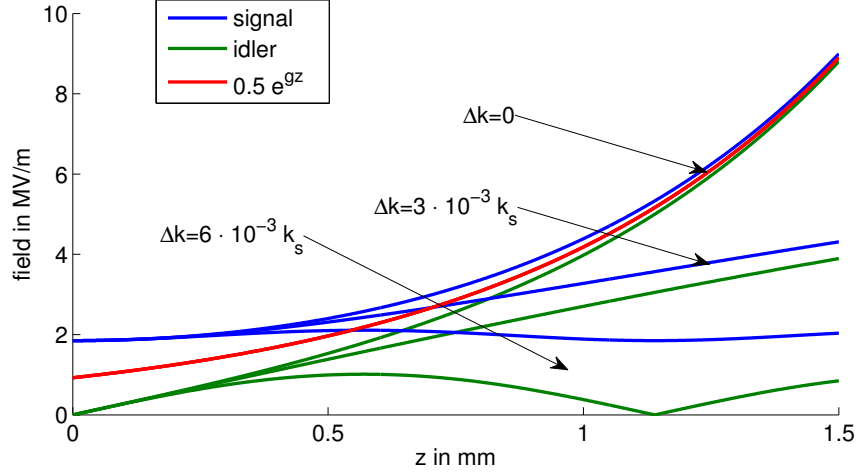


Figure 1.2: Amplitudes of the fields in the coupled wave equations (as given in eqs. (1.16) and (1.17)) plotted over z

Now plugging in the amplitude of the polarization given by eq. (1.12) and separating the z -dependence of the amplitudes $E_m = A_m(z)e^{i(k_m z - \omega_m t)} + c.c.$ we can apply the slowly varying envelope approximation. Then, for the one-dimensional case, this simplifies to the coupled wave equations for difference frequency generation:

$$\frac{dA_s}{dz} = \frac{2i\omega_s^2 d_{\text{eff}}}{k_s c^2} A_p A_i^* e^{i\Delta k z} \quad (1.14)$$

$$\frac{dA_i}{dz} = \frac{2i\omega_i^2 d_{\text{eff}}}{k_i c^2} A_p A_s^* e^{i\Delta k z} \quad (1.15)$$

where the mismatch in wave vectors is abbreviated as $\Delta k = k_p - k_s - k_i$.

For the boundary conditions of no idler at the front surface of the crystal ($A_i(0) = 0$), the solution is given by [11]:

$$A_s(z) = \left[A_s(0) \left(\cosh(gz) - \frac{i\Delta k}{2g} \right) \right] e^{i\Delta k z/2} \quad (1.16)$$

$$A_i(z) = \left[A_s^*(0) A_p \frac{2i\omega_i^2 d_{\text{eff}}}{k_i c^2 g} \sinh(gz) \right] e^{i\Delta k z/2} \quad (1.17)$$

where g is the gain of the optical parametric amplification process and given by

$$g = \sqrt{4|A_p|^2 \frac{\omega_s \omega_i}{n_s n_i c^2} d_{\text{eff}}^2 - \left(\frac{\Delta k}{2} \right)^2} \quad (1.18)$$

Equation (1.17) is plotted over z in fig. 1.2 for different values of phase-mismatch Δk . Note how for perfect phase-matching both seed and idler follow $\frac{1}{2}e^{gz}$, while for larger Δk the amplification drops first and even ceases, when the idler and signal are both reconverted to their initial values.

The parameters (angular frequencies, d_{eff}) for fig. 1.2 are comparable to the first stage of the OPCPA described in section 5.3.

In eqs. (1.17) and (1.18), we see that the small signal amplification in OPA is exponential and the exponent is proportional to the crystal length, to d_{eff} and the square root of the intensity. As soon as the pump wave is considerably depleted, the gain will finally saturate. More accurate analytical expressions for this behavior are found in [133]. However, temporal (because of group velocity mismatch) and spatial (because of Poynting vector walk-off and different mode divergences) walk-off of the fields still limits the efficiency of the process, so often much more elaborate simulations need to be employed to reproduce the experimental conditions.

1.2.2 Phase-matching

As seen in the previous section, a wave vector mismatch of $\Delta k = k_p - k_s - k_i$ is detrimental to the parametric gain process. If we write out this expression, we find that

$$\frac{n_p(\omega_p)\omega_p}{c} = \frac{n_i(\omega_i)\omega_i}{c} + \frac{n_s(\omega_s)\omega_s}{c} \quad (1.19)$$

conservation of momentum is equivalent to phase-matching. Since all refractive indexes are functions of frequency, the phase-matching effectively determines the bandwidth of nonlinear processes (when detecting on-axis radiation only²). In order to find favorable phase-matching, Δk is minimized in birefringent crystals by choosing the pump polarization (the field with the largest frequency) along the fast axis. If we define the gain G of the OPA process as

$$\frac{I_s(L)}{I_s(0)} = 1 + G \quad (1.20)$$

where the intensity I_s is given by $I_s = 2n_s\epsilon_0c|A_s|^2$ we can plot G over wavelength to find phase-matched spectral regions.

Angle phase-matching

The two most employed crystals in this manuscript are Lithium Niobate (LNB) and β -Barium Borate (BBO). Both are negative uniaxial crystals, meaning that $n_e < n_o$. In type-I configurations, signal and idler both have the same polarization, so eq. (1.19) simplifies to

$$n_p^e(\theta)\omega_p = n_s^o\omega_s + n_i^o\omega_i \quad (1.21)$$

where $n_p^e(\theta)$ can (but does not necessarily) contain phase-matched angles θ . d_{eff} can then be calculated from $d_{\text{eff}} = \hat{e}_i \cdot \chi^{(2)} : \hat{e}_p \hat{e}_s^*$.

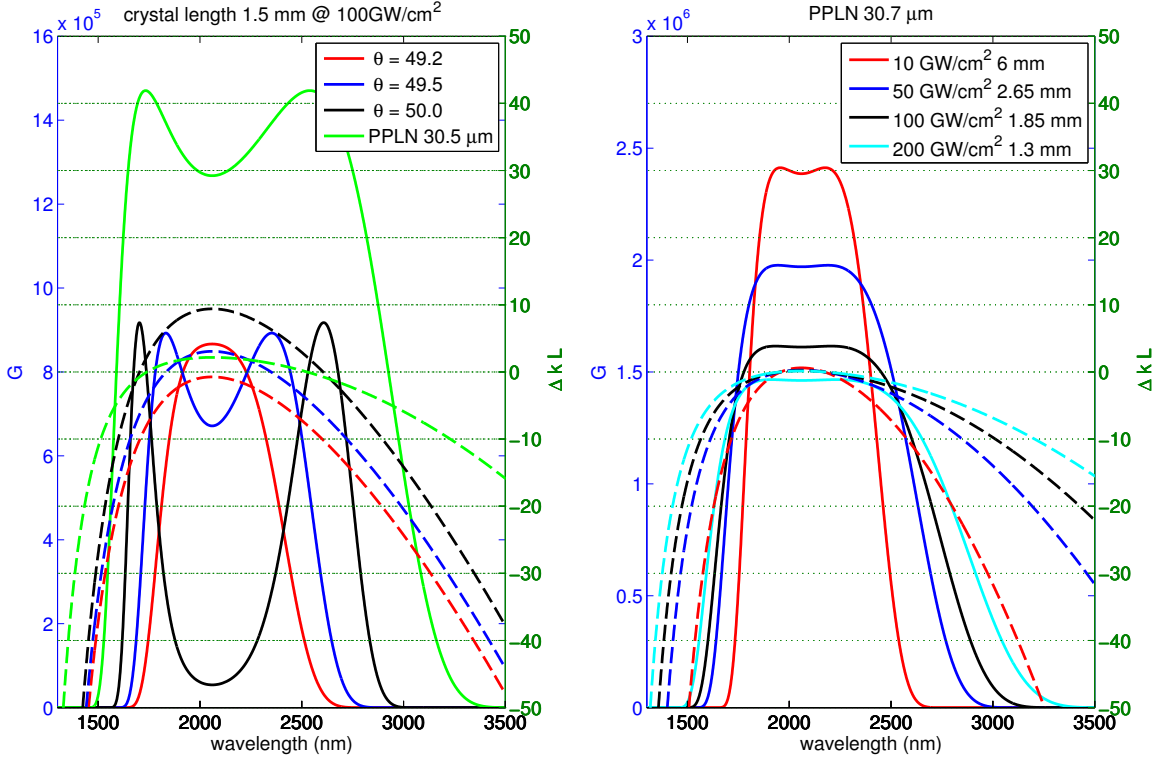


Figure 1.3: Left: OPA gain spectrum for different phase-matching angles of lithium niobate and comparison to QPM in PPLN. Right: Scaling of pump intensity with gain held constant by varying the crystal thickness. solid: gain G , dashed: phase mismatch

Quasi-phase-matching (QPM)

Another approach is to allow phase mismatch for a distance equivalent to the coherence length L_{coh} , when $\Delta k L_{coh} = \pi$ and then switch the sign of d_{eff} after this period before destructive interference of the signal would occur, leading to a continuous buildup of signal and avoiding the back-conversion seen in fig. 1.2. Apart from being tailorable, this kind of phase-matching also allows access to the largest component of the second order susceptibility tensor of lithium niobate $\chi_{zzz}^{(2)}$, by having all polarizations aligned along the z -axis. For angle phase-matching, the use of this large component is not possible (see eq. (1.19)), therefore the nonlinearity of PPLNs is unmatched in the VIS/NIR. The left of fig. 1.3 shows how PPLN easily trumps angle-tuned lithium niobate crystals in bandwidth by better phase-matching alone (consider the more flat phase mismatch curve), while providing larger gain due to higher d_{eff} . (In the plot $d_{eff} = 4.0 \frac{\text{pm}}{\text{V}}$ is held constant for all crystals, otherwise the PPLN would be off the chart with $14.9 \frac{\text{pm}}{\text{V}}$). As the PPLN can be selected several times thinner for comparable gain (compare eq. (1.18)), this allows better phase-matching. The downside of PPLNs is that they cannot be grown in large apertures

²As argued in [3] and [96], non-parallel k -vectors and their detection (“dithering”) increase the bandwidth of the plane wave approximation.

while still providing a clean periodic structure [63]. At the same time, the parasitic nonlinearities of lithium niobate are higher than for other crystals (e.g. n_2 , see table B.1) and the damage threshold is relatively low. This limits them to low and medium energy applications.

Shorter pump pulses

To extend the bandwidth even further, the crystal length (and therefore the phase mismatch ΔkL) can be reduced. An example is shown on the right side of fig. 1.3 for a 30.7 μm PPLN, whose thickness was decreased with increasing pump intensity to hold the gain G constant. The phase-mismatch curve flattens with the shorter crystals, however the pump intensity needs to remain below the damage threshold. As this threshold scales favorably with short pulses [132], the development of ultrashort pump lasers was enforced in recent years.

1.2.3 Higher order processes

Equation (1.4) also contains third order polarization components in $\tilde{P}^{(3)}(t)$. While being more complicated, interesting effects like self-phase modulation (SPM), cross-phase modulation (XPM), third harmonic generation (THG), two photon absorption (TPA) and self-focusing (Kerr-lensing; a spatially dependent $n_2(x, y)$ with x, y transversal to the propagation direction) are caused by the third order susceptibility $\chi_{ijkl}^{(3)}$. As there are four waves participating (that may be degenerate), these effects can all be considered so-called four-wave mixing (FWM) effects. While for second order processes, media need to show some kind of anisotropy, third order processes can be observed in virtually all media, including dielectrics and gases.

In the absence of a second field ($\tilde{E}(t) = Ee^{-i\omega t} + c.c.$), the degenerate processes of $\tilde{P}^{(3)}(t)$ can be separated by their frequency into $\tilde{P}^{(3)}(t) = \sum_n P(\omega_n)e^{-i\omega_n t}$. The interesting components here are

$$P(\omega) = \epsilon_0 \chi^{(3)} (3EE^*) E \quad \text{SPM} \quad (1.22)$$

$$P(3\omega) = \epsilon_0 \chi^{(3)} E^3 \quad \text{THG} \quad (1.23)$$

With introduction of a second field (that could have the same or different polarization, this only changes the indexes in $\chi_{ijkl}^{(3)}$) $\tilde{E}(t) = E_1 e^{-i\omega_1 t} + E_2 e^{-i\omega_2 t} + c.c.$ new terms become relevant, giving rise to XPM

$$P(\omega_1) = \epsilon_0 \chi^{(3)} (3E_2 E_2^*) E_1 \quad \text{XPM} \quad (1.24)$$

When we plug in eq. (1.22) (similar for eq. (1.24)) into the source term of eq. (1.13), we see that the refractive index has experienced an intensity dependent shift Δn :

$$\nabla^2 \tilde{E} - \frac{1}{c^2} \frac{\partial}{\partial t^2} \left(n(\omega)^2 + 3\chi^{(3)} |\tilde{E}(\omega)|^2 \right) \tilde{E} = 0 \quad (1.25)$$

If we define the nonlinear refractive index n_2 as a correction to the linear refractive index $\Delta n = 2n_2|E|^2$, it follows for SPM (fields only along one polarization)

$$n_2 = \frac{3}{4n}\chi_{xxxx}^{(3)} \quad (1.26)$$

Likewise, for XPM we find a factor of 6 in eq. (1.25) for all fields being polarized along the same axis in an isotropic medium.

As usually we are more interested in the response of the medium to the intensity, there is a second definition for n_2 (mostly used in the literature, also dubbed γ):

$$\Delta n = 2n_2|E|^2 \equiv n_2^I I \quad (1.27)$$

that can be converted by $\gamma \equiv n_2^I = \frac{n_2}{\epsilon_0 n_0 c}$.

B-integral

Often the accumulation of pulse distortions induced by SPM (or XPM) are simply characterized by the B-integral [76]

$$B = \frac{2\pi}{\lambda} \int_l n_2^I I(z) dz \quad (1.28)$$

which adds up the nonlinear phase shift of eq. (1.27) over the path length l in the transmitted medium. As n_2 is usually positive (unless close to two photon absorption) in most materials, the B-integral is monotonically growing. In space it promotes the small-scale self-focusing of spatial distortions and can lead to optical damage [76]. Also it can distort the temporal profile of the pulse, like shown in fig. 3.5, especially for ultrashort pump lasers that are typically used in OPCPA. Therefore B should be kept low.

Spectral broadening and self-steepening

For a pulse with $\tilde{E}(z, t) = \tilde{A}(z, t)e^{i(\omega t - kz)} + c.c.$ a shift in the (time-dependent) refractive index $\Delta n(t)$ over the absolute value of $k_0 = \frac{n\omega}{c}$ leads to a shift in $k = k_0 + \Delta n(t)\frac{\omega}{c}$. Since this leads to a (time-dependent) phase-shift for the whole pulse, we need to shift the overall phase, to find the relative modulation. We do this using the phase velocity in the substitution: $t' = t - z\frac{n}{c}$. This gives the modulated pulse $\tilde{E}(z, t') = \tilde{A}(z, t')e^{i(\omega t' - \Delta n\frac{\omega}{c}z)} + c.c.$ and therefore a time-dependent nonlinear phase-shift of

$$\phi_{NL}(t) = -\Delta n(t)\frac{\omega}{c}z = -\frac{\omega}{c}n_2^I I(t)z \quad (1.29)$$

For the instantaneous frequency $\omega(t)$ of the pulse, this means a shift of $\delta\omega(t) = \frac{d}{dt}\phi_{NL}(t)$ and results in

$$\omega(t) = \omega_0 - n_2^I \frac{\omega}{c} z \frac{dI(t)}{dt} \quad (1.30)$$

As the refractive index $n = n_0 + n_2 I(t)$ changes with the time-dependent intensity $I(t)$ and n_2 is usually positive, the instantaneous frequency in eq. (1.30) will create red-shifted frequency-components at the leading edge of the pulse and blue-shifted at the trailing. This mimics a linear chirp in the center of the pulse, but increases the bandwidth elsewhere at the same time. The modulation strength is obviously given by the temporal gradient of the pulse. Note that the phase of the pulse is modulated according to the temporal pulse shape. For non-ideal pulses, this can often not be compensated. As a consequence, the spectral broadening then naturally leads to satellite pulses or pedestals and therefore comes at the cost of contrast [129]. In fact, the temporal shape of the pulse determines how well the broadened spectrum can be compressed [137].

The most broadband spectra generated from broadening are in general not symmetric around the center wavelength. This is caused by higher order dispersion and the effect of self-steepening. As the peak of the pulse experiences a larger group velocity, it is delayed with respect to the center, leading to an even steeper temporal gradient of the trailing edge and (from eq. (1.30)) consequently more spectral extension into the blue from this so-called shock wave. The derivation is beyond the scope of this work and can be found in [11], chapter 13. Self-steepening is significant when the input spectral bandwidth of a pulse is already significant compared to the output spectrum, for example in super-continuum generation (like performed in section 2.2 or section 7.4).

Kerr lensing

An intensity dependent refractive index can also lead to modulations in the spatial domain. This includes effects like nonlinear holography using several beams (transient grating), which can be used for ultrafast pulse characterization. The beam can even focus itself due to a spatial gradient in its beam profile, which is called Kerr-lens self-focusing. For pulses exceeding the critical power

$$P_{cr} = \frac{\pi(0.61)^2 \lambda^2}{8n_0 n_2} \quad (1.31)$$

this ultimately leads to self-trapping of the beam (filamentation), where one filament carries exactly P_{cr} and the diffraction (enhanced by plasma generation) is compensated by self-focusing. As it increases the interaction length of SPM at high intensity, filamentation is useful for spectral broadening. To enhance the self-focusing tendency (that often only leads to very long focal lengths), usually one focuses weakly into a medium. However diffraction and the dispersion of the medium limit the length of the filament.

Two-photon absorption

Four-wave mixing can modulate not only the phase, but also the amplitude of a pulse. The imaginary part of $\chi^{(3)}$ leads to two-photon absorption (TPA) according to [133] $\frac{dI}{dz} = -\alpha I - \beta I^2$

and

$$\beta = \frac{3\pi}{\epsilon_0 n^2 c \lambda} \text{Im} \left(\chi_{xxxx}^{(3)}(-\omega; \omega, \omega, -\omega) \right) \quad (1.32)$$

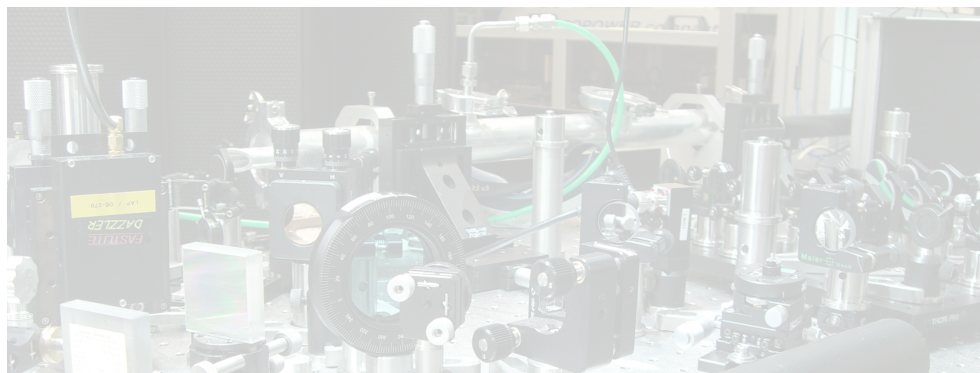
The effect is only considerable when the medium contains a transition which is resonant near twice the photon energy. This is the case for the silicon plates used for pulse compression in section 5.4 and demands low intensities (large spot sizes) as significant fractions of the pulse energy can be absorbed. Besides, it further motivates long wavelength few-cycle pulses for probing ultrafast processes in moderate band-gap dielectrics at high fields (see chapter 6) without breaking the sample under investigation.

Photo-refraction

The properties of lithium niobate are very favorable in general, as it does not show any absorption in the near infrared (see table B.2) and is not hygroscopic. However, especially for shorter wavelengths it suffers from photo-refraction, a spatial laser-induced distribution of carriers. The local fields of these charges then lead to a modulated refractive index. While this is a very strong (and therefore rather slow) nonlinear effect, it cannot be described by means of higher-order susceptibilities. To prevent it to some extent, MgO-doping and heating help to elevate the damage threshold to levels that can be used for OPCPA. However, the damage threshold is still much lower than for crystals like BBO, while n_2 is significantly higher (table B.1), leading to large B-integrals in the OPA stages of chapter 5.

1.2.4 OPCPA

OPCPA adds the concept of CPA [131] to the parametric amplification. Rather than working with compressed pump and seed pulses, the seed in OPCPA is chirped to enable power scaling (minimizing unwanted nonlinearities) and overlap significantly with longer (nanosecond to picosecond) high energy pump pulses. This is important, since pump lasers with few-ps pulse durations are technically very challenging and often have to rely on CPA themselves. The pump window (the temporal window of the pump pulse with significant gain) is optimized according to the gain of the OPCPA stage, described in great detail in [91]. A larger window will avoid clipping the spectral bandwidth of the seed, but the efficiency will decrease. Even worse, the undepleted and unseeded temporal parts will tend to amplify more so-called superfluorescence (SF), as the small signal gain of OPA can be large enough to amplify noise to significant levels. When the seeding level is not large enough, this becomes a serious issue, as the SF is not phase-stable or compressible, deteriorating the contrast of the OPCPA after compression. On the other hand, a larger pump window lessens the requirements on pump and seed synchronization described in chapter 4.



Chapter 2

Seeding OPCPA

2.1 The seed laser

The femtosecond pulses needed for seeding both pump and seed amplifiers of the OPCPA are generated inside a commercial Kerr-lens mode-locked Ti:sapphire oscillator (Rainbow, Femtolasers). As mentioned in section 1.1.1, this oscillator sets the frequency comb that both amplifiers will be lasing on. It does not need to be CEP stabilized for our purposes.

In OPCPA systems, for all but the most broadband of high-power pump lasers [103, 118], more broadband laser sources are synchronized for seeding. This can either be done directly [36] or, typically for higher seed energies, after further broadening the seed spectrum by using self phase modulation in noble gases. In any case, the synchronization between pump and seed pulses needs to be ensured (see chapter 4).

The setup of the seed generation is shown in fig. 2.1. The long-wavelength spectral part of the oscillator output (> 1000 nm) is used to seed the pump laser (see section 3.1.2). A Ti:Sapphire amplifier, running at 3 kHz and described elsewhere in more detail [18], is seeded by the remainder. It is based on the commercial Femtopower Pro HR/CEP from Femtolasers. After amplification 5% of the pre-compressed 1 mJ pulses are split off for our purposes. While 5% of this 50 μ J are used for delay and beam pointing stabilization (where chirped pulses are advantageous), the rest is finally compressed by a pair of thick SF57 wedges, AR-coated for the laser wavelength.

Figure 2.2 shows a pulse characterization of the compressed pulses using second harmonic generation frequency resolved optical gating (SHG FROG). The retrieved spectral phase indicates some uncompensated higher order dispersion, which is to be expected, given that the final compression is done by the thick wedges alone. However most of the pulse energy is confined to the main pulse and the result proved to be sufficient for efficient seed generation. Reconstruction gives a pulse duration of $\tau_{FWHM} = 26.5$ fs and a bandwidth of $\Delta\nu_{FWHM} = 67$ nm. The time axis of the retrieval was determined by insertion of additional glass. In fact the spectral broadening appeared much more sensitive to changes of dispersion than the FROG, however with an offset

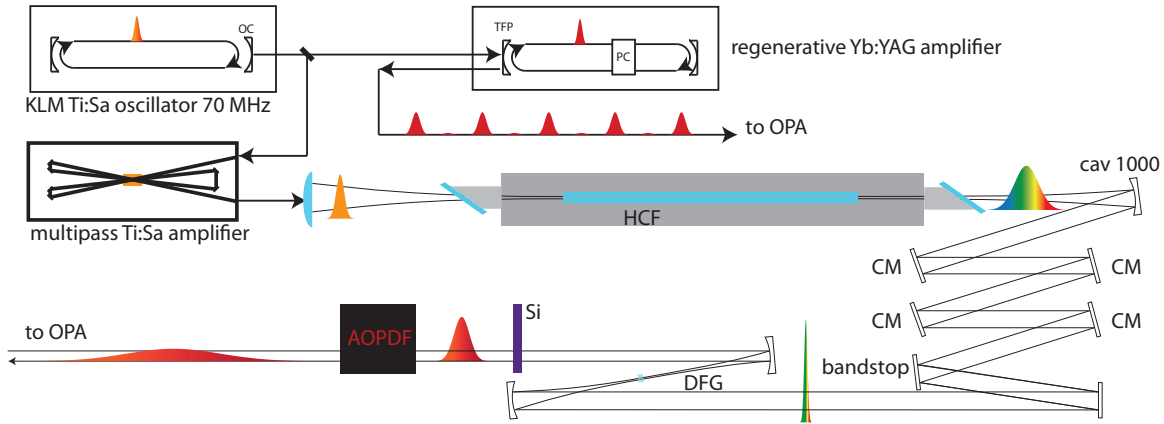


Figure 2.1: Seed generation scheme of the OPCPA.

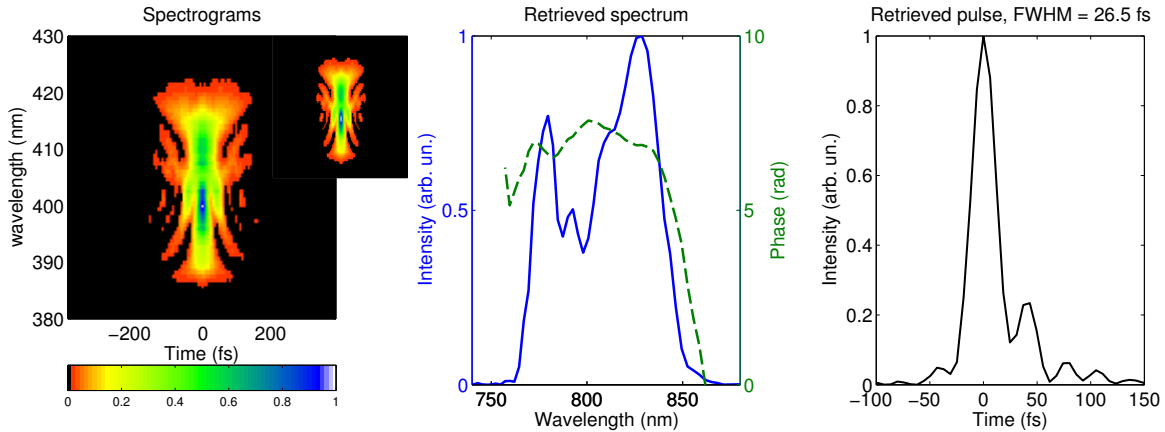


Figure 2.2: Measured and retrieved (inset) SHG FROG trace of the seed amplifier and retrieved temporal and spectral intensity and phase.

due to dispersion of the entrance window and gas in the gas cell. Moreover the retrieved spectral phase allows the use of the seed laser as a reference pulse for cross-correlation FROG (XFROG) with more complicated, synchronized pulses (as shown in section 2.3).

Stable broadening demands good stability with respect to pulse energy and beam pointing [65] from the driving laser. The pulse energy stability of our seed pulses amounted to $\sigma_P = 2.2\%$. It was characterized using a diode with sufficient aperture and integrating in time over the temporal (electronic) pulse profile.

Characterizing beam-pointing needs to be done carefully. Position sensitive detectors (PSDs, like used in section 3.2.3 and section 4.3.5) are able to resolve beam-pointing for single shots, where CCDs are read out slowly and typically integrate over many shots, therefore suppressing high-frequency beam-pointing components and leading to an underestimation of beam pointing instability (see discussion in section 4.3.5). As PSDs only return a voltage level proportional to

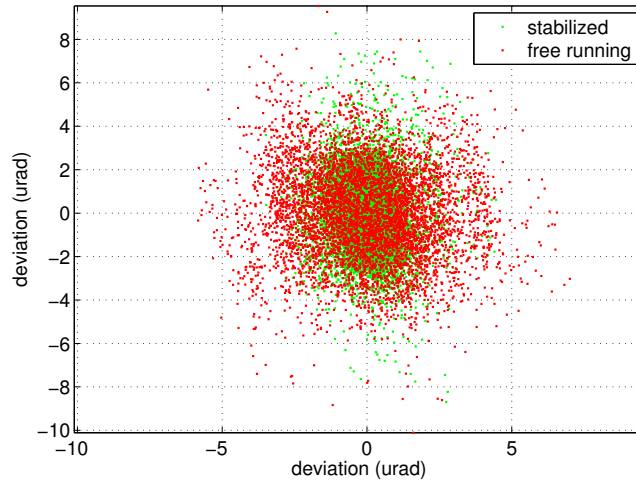


Figure 2.3: Angular beam pointing of the seed laser before the entrance of the hollow core fiber.

the (center of mass) position, they need to be calibrated. For the PSDs and readout electronics used this is done in appendix C.1, where very good linearity is found. The fitted scaling coefficients are $(17.41 \pm 0.02) \frac{\text{mV}}{\mu\text{m}}$ and $(7.73 \pm 0.02) \frac{\text{mV}}{\mu\text{m}}$ respectively. One may note that this is actually proportional to the respective detector sizes. PSDs offer sub- μm resolution, however the read-out demands ADCs of higher resolution than usual oscilloscopes (8 bit), since the processed (analog) position signal ranges up to 10 V. Therefore 16 bit ADCs (USB-6229 with 250 kS/s from National Instruments) with sub-mV resolution were used. Since the processing read-out electronics directly after the PSDs sample and hold the readings for each optical pulse, the single electronic pulses do not have to be resolved, allowing for relatively slow sampling. Also the RC-constant was very large at $\tau_{\text{RC}} \approx 70 \mu\text{s}$, due to the large detector size and input impedance (10 G Ω). This is leading to some overlap between pulses and effectively limits the measured beam pointing bandwidth.

Figure 2.3 shows the measured beam pointing at the focus of a 1 m focusing lens, right where it would be coupled into a hollow core fiber (HCF) (the beam was attenuated to avoid nonlinear effects in this measurement¹). With only $\sigma_{\text{unstabilized}} = 1.40 \mu\text{rad}$, the stability is even sufficient without external stabilization for a HCF with an inner diameter of 140 μrad . However slow thermal drifts make the setup more reliable when using a feedback stabilization and fast beam pointing was improved to $\sigma_{\text{stabilized}} = 1.07 \mu\text{rad}$. The pointing appears more centered in fig. 2.3, however the jitter in y-direction is larger due to mechanical piezo resonances being stronger along this axis. More rigid construction can lead to better performance, as indicated by $\sigma_{\text{stabilized},x} = 0.92 \mu\text{rad}$. Still, the throughput of our 140 μm hollow core fiber fluctuated only by 0.8% in

¹Note that position sensitive detectors rely on highly linear signals for normalization, therefore nonlinear responses would decrease the resolution. This dictates low fluences for femtosecond sources when measured at the focus, decreasing the signal-to-noise ratio. As this again would limit the resolution, measuring at two positions away from the focus and software-correction or chirping of the pulses can be used to overcome this limitation.

intensity (measured with a miniature spectrometer over 505 shots at 10 Hz with 12 ms integration time). Note that due to integration the output could only appear more stable than the input of the HCF.

2.2 Spectral broadening for seeding ultrabroadband OPCPA

For broadening the compressed Ti:Sapphire pulses, we used self-phase modulation in inert gases. Two methods are employable for the temporal and intensity regime of the input pulses: filamentation and broadening in a hollow core fiber (HCF). The following subsections will describe both methods and results.

2.2.1 Spectral broadening by filamentation

Filamentation is based on the interplay of Kerr-lens self-focusing (see section 1.2.3) and defocusing by the generated plasma and diffraction after collapse is reached. Furthermore the intensity of the pulse is clamped by the steep onset [25] of multi-photon-ionization. As spectral broadening is happening even without further guiding by a hollow fiber, filamentation (and self phase modulation happening during the process) alone can be a very efficient way of broadening, as transmission (and coupling) losses are avoided. However, some off-axis emission occurs that needs to be removed and the achieved broadening is limited, making it less desirable for the generation of the very shortest pulses.

Filamentation has other disadvantages, as the critical power P_{cr} is limited and high gas pressures for extended broadening can consequently lead to multi-filamentation, especially for beam profiles that contain spatial distortions [13]. When multiple filaments arise, they tend to interchange energy, changing their spatial and spectral characteristics at the same time. Therefore they cannot be used for stable seed generation.

A clean laser mode is more crucial as compared to HCF broadening, as filamentation is very sensitive to spatial distortions like astigmatism. Also the splitting into several filaments depends on the spatial properties of the beam. Methods of "cleaning" the beam profile by apertures, leading to a more stable filamentation [22, 24], are lossy and only mimic the inherent nature of a HCF.

In fig. 2.4 the spectral broadening in a gas cell is shown for different pressures. Krypton gas and a $f = 500$ mm focusing lens (with a broadband AR coating) were used, as well as 93 mW of input power. The output power (measured over the whole beam profile with a power meter head) was around 60 mW and did not change significantly over pressure. All plotted curves were normalized to a peak of 0 dB, as equivalent coupling into the spectrometer's delivery fiber (single mode) for all pressures can not be assumed. The output is quite low for filament compression, but can be attributed to the limited AR bandwidth from the exit window (OA222, Femtolasers) and the

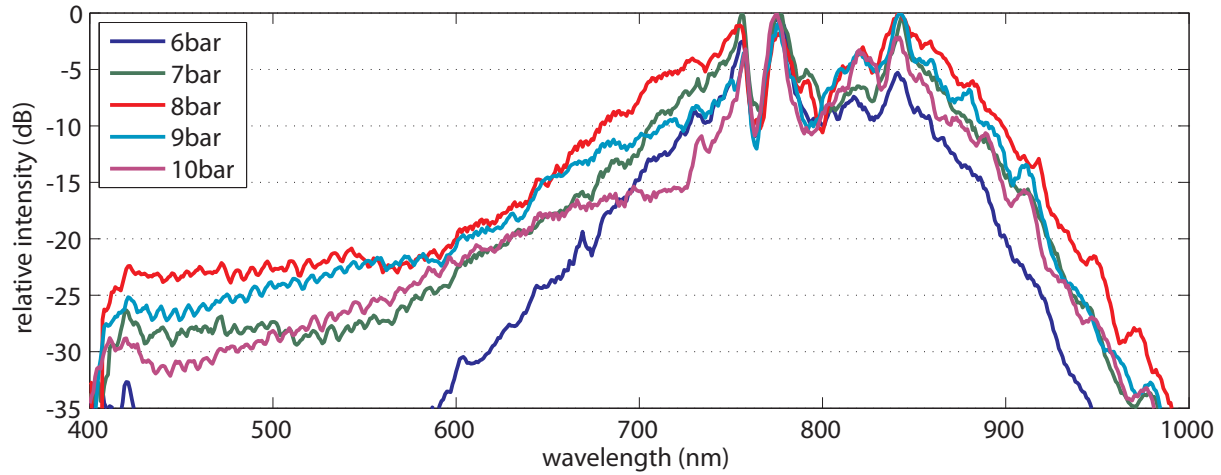


Figure 2.4: Spectral broadening by filamentation for different pressures of Krypton.

finite output window size, clipping the outer parts of the mode. Using larger Brewster windows in another (lower pressure) setup, larger throughput could be achieved. Spectra were taken with an optical spectrum analyzer for sufficient sensitivity in the weak spectral parts (Ando AQ6317). The light was not focused into the collecting fiber, as further broadening was observed there as well. The signal however was still large enough when illuminating the fiber with the filament's very center. We see in fig. 2.4 that broadening with Krypton was maximized for a pressure of about 8 bar. The blue tail is clearly preferred, whereas the broadening in the red stagnates around 1000 nm. For 6 bar there does not seem to be enough self-steepening (section 1.2.3) for the spectrum to extend into the blue region. Since most of the energy (85% for 8 bar) is still centered in the spectral part of 700–900 nm, for truly broadband OPCPA seeding this is not a very satisfying result. Changing gases and focusing conditions did not significantly improve this general tendency. Therefore we went to broadening using a HCF.

2.2.2 Spectral broadening in a hollow core fiber

The used hollow core diameters are rather small compared to [18], since our pulse energies are quite low. As transmission is limited for smaller core sizes, the fiber is also kept short at around 17 cm. The Krypton gas pressure is kept below 5 bar (the mechanical limit for the glued windows, as confirmed experimentally) and the Brewster-windows made from fused silica are 1 mm thick.

The fiber is resting on a V-shaped trench cut into a steel rail. Less rigid rails were found to bend and inhibit single mode transmission. A mechanically sound setup for a HCF defines not only position but also direction and divergence of the emitted mode. Therefore it is not only a benchmark of the spatial jitter of the incoming beam, but also makes alignment-sensitive setups behind it more reproducible, as spatial coupling, dispersion and gas pressure can be optimized while aligning the input beam instead of the static fiber. As only the mode with the least losses (EH_{11} for fused silica waveguides) will propagate sufficiently in the fiber [84, 94], it acts like a spatial

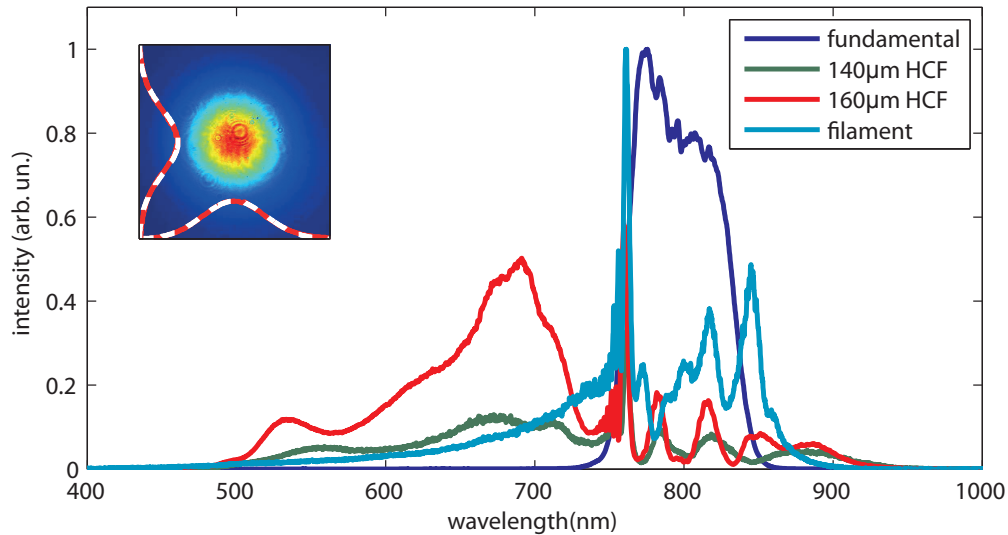


Figure 2.5: Spectral broadening in a HCF filled with Krypton using $f = 750$ mm focusing. Gas (absolute) pressures were 2.86 bar (140 μm), 4.60 bar (160 μm) and 4.75 bar (filament).

filter against higher order spatial distortions, if the coupling conditions are chosen appropriately.

Hollow core fiber setups for broadening have lots of parameters to tune; focusing length, input pulse energy and duration, gas pressure and type, fiber diameter and length, distance of fiber entrance to focus and filament. None of them are decoupled however, making a systematic scan of a single parameter (like for filaments) not useful. Smaller inner fiber diameters result in more broadening (at the same pressure) and less transmission. The required focus needs to be matched by gas pressure and focusing length to couple most energy into the fundamental mode. As an example, higher gas pressures would lead to stronger self-focusing. Since the filament then appears earlier (with respect to the focus position) in the gas cell, the distance to the fiber changes and needs to be re-optimized for good transmission (as an alternative, one could decrease the pulse energy, leading to lower overall throughput as well). Probably the spot size changed, so the fiber inner diameter is now too large, leading to the excitation of higher order modes in the fiber². Replacing the fiber then would ask for an optimized new fiber length. Therefore good parameters have to be found by careful optimization and matching of parameters.

Out of the inert gases typically used, Neon and Argon both showed too little broadening for pressures the gas cell could support, while Kr around 3 to 5 bar and Xe (1 to 2 bar) showed sufficient and comparable broadening. However, for economical reasons we selected the less rare Kr, as the volume of the gas cell was rather large (~ 1200 cm^3). The input pulses were used at full pulse energy (without the use of apertures) and the dispersion was optimized for long and visible filaments before the fiber entrance.

²Interesting however is that these colorful modes can be very stable and sometimes experience more broadening than the fundamental, since their local intensities are higher.

Some typical results are shown in fig. 2.5. Here, the broadened spectra were normalized according to their throughput (except for the fundamental). The focusing conditions were held constant by using a $f = 750$ mm plano-convex lens and an input power of 113 mW. The filament showed considerably less broadening in the gas cell compared to the HCF broadened spectra. Note that a pronounced spike appears in all of the spectra at the blue part of the fundamental. The throughput was very high using a filament (110 mW) in this larger gas cell (compared to section 2.2.1) and dropped towards smaller HCF diameters (64 mW using 160 μm and 36 mW using 140 μm). Also for smaller fiber diameters the gas pressure could be reduced for similar broadening. In the inset of fig. 2.5, the beam profile out of the HCF is shown together with an excellent fit to a Gaussian profile.

While the filament still leaves most energy concentrated around the fundamental, the HCF is able to broaden towards energetic spectral wings that reach much further in both directions. This makes it better suited for ultra-broadband frequency mixing, given that the spectral phase is well-behaved. The latter will be investigated in the next section.

2.3 Compression and characterization of the broadened spectra

Since the generated spectra alone do not prove the compressibility of the generated pulses, in this section the spectral phases of both one filament and HCF configuration will be characterized using the (SFG) XFROG technique. As the reference pulse, a part of the seed laser was split off and characterized as in fig. 2.2. Since both both pulses are inherently synchronized (and the reference pulse is quite short and simple), this method offers a high resolution, can be applied even to the most complex pulses [45] and allows good interpretation even without reconstruction [95]. Figure 2.6 shows an XFROG spectrogram of filament (left) and HCF (right) broadening. The respective retrieved spectra are shown below. Again we see that the HCF broadens better towards the long-wavelength side, the short-wavelength one is not interesting here (as it cannot be properly compressed using our chirped mirrors) and was cut by the use of gold mirrors. Overall the spectral wings are very clean in both cases, allowing the generation of high contrast difference frequency generation (DFG) pulses. However, the filament shows a much more complicated structure around the fundamental, which could lead to pedestals or satellite pulses after DFG.

Note that we are not necessarily interested in creating a bandwidth-limited pulse here. Instead, using intra-pulse DFG will allow us to mix spectral components that do temporally overlap inside the crystal. As long as their spectral phase is well-behaved in spectral parts where the process is phase-matched, the resulting DFG pulse will be generated with an almost flat spectral phase. Using this, we can significantly improve the pulse contrast. Since SPM does lead to a modulated phase around the fundamental, DFG is used to mix the spectral wings in our application. This is why XFROG is a very appropriate measurement technique here, as it shows the temporal overlap of spectral components and their continuous group delay.

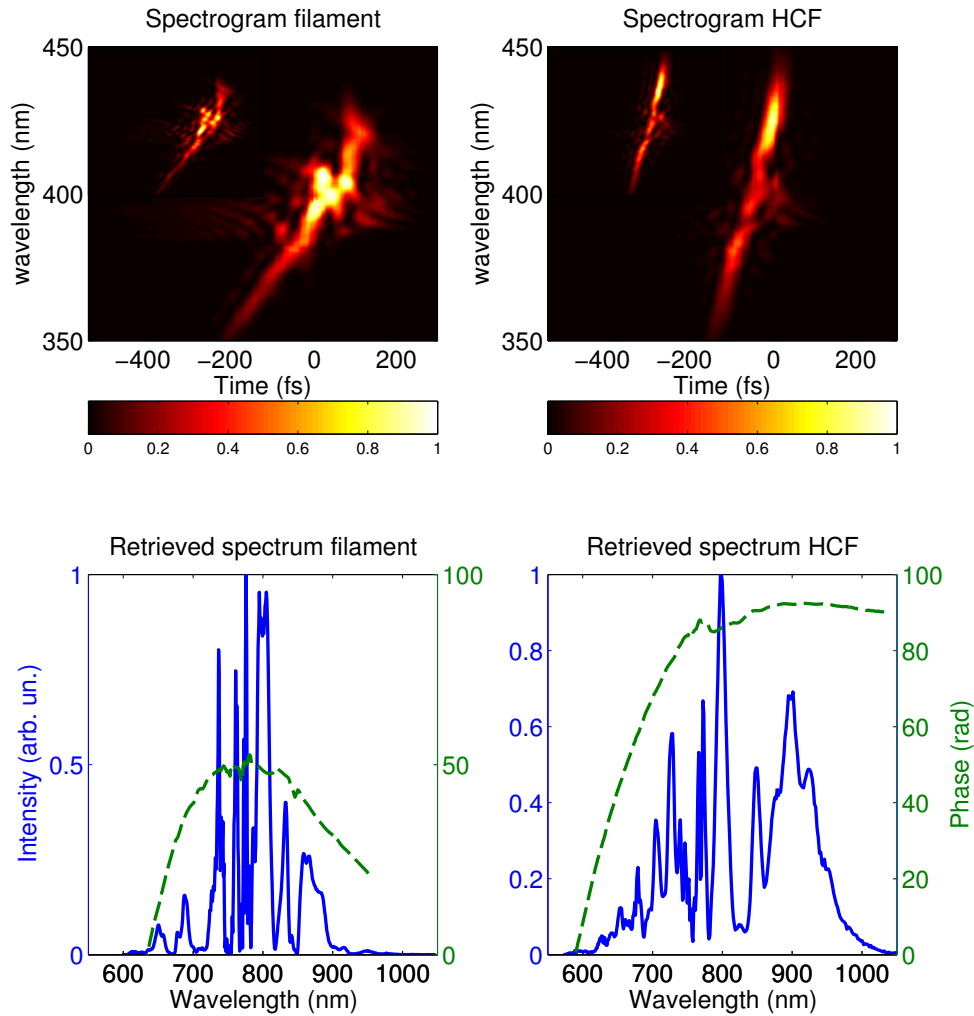


Figure 2.6: SFG XFROG of filament (left) and HCF broadening (right). The insets on the upper left show the retrieved spectrograms.

In another investigation, XFROG measurements were also performed while changing the pressure for both types of broadening. It turned out that the HCF left the resulting chirp much more constant. This can be understood, as the pressure does not only change the nonlinearity and dispersion of the medium, but also determines the spatial self-trapping in case of the filament. Depending on the parameters this can lead to a longer filament and more broadening. On the other hand, the HCF did not broaden any more when increasing the pressure. As the dispersion of inert gases is not very high, the resulting chirp therefore is more sensitive to pressure for the filament.

Altogether, the HCF seemed the better choice for seeding DFG. We will see in the next section, that the generated bandwidth in DFG is even much beyond what is needed for the OPCPA of chapter 5. Therefore using a filament may be just as appropriate for more narrowband (or deeper IR) DFG, given the right optimization.

In the next step, double-angle chirped mirrors (PC70, coated in our group by Volodymyr Pervak) were introduced with an almost constant (but slightly oscillating) GDD of -50 fs^2 . The fact that the TOD cannot be exactly compensated is not important, as the DFG crystals themselves are quite dispersive. Therefore pre-chirping and group velocity mismatch of blue and red components in the crystal will lead to an overlap during propagation. Furthermore we introduce thin glass wedges to optimize the amount of pre-chirping. While the short-wavelength components of DFG are only generated when the most distant spectral parts of the continuum overlap in time, the longer wavelength components can be generated from components that are less distant and therefore naturally experience less group velocity mismatch (even though they may be polarized on different crystal axes). This is why the resulting chirp of the DFG IR pulse may slightly change, but can be compensated for by the acousto-optic programmable dispersive filter (AOPDF) used directly after DFG.

2.4 Phase-stable infrared seed generation

The ultrashort, broadband pulses obtained in section 2.3 are the tool of choice to generate a seed for the IR OPCPA as they are optically synchronized with the pump pulses after the HCF. The process of inter- or intra-pulse difference frequency generation (see fig. 1.1) can then be employed for the generation of broadband and phase-stable spectra in the IR [19], as discussed in section 1.1.1.

2.4.1 DFG using PPLN

The intense white light pulses from section 2.3 are focused by metallic optics onto the DFG crystals. Here a PPLN with a poling period of $11.2 \mu\text{m}$ was used at room temperature. The DFG process is only effective as long as the phase-matched fundamental frequency components overlap in the crystals, limiting the output of the blue difference frequency parts. This leads

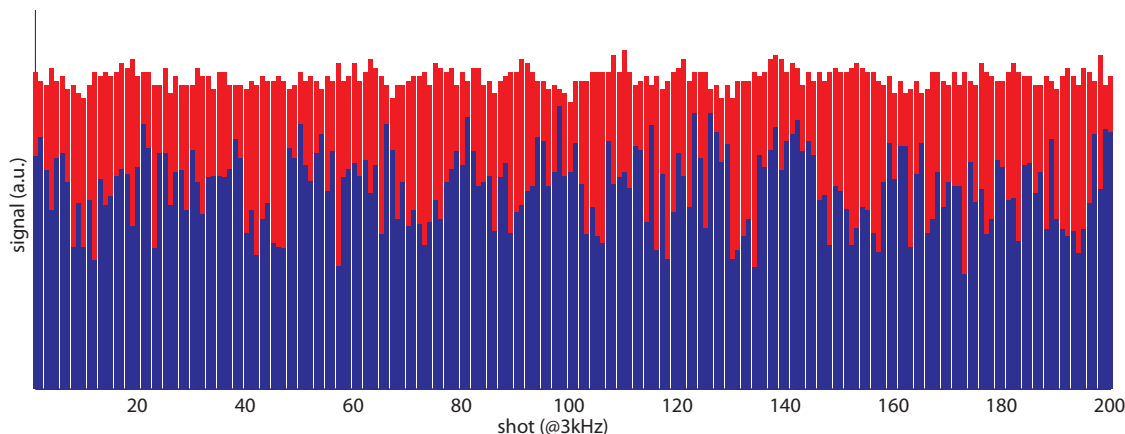


Figure 2.7: Intensity of frequency components in the NIR, taken for 200 shots at 3 kHz with an extended InGaAs diode. Blue bars were measured with $f = 150$ mm focusing, red with $f = 300$ mm focusing (and consequently reduced intensity).

to an effective length of the periodically poled lithium niobate (PPLN) crystal of only a few $100 \mu\text{m}$. Self-phase modulation (SPM) however is inherently phase-matched and will generate broadened fundamental spectra over the whole crystal length. It was observed that as the fundamental is not passively phase-stable and has the same polarization as the difference frequency (see section 1.2.2), both the red tail of SPM and the bluest difference frequencies will overlap in spectrum and time. This makes the generated signal unsuitable for stable OPCPA seeding, as a very fast $f-0$ beating (shown in fig. 2.7) between both fundamental and DF results in the near infrared. It was recorded using an oscilloscope and an extended InGaAs photo diode (DET10D/M from Thorlabs) after suitable bandpass filters. The beating could extent to spectral components up to $2 \mu\text{m}$.

However it can be stabilized by phase-locking the Ti:Sapphire oscillator, rendering the SPM phase-stable as well (still, some slow drifts do remain after the amplifier, since we do not use a slow feedback loop). Figure 2.8 shows the signal for the phase-locked oscillator, making the beating between SPM and DFG parts visible. As the fringes do disappear for a free-running oscillator (and drift when glass is introduced before the PPLN), this is already prove of a phase-stable seed generation (using DFG). However, since the Ti:Sapphire amplifier was not phase-locked by the slow loop (as we do not feed it any signal in our setup), we cannot make any conclusions about the jitter of the DFG phase. Also the delay between SPM and DFG cannot be varied considerably inside the PPLN.

We carefully optimized the focusing (longer focusing favors DFG over SPM) to suppress the SPM onset of the used spectrum starting at about 1550 nm . This was done by observing the generated signal behind a bandpass filter around the blue spectral edge of the OPCPA (NB-1600-033 nm from Spectrogon filters) with the photo diode. The instability of the generated DFG output could be optimized to 3.0% (red bars in fig. 2.7, concave $R = 600$ mm focusing mirror),

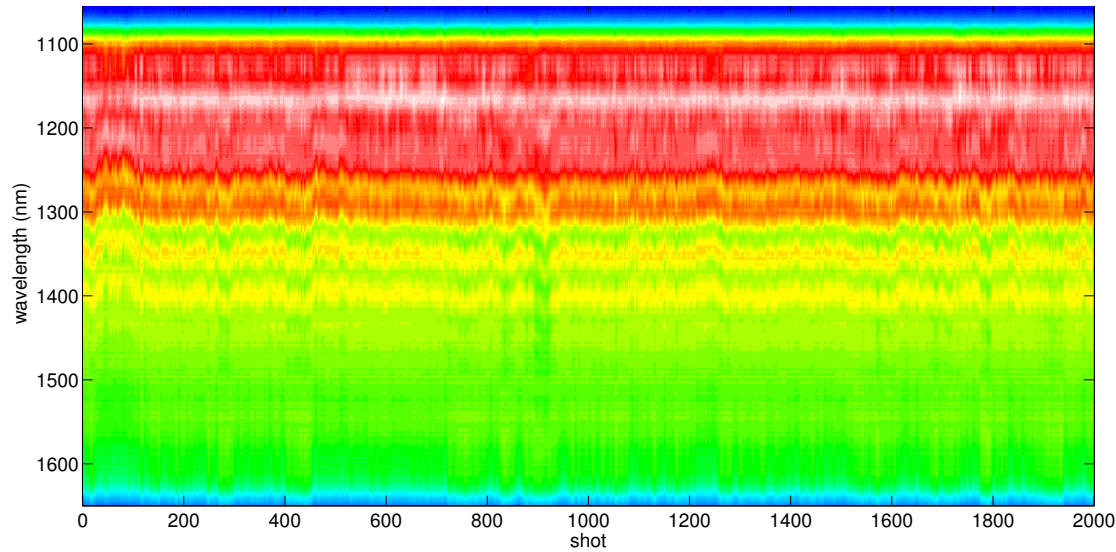


Figure 2.8: Spectrally resolved interference observed between DFG and SPM in a PPLN. Note that both signals have the same polarization, hence the non-perfect contrast. The Ti:Sapphire oscillator was locked to obtain a CEP-stable SPM spectrum and the resulting fringes.

whereas stronger focusing lead to a RMS intensity fluctuation of 18.7% (blue bars, concave $R = 300$ mm focusing mirror). Also limiting the red tail of the white light spectrum by a change of gas pressure or the use of a bandstop mirror proved helpful. The latter one however decreased the used input energy at the same time. The DFG proved very sensitive to a change of the input pulse duration, whereas SPM remained constant. Figure 2.9 shows the blue part of the generated DFG spectra. In order not to oversaturate the spectrometer, the signal is measured behind a piece of silicon, causing the sharp drop around 1050 nm. For little intensity (violet, intensity adjusted by aperture before focusing), the DFG spectrum starts at about 1100 nm and stops at the detection limit of the InGaAs spectrometer at 1700 nm (RED-Wave NIR from Stellarnet). Larger intensities make the DFG signal saturate, while at the same time the SPM part (that was previously not visible after the silicon filter) becomes more pronounced. Since both signals cannot be distinguished by polarization, the PPLN was replaced by a bulk (z-cut) piece of MgO-doped lithium niobate. The crystal should not exhibit any phase-matching in this orientation. The resulting self phase modulation is shown as the dark gray curve in fig. 2.9. Note how the frequency components reach deep into the NIR, leading to the relatively deep modulations in fig. 2.8 and strong intensity fluctuations in fig. 2.7.

Large intensities on the crystal did not only lead to detrimental SPM, particular to lithium niobate and lithium tantalate is also photo-refraction, especially at shorter wavelengths (see section 1.2.3). Looking at the output beam profile of the fundamental with a CCD Camera (Wincam D, Dataray) reveals a distorted beam profile when the aperture in front of the PPLN (or PPLT) that limits the input beam size (and intensity) is opened too much (see insets of fig. 2.9). Observing the generated DFG signal at the same time with the extended InGaAs diode revealed that

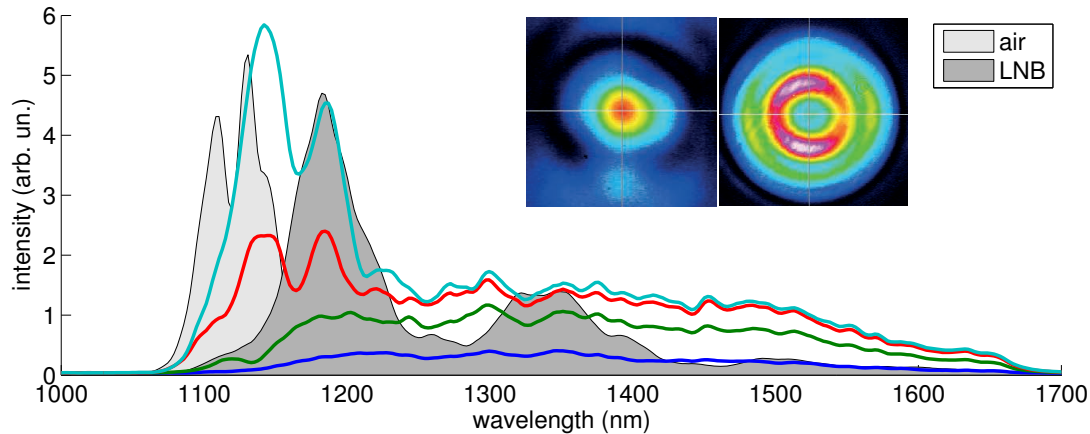


Figure 2.9: DFG signal for increasing intensities on the PPLN are plotted in color. In grey, SPM in a bulk lithium niobate crystal of identical length and doping and air is shown (not to scale). The inset pictures show the beam profile distortions for low (left) and high (right) intensities on the crystal.

when the distortion becomes visible, the DFG signal starts to decrease again.

However, the beam profile of the difference frequency was still homogeneous, as characterized by a razor-edge method (and visible after OPA amplification). The divergence of the difference frequency beam was subject to the input intensity however. Therefore the collimating concave mirror (concave $R=350$ mm) after the crystal needs to be aligned carefully to a spot size of about 3 mm (for still fitting through the AOPDF crystal with an aperture of 5 mm). Collimation to less than 1 mrad is needed for the AOPDF to work precisely [33].

Since the amplified level was too low to characterize the generated pulse directly, the first stage of the OPCPA described in chapter 5 was used to pre-amplify the signal to about 1 μ J. Using a lock-in amplifier and a pyroelectric detector, the signal energy before the AOPDF was measured to be 7 nJ before amplification. The AOPDF was set to be almost self-compensating (see section 4.2.2) in order to observe the amplified DFG signal with little additional chirp (some stretching was needed in order to pre-amplify efficiently).

In order to characterize the spectral phase of the amplified seed pulse, an XFROG setup was used. A small percentage of the Ti:Sapphire amplifier (see section 2.1) was split off and characterized using a SH FROG. It acts as the reference pulse. Via SFG (20 μ m thick BBO cut at $\theta = 25^\circ$) the IR pulse can conveniently be transferred into the visible and the rough group delay can be estimated from the spectrogram. SFG maps the spectral range from 1500 nm – 3000 nm to approximately 520 nm – 630 nm assuming a narrow-band 800 nm reference. We can easily phase-match over one octave using this setup, in section 2.4.2 it will even be used to phase-match nearly two octaves.

The result of the measurement is shown in fig. 2.10. The seed pulse is stretched after amplification using 1.5 mm silicon to observe the background more clearly. There is obviously no clear

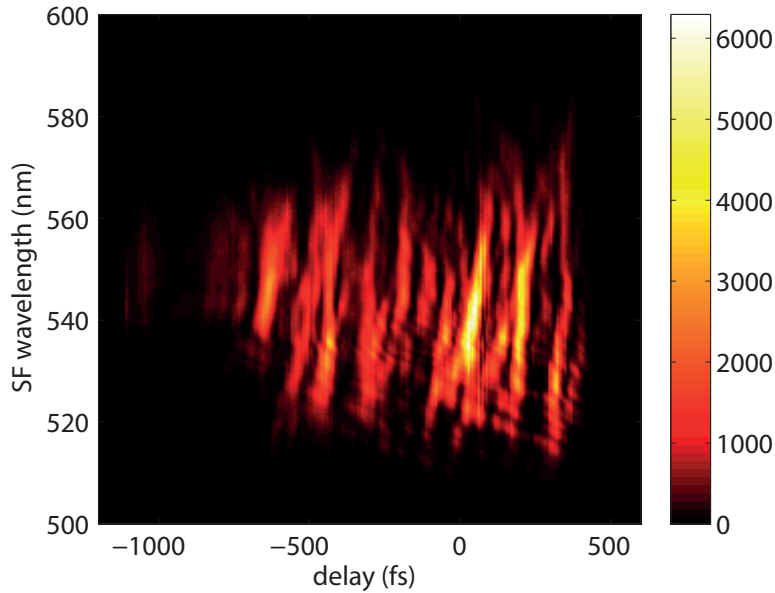


Figure 2.10: XFROG spectrogram of the amplified DFG idler generated in a PPLN.

group delay structure and the background is heavily elevated. It spans all over the pump window. Also all efforts to characterize the phase and compress the pulse using the AOPDF did not succeed. Switching to a PPLT did not significantly improve the situation. We can only explain those severe pulse distortions by the photo-refraction of the PPLN, that destroyed the temporal profile at much lower input intensities than what led to the spatial distortions seen in the inset of fig. 2.9). Using less input power did improve the temporal contrast, but as too little input for the DFG process did not result in detectable amplification any more, this scheme of seed generation was abandoned.

2.4.2 DFG using BBO

Since the temporal structure of the DFG pulse from the PPLN in the last section was not acceptable, an alternative approach was needed. As reported in [55], DFG in a BBO crystal was achieved with high efficiency and an octave-spanning phase-stable spectrum. While their approach contained two arms, using a strong pump and a weaker (OPA-amplified) broadband seed, the idler in this slightly non-collinear scheme can only be kept from experiencing angular dispersion to a certain amount.

Therefore the broadband white light was employed for pump and signal in our scheme (see also [34]). This offers many advantages like perfect pump-seed synchronization and no angular dispersion on the idler output. At the same time it can be very effective at over 10% [34] conversion efficiency. As type-I DFG in the 1 mm thick BBO ($\theta = 29.2$ deg, $\phi = 90$ deg) requires the pump in the extra-ordinary and the signal in the ordinary axis, we simply tilted the crystals to about

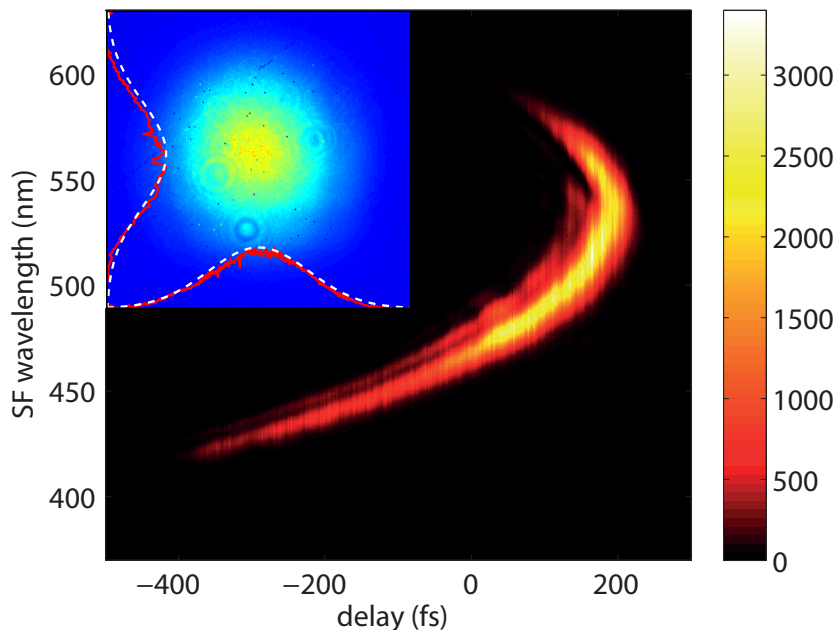


Figure 2.11: XFROG spectrogram of the DFG idler generated in a BBO crystal. Also compare to fig. 2.10. The inset shows the beam profile.

45 degrees between respective polarizations and optical axis (angle as projected onto the crystal surface). Rotation of this axis allows changing of the projections in both axes and more pump/signal amplitude to be used. The generated idler shares its polarization with the signal. Using a periscope at about 45 degrees allows the polarization to be rotated back for the AOPDF. With the much larger damage threshold, the lower n_2 of BBO (see table B.1) and the shorter crystal compared to section 2.4.1, an overall output of about 500 nJ could be achieved, while SPM remained very low. This output energy is far beyond the level reached using PPLNs or PPLTs like in section 2.4.1.

The same XFROG setup as in the last section was used to characterize the pulses. However, it was soon discovered that without using the AOPDF (which is quite inefficient when self-compensating, as discussed in section 4.2.2), the pulses were intense enough to be characterized directly without pre-amplification. The spectrogram is shown in fig. 2.11 and shows an exceptionally well-defined phase that is curved around the zero-dispersion point (ZDP) at 540 nm (SFG) ($\approx 1.7 \mu\text{m}$) and reaches from 420 nm (SFG) ($\approx 880 \text{ nm}$) to 600 nm (SFG) ($\approx 2400 \text{ nm}$), spanning significantly more than one octave. The ZDP of BBO is lower (see table B.2), however several meters of additional air path (from the XFROG setup) can shift this point to longer wavelengths.

While the selected spectrogram was the most broadband, angle tuning allowed moving its center more into the long-wavelength regime, where the OPCPA amplification spectrum is located. Also spectral clipping by limited SFG phase-matching and IR BBO absorption cannot be excluded. Still the OPCPA of chapter 5 proved to be sufficiently seeded by this source. The inset

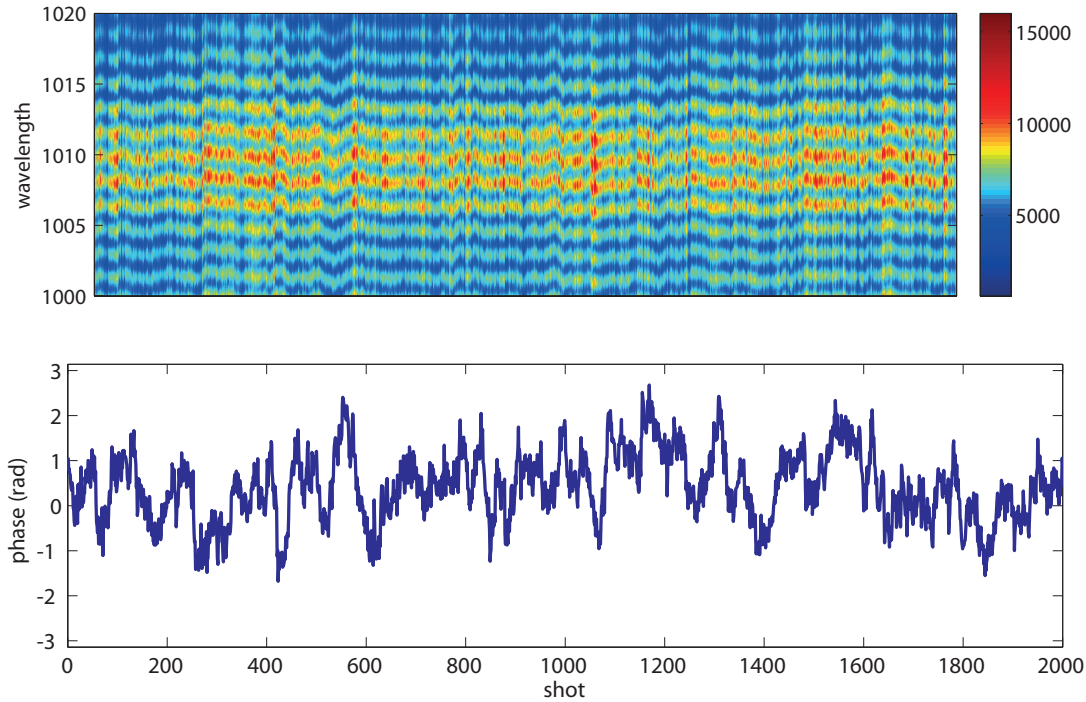


Figure 2.12: f - $2f$ spectrogram of the DFG idler generated in BBO

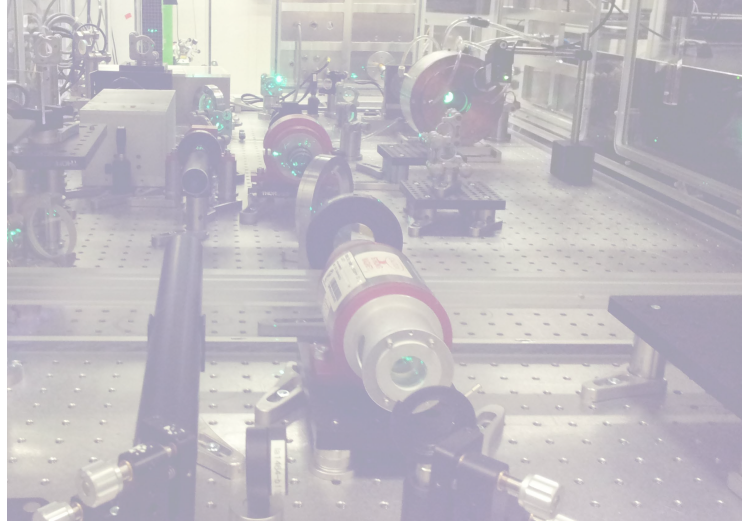
of Figure 2.11 shows the beam profile of the generated idler. Due to spatial constraints, the collimating mirror had to be used at a slightly larger angle, leading to some astigmatism in the beam profile. Diffraction effects on the visible beam like in the inset of fig. 2.9 could be observed as well. However, these occurred at much larger intensities and without negative effect on the idler output in time or space.

In order to confirm the phase-stability of the DFG output, f - $2f$ interferometry was used (see section 1.1.1). For f , the fundamental is taken from the broadband DFG idler around $1\ \mu\text{m}$ (reflected off the silicon stretcher of the OPCPA). The second harmonic ($2f$) is amplified by a first OPCPA stage (as described in chapter 5) to be intense enough for frequency doubling in a BBO crystal. As the OPCPA setup makes the optical path lengths long (7 m respectively), the linear change in path also contributes to jitter in this large interferometer. Figure 2.12 shows the interferogram, recorded over 2000 shots in 245 seconds with an integration time of 60 ms. No measures were taken to optimize the fringe contrast. This should not be necessary, as we do not expect fast jitter components from an inherently CEP stabilized source. Rather, the fast jitter components should be the result of temporal jitter between interferometer arms (see eq. (1.2)).

The CEP jitter is evaluated to be 760 mrad, which is surprisingly little given the large dimensions of the interferometer. As we shall see in the f - $2f$ measurement of the OPCPA itself (see section 5.5), the delay jitter is dominant here, while the CEP stability from DFG is excellent. Therefore this measurement rather proves the phase-stability of the short-wave tail of the spectrum, which is not used any further in this manuscript.

However, a second OPCPA (pumped with the second harmonic of the pump laser) from 800 nm to 1500 nm could be seeded CEP stable from this spectral tail (which, according to the spectrogram of fig. 2.11, contains several 100 nJ of pulse energy). As the interferogram of fig. 2.12 indicates jitter of only 760 mrad around 1 μm (that we can safely assume to be dominated by timing jitter) this is equivalent to no more than 0.7 fs of jitter between both arms. As the main contributions of the jitter even appear at low frequency and the beam paths for the measurement were not covered yet, this should be easy to compensate and allow sub-cycle OPCPA synthesis as described in [58] (where the NIR OPCPA was still actively CEP-stabilized).

It should be noted that type-II phase-matching of the DFG process in BBO is also possible. While being a bit less broadband and efficient, it offers the advantage of signal and pump both being polarized on the extraordinary axis, so the idler can be separated by polarization. For seeding NIR OPCPA this is a great advantage in terms of contrast.



Chapter 3

Pumping OPCPA

In order to reach the required spectral bandwidth for sub-two-cycle pulses around $2.1 \mu\text{m}$ using LiNbO_3 crystals, short pump pulses on the order of few picoseconds have to be used to keep the required pump intensities below the damage threshold (see section 1.2.2 and [132]). A higher pump intensity allows shorter nonlinear crystals and thereby helps loosen the phase-matching constraints.

Because of the relatively high energies required for an OPCPA system to drive high harmonics, the pump laser needs to be able to produce multi-mJ pulses. This requires high peak-power pump pulses that can only be dealt with using the CPA scheme [131] to keep unwanted nonlinearities in the amplifier low.

A further challenge is the low seed energy. Since the OPCPA is optically synchronized, both pump and seed amplifier derive their respective seed pulses from the same broadband oscillator. In our case this Ti:Sa based oscillator emits only pJ pulse energies around the amplification spectrum of Yb:YAG. Therefore a total amplification of $\sim 10^9$ is required for the pump laser, leading to unwanted (chaotic) amplification dynamics. Employing these chaotic behavior then implies consequences for the synchronization of the OPCPA that will be described in chapter 4 in more detail.

This chapter is based on [88] and the PhD work of Tom Metzger [87] who was joined by the author later. Therefore the work published in [88] will only be summarized very briefly for completeness, in order to see the implications in the following chapters. Beyond that, later changes and characterizations performed by the author are described and the implications for OPCPA are elaborated.

3.1 Pump laser for OPCPA

3.1.1 Motivation of the thin-disk concept for pumping OPCPA

Currently the most promising concepts of scaling the average power of few-ps rare-earth-doped lasers are the thin disk [39] (low to moderate repetition rates), Innoslab [112] (moderate to high repetition rate) and large mode area fibers [109] (high repetition rates). Large average powers at any repetition rate require efficient cooling to keep the amplification of the medium high and reduce thermal lensing effects that could otherwise damage the laser. Where thin-disk and Innoslab use optimized gain media and heat sink geometries to maximize heat transfer, fibers benefit from their large surface. While the capabilities for high average power handling are about balanced, large pulse energies induce nonlinear distortions to the spatial and temporal profile of the pulse. Using chirped pulse amplification (CPA) allowed scaling of pulse energies for the last few decades, while keeping the B-integral (see section 1.2.3) low. However the required larger high-efficiency diffraction gratings tend to become very expensive with increasing aperture.

As discussed in [112], the thin-disk concept, originally developed by Giessen [39], shows most potential at moderate repetition rates of few kHz. There, it is the best compromise between high energy and average power as it minimizes the optical path through material, using a few 100 μm thin crystal as the amplification medium with close contact to a heat sink. This allows excellent beam profiles, important for OPA, as the (spatial and temporal) pump profile imprints itself onto the amplified signal. Employing vacuum technology, the crystal would be (almost) the only medium that is used in transmission and therefore provokes unwanted thermal and nonlinear effects. Moreover, due to the cooling concept, the crystal size can be scaled easily (with some limitations given by amplified spontaneous emission [127]). Also the thermal lens remains low, which allows the stable operation of regenerative cavities. As thin gain media lead to fairly low gain (despite strong diode pumping with several kW/cm^2), a regenerative amplifier with many round-trips is especially useful to counter this conceptual weakness.

3.1.2 Pump laser setup

The pump laser setup is shown in fig. 3.1. In order to reach an amplification from hardly 1 pJ (60 μW measured) to 20 mJ, we first use a fiber amplifier (from a collaboration with the Tünnermann group, Universität Jena) to amplify to about 0.5 nJ before seeding a regenerative amplifier with up to 100 round trips. Both amplifiers are encompassed by a stretcher-compressor setup that chirps the amplified pulses to a duration of about 200 ps (FWHM, with gain-narrowing included). This is a compromise between the finite size of the employed gratings and a sufficiently low B-integral (see section 3.2.1).

After reducing the repetition rate by a pulse picker (which is only needed because the regenerative cavity is longer than the seed oscillator cavity), a Faraday rotator discriminates incoming and outgoing pulses in the out-coupling section (marked light green in fig. 3.1). Together with the

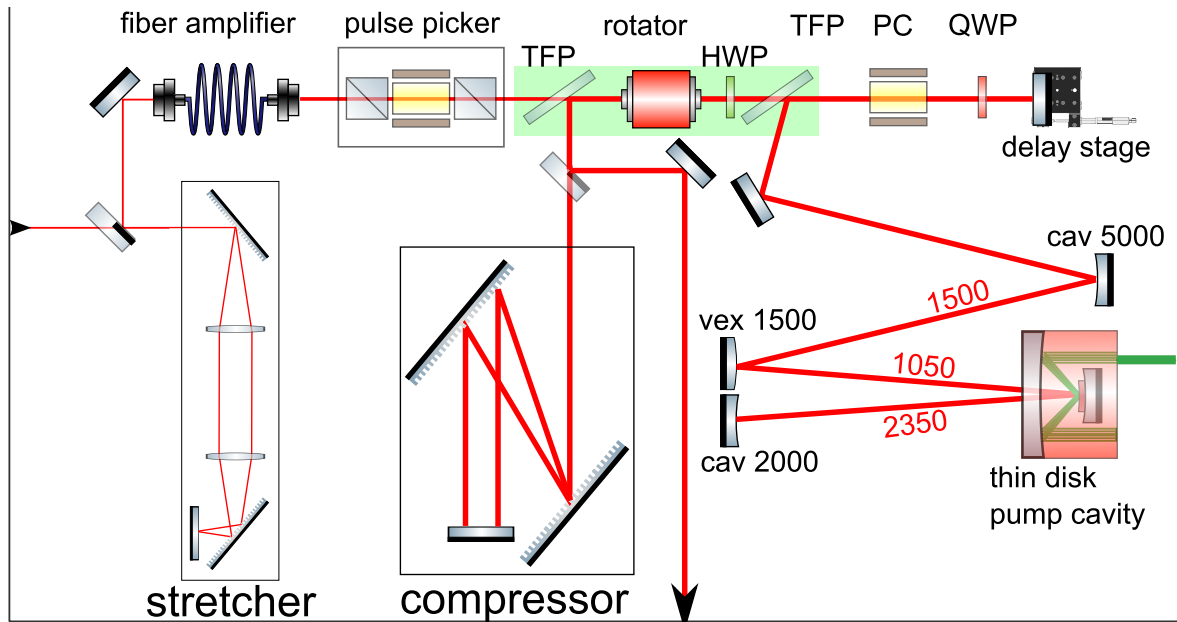


Figure 3.1: The schematic setup of the thin-disk regenerative amplifier. Mirror curvatures and distances in the cavity are indicated. The plotted line width of beam paths represents pulse energy and the out-coupling section is marked in light green. TFP: thin-film polarizer, HWP: half-wave plate, QWP: quarter-wave plate, PC: Pockels cell

thin film polarizer (TFP) that is part of the cavity, these are the only components transmitted with large energy pulses, apart from the thin-disk and the Pockels cell within the cavity.

As soon as the pulses are coupled into the cavity, the Pockels cell (PC) switches on (quarter wave retardation) and closes the cavity. The cavity design was optimized for stable period doubling (see section 3.1.3) and a large spot size on the PC. To reduce the B-integral even more [83] here, a relatively short BBO Pockels cell was used inside the cavity. The switching voltage therefore is very high at about 14 kV. Also enough tolerance for thermal lensing of the disk needed to be considered in order to keep the spot size on the disk large enough and therewith limit the onset of higher order spatial modes (see M^2 characterization in section 3.2.2) by using the pump spot on the disk as a soft aperture.

The thin disk (Trumpf Lasertechnik, Schramberg) is pumped with continuous wave fiber-coupled diodes at a wavelength of 939 nm (indicated dark green in fig. 3.1). A close-to-flat-top spot size of 3 mm in diameter is pumped by around 223 W. Assuming full absorption of the pump light (with the help of the pump cavity also supplied from Trumpf), this leads to a pump intensity of 3.2 kW/cm^2 . After enough round-trips (about 4 to 5 μs) the PC switches off again and couples out the amplified (and gain-narrowed) pulses, ending the amplification cycle. The pulse-buildup during one amplification cycle shows saturation in fig. 3.2.

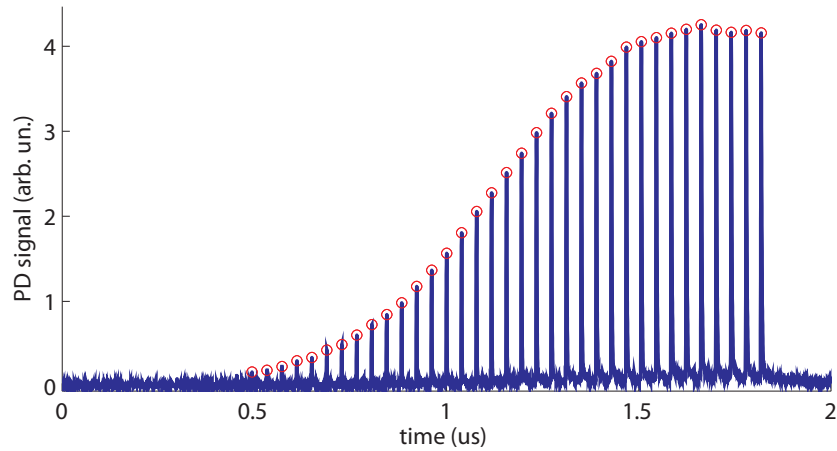


Figure 3.2: The buildup of the amplified pulses in the regenerative cavity. The round trip time is 40 ns. While the total amplification cycle lasts for several μs , only the last few are visible here. Also a build-up of Q-switched unseeded background is visible.

Compression

The grating compressor finally compresses the pulses again; more about the temporal pulse profile is given in section 3.2.1. The used reflective diffraction gratings have a high throughput of about 88%, thanks to the record diffraction efficiency of the gratings (that stem from a collaboration with Fraunhofer IOF in Jena). The stretcher uses a telescope with a magnification of -1 to invert the usually negative dispersion of grating compressors [85]. The gratings in both stretcher and compressor have the same line spacing of 1740 lines/mm, so even higher order chirp between the stretcher and compressor should be compensated [92]. The absolute amount of dispersion for both stretcher and compressor is $D_{CPA} = 7.9 \cdot 10^7 \text{ fs}^2$, therefore the contribution by optical components in the amplifier (the major one being the 20 mm long BBO crystal with $D_{BBO} = 1.9 \cdot 10^5 \text{ fs}^2$) is almost negligible in comparison. This means that the round trip time can be altered without re-optimization of the grating compressor.

Safety mechanisms

With the operation in heavy saturation (of the pump average power) arises a potential damage issue for the whole amplifier; as soon as the seed pulses would stop depleting the gain medium, the usable inversion inside the disk increases to levels that are never seen in continuously seeded operation. A potential heavily amplified first pulse at this inversion could (and in reality, did) damage optical components.

To avoid that, a fast photo diode (135 ps rise time, to resolve the internal pulse train shown in fig. 3.2) was set up for some leakage beam through the flat end mirror (shown in fig. 3.1) to monitor the intra-cavity intensity. A second delay card was triggered at a critical threshold level

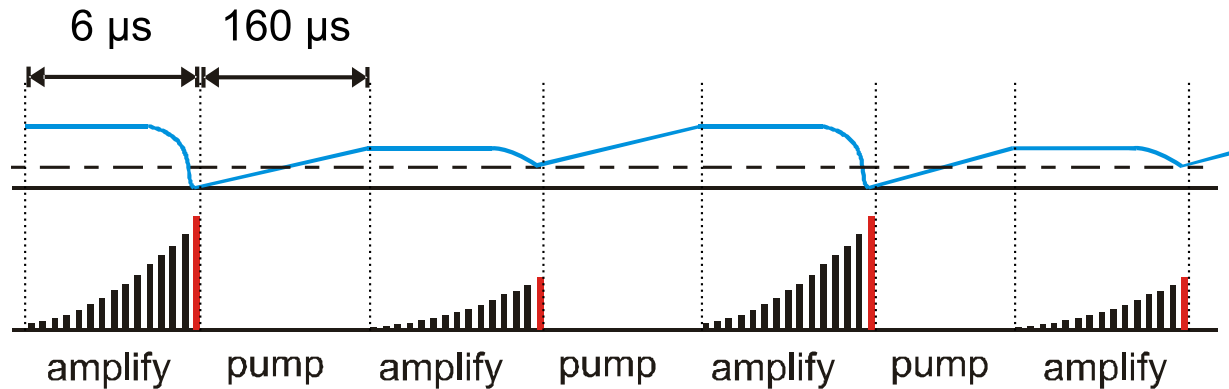


Figure 3.3: The amplification cycles in the regenerative amplifier see the gain medium's history (inversion, shown in blue). Gain depletion (caused by large amplified pulse energy) can then lead to period doubling and stabilize the otherwise chaotic behavior. In the lower column, the intra-cavity pulse-buildup is shown in black and the ejected pulse is marked red.

where it prematurely ended the amplification cycle by switching off the Pockels cell within about three round trips ($\tau_{RT} = 40$ ns). This way, excessively high pulse energies could be avoided, independent of the source.

However later this solution turned out to be too time consuming. As a simpler approach, the (master) delay card of the amplifier (shown in fig. 4.1) was then triggered by a photo diode, illuminated with a part of the seeding pulses. In case of missing signal, it left the Pockels cell driver at a constant voltage (unswitched) so the cavity was no longer closed. This safety mechanism proved to be appropriate for potential problems with the seed.

3.1.3 Chaotic behavior of cw pumped regenerative amplifiers

The high gain in the regenerative cavity leads to a chaotic pulse-buildup for consecutively seeded pulses. This actually limited the usable energy from thin-disk regenerative amplifiers before, see [93]. However, stable (intermittent) regimes in this chaos can be identified, where only each second pulse experiences significant gain. This is illustrated in fig. 3.3, where only each second amplification cycle experiences full inversion and therefore the amplified pulse reaches the full pulse energy only at half the repetition rate, leading to so-called period doubling.

To the authors knowledge, this was investigated before [29], but not taken advantage of yet. These chaotic effects in rare-earth doped lasers were discovered rather late, since they occur at a repetition rate around the inverse of the upper laser level lifetime [29, 44]. As the system is driven in resonance there, even larger reductions in repetition rates may occur.

As intermittent regimes (with the large amplified pulse containing most of the energy) occur far in the saturation of the intra-cavity pulse buildup, the pulse-to-pulse fluctuations are minimized as well. Figure 3.4 shows the pulse energies measured after amplification when increasing the

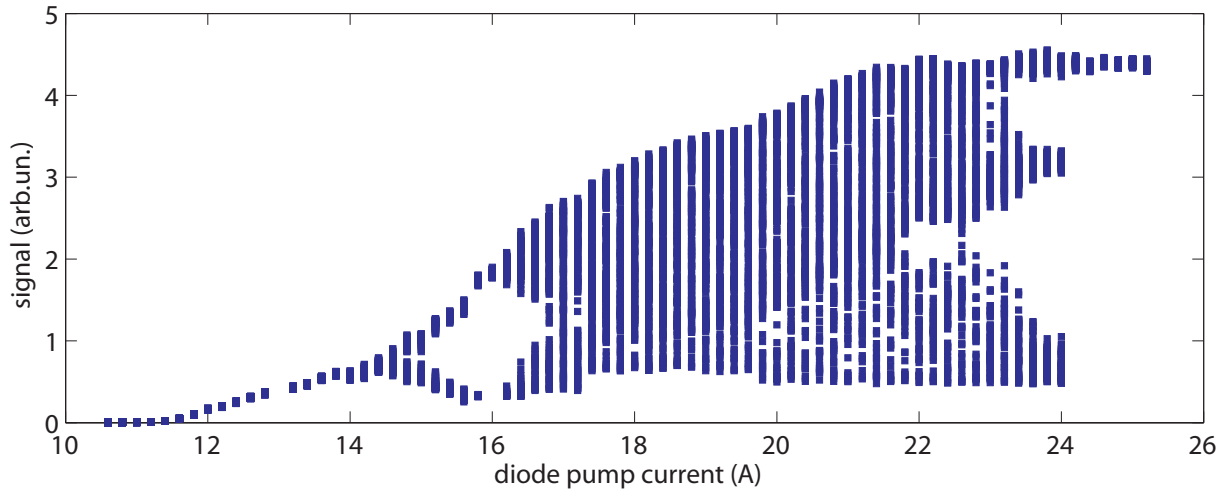


Figure 3.4: The output pulses plotted over the current of the pump diodes. Notice the bifurcation appearing at 15 A, the chaotic region up to 23 A and the intermittent regime thereafter. Over 24 A only the strongest pulses are significantly amplified, whereas the other half is experiencing too little gain.

diode current. At around 14 A, the pulse energies split up. This is the situation illustrated in fig. 3.3. When pumped even higher, deterministic chaos occurs beyond 16 A, where every pulse energy depends on the last one. Finally, for large energies over 24 A, depletion keeps the weaker pulse from significant amplification, the period of the amplifier has doubled. So in order to supply pump pulses at 3 kHz, the whole laser needs to be electronically driven at 6 kHz.

The chaotic behavior is due to the coupling of the individual amplified pulses. For low repetition rates or pulsed (QCW) pump diodes (that are currently not available at these high repetition rates), the coupling would be heavily reduced. However, the upper-state lifetime of Yb:YAG is very high at 951 μs [76] even at room temperature, and therefore CW pumping is more efficient. For Ti:Sapphire, period doubling occurred recently in a CW-pumped regenerative amplifier as well [145], but at higher repetition rates (as the lifetime is only 3.2 μs). As the doubling regime was avoided there, the amplifier could not run in saturation and both stability and efficiency were sacrificed instead.

3.2 Short characterization of the pump laser

3.2.1 Consequences of high B-integral

Self-phase-modulation (section 1.2.3) is a serious issue, limiting the pulse energy of most modern picosecond pump lasers for OPCPA. While for ultrashort pulses it can be used favorably, when broadening the pulse spectrum (see chapter 2 and chapter 7), for picosecond narrow-bandwidth

and high-energy sources the effects are primarily negative.

In our case spectral broadening is countered by gain-narrowing during amplification and the large chirp of the applied seed pulses, therefore the spectrum will not broaden considerably. However, local hot-spots tend to self-focus with increasing B-integral [76] and lower the damage threshold. Also the temporal structure of the pulse can be significantly impaired. This leads to bad contrast pump pulses or even a strong coupling between pulse duration and intensity, as is shown in fig. 3.5.

The B-integral of the intra-cavity amplification cycle is dominated by air and the BBO of the Pockels cell. Since several round trips are made in saturation at full pulse energy (see fig. 3.2), the B-integral there increases rapidly. However, a certain amount of saturation is necessary to ensure stable long-term operation in the doubling regime. Figure 3.5 shows FROG traces (on a 64x64 grid) taken for the same pump laser configuration, while modifying the pump intensity on the disk and the round trip time in the cavity (to remain in the doubling regime).

The first column in fig. 3.5 shows a pulse measurement at low intensity (with chaotic pulse buildup still). The retrieved pulse duration (FWHM) of 1.5 ps and the well-behaved spectrum (FWHM 1.2 nm) show the behavior for low B-integral in a linear amplifier. In the second column, the pump power was increased to reach stable doubling and drive the regenerative amplifier into saturation. The spectrum is obviously broadened (FWHM 1.5 nm), as is the whole pulse (FWHM 3.8 ps). Even more impressive is the delicate dependence on the round trips (and therefore on the B-integral). In the third column, the round trips are only reduced by four, leading to a significantly shorter pulse (FWHM 1.9 ps). In fact, even just alignment of the cavity (optimizing the amplified output by less than 5%) lead to very heavily changing pump pulse intensities and OPCPA outputs levels. This non-linear behavior is consistent with simulations (that are beyond the scope of this section), and show that the B-integral needs to be kept low for reproducibility in the OPCPA. Limiting the round trips to just 90, as shown in the right column of fig. 3.5 shows some limited spectral broadening in the wings and leads to short pump pulses of 1.3 ps (FWHM). However, in order to reach saturation and stable period doubling with this configuration, excessive pumping of the thin disk is needed (as the total gain needs to remain constant), which leads to thermal effects on the gain medium. This is treated in section 3.2.2. Note how a larger seed energy would allow to reach period doubling at lower pump powers and therefore helps avoid this pulse distortion.

It is especially interesting, how the retrievals of the two center configurations shown in fig. 3.5, are less than ideal. In fact, for large B-integrals the pulse train is expected to fluctuate (due to intensity fluctuations). While in an intensity autocorrelation, this would only show as a large background with a peak resembling a so-called coherent artifact, in multi-shot FROG, we expect a larger FROG error, since we are only measuring the averaged part of a fluctuating pulse, as pointed out very recently [107]. The larger error results from the fact that the spectrogram is over-determined and the FROG algorithm cannot perfectly reconstruct it, as it does not indicate a physically correct pulse. As the temporal structure of the pulse fluctuates from shot to shot however, a single pulse duration cannot be defined for the whole pulse train. Moreover, the synchronization of chapter 4, which employs cross-correlation using the temporal pump pulse

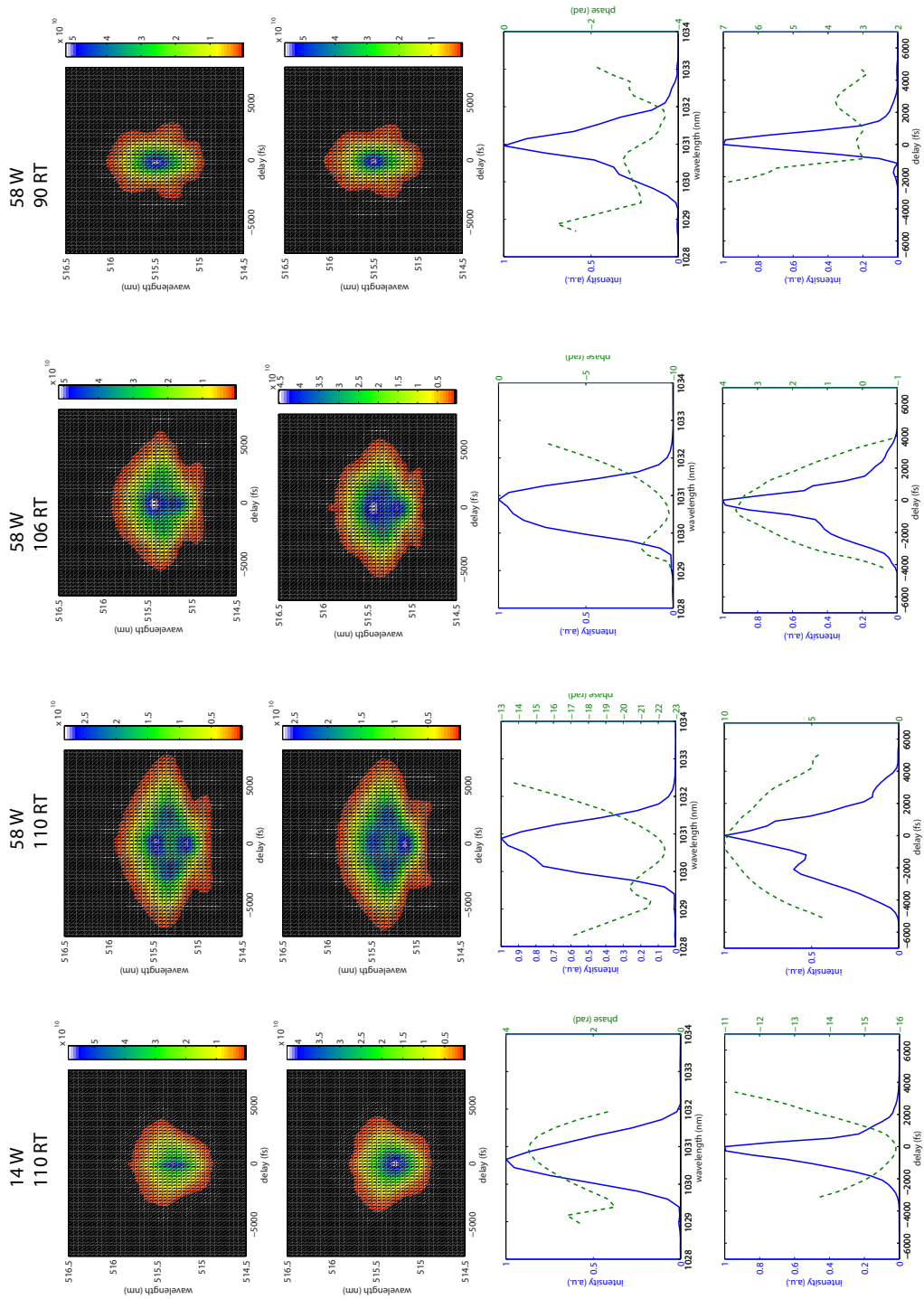


Figure 3.5: SHG FROG traces and reconstructions in spectral and temporal domain for different regenerative amplification settings.

profile (section 4.3.3), can suffer from a fluctuating center of mass. A coupling of intensity to timing jitter is the consequence, which ironically leads to pulse-shape fluctuations in the OPCPA. Therefore this large B-integral regime needs to be avoided for stable operation of the OPCPA.

To reduce the B-integral in the pump laser further, one could think about removing the air (or replacing it by a helium atmosphere) or chirping the pulse more, using larger grating distances (and eventually larger and more expensive gratings). However, further chirping could lead to a linear increase in timing-jitter as well [73]. Therefore, the only immediate solution was to limit the average power a bit, while keeping the saturation low to achieve pump pulse durations on the order of 1.5 to 1.6 ps (FWHM).

As an accumulation of B-integral can lead to optical damage not just in the amplifier but also later in the OPCPA setup, care must be taken to reduce transmissive optics at large intensities in the whole setup as much as possible. This is why reflective optics and large beam diameters in the beam delivery are used for the high-energy amplification stages described in chapter 5 and chapter 7. Transmissive optics proved to be unusable in these stages because of resulting optical damage and very deteriorated beam profiles. As the B-integral (see eq. (1.28)) grows with shorter pump pulses (this means higher intensities with constant fluence), ever shorter pulses will require entire OPCPA systems to be set up in vacuum [72].

It should be mentioned that large B-integral in the OPCPA itself also has detrimental consequences for the CEP stability [19].

3.2.2 Beam profiles, M^2

The beam quality (characterized here by M^2 measurements using the camera-based Spiricon M^2 -200) of thin-disk lasers is typically excellent ($M^2 < 1.1$) as long as higher order transverse modes are kept from lasing in the cavity. In fact the measurement directly after the laser (without compressor gratings) gives values of $M_X^2 = 1.2$ and $M_Y^2 = 1.1$ as long as the pump intensity on the disk is kept low. With more thermal load on the disk however, the surface deforms in a non-spherical manner (see picture d) in fig. 3.6), promoting the appearance of higher transverse laser modes [99] as $M_X^2 = 2.5$, $M_X^2 = 2.0$ and the pictures a) and b) of of fig. 3.6 indicate. Careful cavity design also was seen to result in better M^2 values, which can be attributed to the limited pump spot acting as a soft aperture and the decreased susceptibility of the cavity to resonantly amplify higher modes [99]. The picture (d) in fig. 3.6 is a helium neon laser beam reflected off a (not amplifying) thin disk at high pump intensity. It shows the aspheric surface of the disk that results from excessive pumping, although amplification will extract more energy from the disk in general. Notice that some fringes arise from reflections on the surfaces that are not coated for 633 nm, however, the overall beam distortion is still obvious. De-collimating the fiber-coupled diode pump light (making the edges of the flat-top pump profile less steep) improved the situation, as it reduces the transversal temperature gradient on the disk. Finally, avoiding excessive pump power (on the same pump spot diameter) brought an acceptable beam quality for pumping the OPCPA stages, while sacrificing average power however. Power scaling is therefore

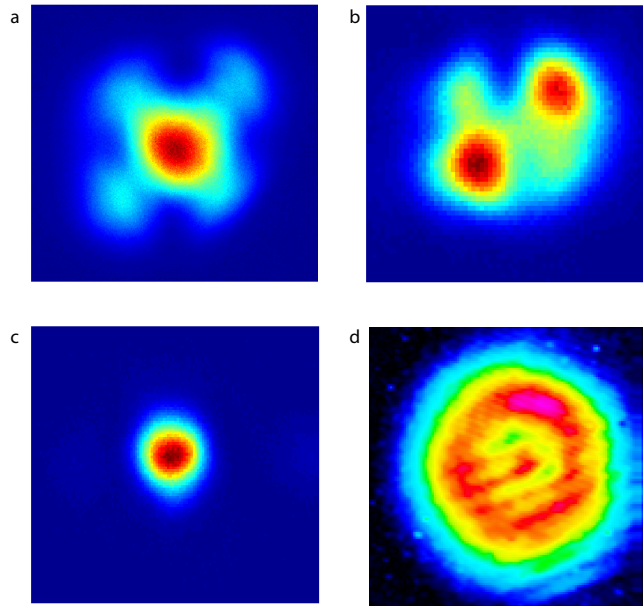


Figure 3.6: Beam profiles for a too intensely pumped thin disk are shown before (a) and in the focus (b). Limiting the pump density on the disk results in good beam quality (c). In (d) the reflection of a pump-induced non-spherical thin disk is shown.

limited; as a larger pumped spot on the disk alone would also enhance higher order lasing, the cavity length would need to be extended further. Other approaches would be to distribute the thermal load over two pumped disks, or to actively compensate the thermally induced aberrations in the cavity [101].

One of the used compressor gratings appeared to be not flat and caused astigmatism in the compressed beam. In a M^2 measurement after the compression gratings, the focusability is therefore also decreased in the diffraction plane (to about $M_x^2 = 1.4$). Figure 3.7 already shows some astigmatism out of the cavity, probably due to non-zero incidence angles on spherical optics. The astigmatism induced by the grating however is much larger in comparison. To compensate for it, a 3 mm thick one inch high reflective mirror was later bent before the compressor. This made the beam profile more symmetric in the following OPCPA stages while avoiding the use of cylindrical optics. The non-perfect focusability is not a concern for pumping our OPCPA, since the pump intensities needed are easily achieved even for large spot sizes and higher order modes did not amplify considerably through the OPCPA stages. This is confirmed later in section 7.3, where coupling the OPCPA output into a hollow core fiber proved highly efficient (using high quality OPA crystals).

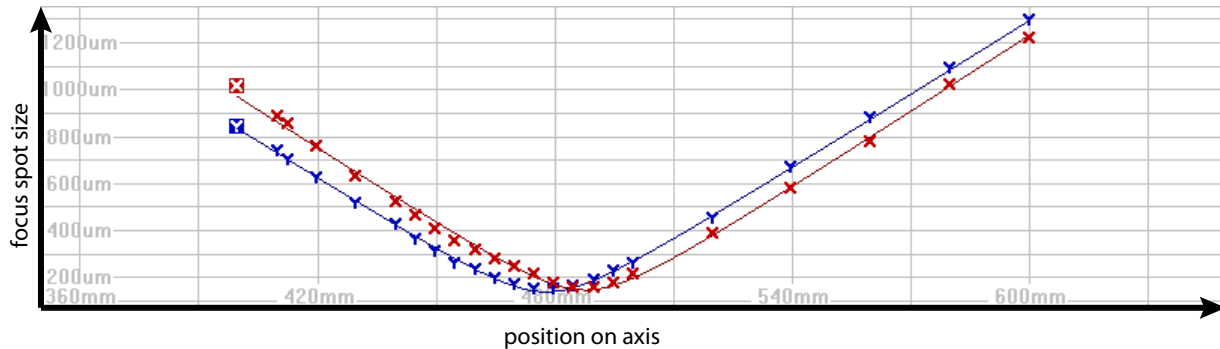


Figure 3.7: M^2 measurement of the pump laser before compression. The vertical axis indicates the spot size (calculated using the 4σ method) and the horizontal axis marks the position along the focus. Notice the slight astigmatism that already arises from the cavity.

3.2.3 Beam pointing

Stable beam-pointing is especially important in our OPCPA setup, as we do not want to rely on relay-imaging which would require (lossy) vacuum cells and put strong restrictions on the pump beam paths. Moreover, spatial jitter would also necessarily lead to temporal jitter in the OPCPA crystal as pump and seed are derived from different sources. Also a slow drift of the beam position is detrimental to the stable operation of the OPA system over extended periods. As the pump laser angular beam pointing was characterized to be $4.38 \mu\text{rad}$ (see fig. 3.8), the long pump delivery paths lead to a significant lateral offset of the pump spot. Even worse, as we need to reduce the beam size by a telescope in the second and third stage of the OPCPA, the angular magnification increases the amount of angular fluctuations further. Poor and fluctuating spatial overlap in all three stages would accumulate and induce considerable instabilities. Even an active delay stabilization (see section 4.3) would derive an incorrect delay, as it depends on good beam pointing of both pump and seed lasers in (at least) the diffraction direction of the dispersing grating (see section 4.3.5). As spatial and temporal jitter correlate differently in every OPCPA stage, they cannot be compensated somewhere in between OPCPA stages, as this could even deteriorate the situation somewhere else. Instead, beam pointing needs to be reduced first, before the optical pulses from both pump and seed are overlapped in the delay stabilization for the first time. Then subsequently all stages will experience improved performance.

To reduce the beam pointing of the pump laser, an active commercial stabilization (Aligna 4D, TEM Elektronik) was used. It employs two position sensitive detectors with sample & hold electronics (details see section 4.3.5) to measure both lateral position and direction of the beam. The circuits were triggered externally to make sure only the right pulses are detected when in the doubling regime. These error signals are then fed back to analog PID regulators. Two piezo-driven actuators, fixed on a stepper-motor driven mirror mount are driven by the regulator, the stepper-motors merely center the piezo voltage. For improved performance, balanced piezo actuators (that means both actuators are acting against each other) were chosen as they proved to experience much less mechanical hysteresis. Therefore the feedback loop is working much more

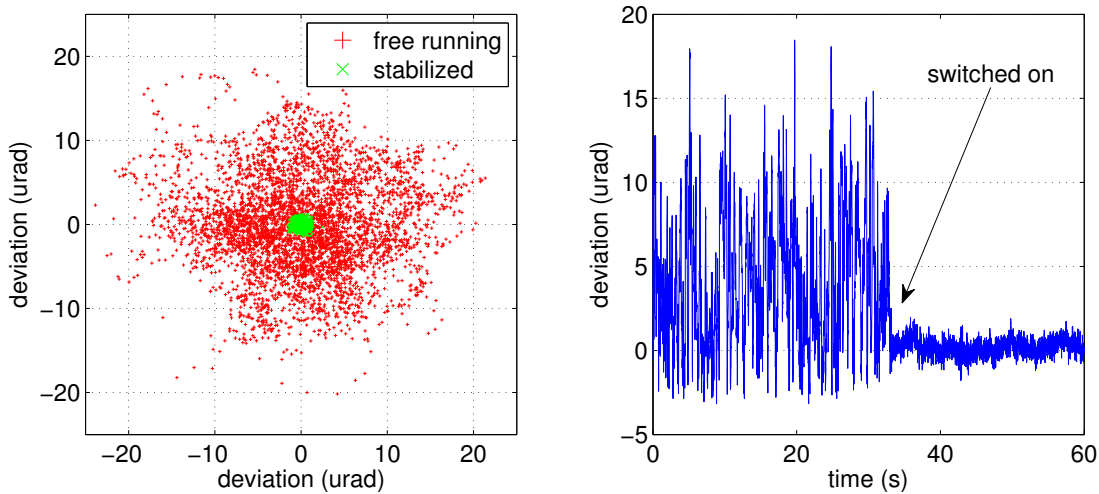


Figure 3.8: Angular beam pointing of the pump laser before being delivered to the OPCPA. On the right, the angular deviation is minimized when an active beam stabilization is switched on.

efficiently, although the resonance frequency of the piezos did not increase significantly. As the main source of disturbance for beam pointing is the pump laser cavity itself, the compensating beam stabilization mirrors were put as close to the outcoupling section (marked light green in fig. 3.1) as possible. Small mirrors were used at normal incidence to keep the optics weight low and to not reduce the resonance frequency too much.

The results of the active stabilization are shown in fig. 3.8. They were measured under the same conditions as described in section 2.1. Before active stabilization, the beam pointing was $4.38 \mu\text{rad}$, after it was reduced to $0.30 \mu\text{rad}$. Notice how thanks to more rigid mounting, the pointing in both dimensions is very comparable, as opposed to fig. 2.3.

Although the stabilization can work over an unlimited amount of time, some detection issues may result in a small drift of the error signal, and consequently, the pointing. As the divergence of the beam can change by a drift in thermal lensing of the pump laser, the second detector (located in the focus of the beam to observe the beam direction) will add some lateral position to the pure direction reading. This would lead to a shift in both direction and position.

Chapter 4

Synchronizing OPCPA

The synchronization of OPCPA is crucial, since pump and seed pulses need to interact in a very controlled manner to ensure a stable parametric amplification in terms of spectrum, energy and CEP. It can be divided into the electronic and the optical domain. Where in the first domain we need to control the pulse overlap within one oscillator clock cycle (approximately 14 ns for a 70 MHz oscillator, see section 2.1), the latter needs to be stabilized to a small fraction of the pump pulse duration (ideally much less than 10% [36]). This means a jitter in delay of $\ll 150$ fs is needed.

A part of the following work was published before in [119] by the author. However, more aspects (especially those affecting the OPCPA operation) are treated in this chapter.

4.1 Electronic synchronization

4.1.1 Timing hardware used

The electronic synchronization is technically not very challenging for an optically synchronized system, given that current delay equipment [128, 8] routinely offers timing jitter of less than 100 ps. Within this precision, Pockels cells and their drivers will usually experience ringing and other transient side effects anyway. Our electronic delay equipment is based on BME_G05p delay cards from Bergmann Messgeräte, Murnau. Figure 4.1 shows how the three sets of delay cards (for seed laser, pump laser and OPCPA) are connected to trigger all necessary devices for OPCPA operation.

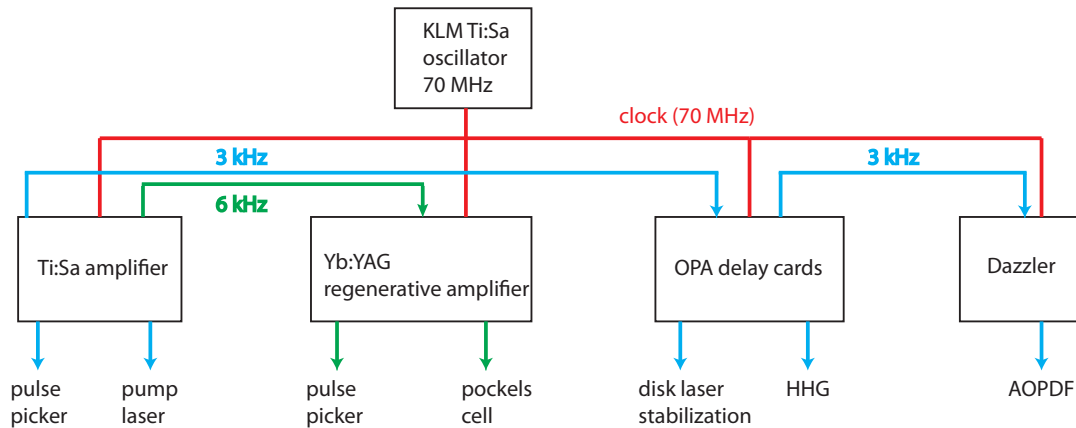


Figure 4.1: Devices included in the electronic synchronization

4.1.2 Seed laser

Ti:Sapphire has a short upper laser level lifetime, therefore it is typically pumped by pulsed frequency-doubled Q-switched lasers for few kHz repetition rates. Also multi-pass amplifiers require a pulse picker to amplify single pulses. Both pulse-picker and pump-laser are triggered by electronic pulses that are generated from a set of delay cards synchronized to the external oscillator (clock) running at 70 MHz.

4.1.3 Pump laser

The disk laser is CW pumped, because Yb:YAG can store pump energy well as the upper laser level lifetime is comparable to the inverse repetition rate. However the regenerative cavity is longer than the cavity of the oscillator (40 ns vs 14 ns), making a pulse picker necessary. Both the Pockels cell (that closes the regenerative cavity) and the pulse picker are triggered from a 6 kHz signal derived and replicated from the Ti:Sapphire delay cards.

The alternative pulse heights emitted from the Yb:YAG amplifier in Figure 4.5 (smaller pulses exaggerated) indicate the laser is running in period doubling. That means while all electronics are internally running at 6 kHz, the pulses that experienced less depleted gain are amplified at 3 kHz (see section 3.1.3). These pump pulses are synchronized with the OPCPA seed pulses as long as period doubling remains running stable. However, perturbations of the pump laser (as well as the oscillator) can disturb the the dynamic of period doubling and lead to the wrong pulses overlapping, resulting in almost no parametric amplification. Therefore, in fig. 4.1 the beam stabilization of the disk laser is triggered by a 3 kHz signal, replicated from the delay cards of the Ti:Sa amplifier, and makes the error in synchronization obvious. As an alternative, an external Pockels cell could be used to filter the correctly timed pump pulses and improve the contrast at the same time by removing prepulses leaking out of the regenerative cavity.

4.2 Dazzler (AOPDF)

4.2.1 Electronic triggering

The delay cards of the OPCPA are replicating the 3 kHz signal from the Ti:Sa amplifier cards for auxilliary devices like triggered cameras, beam stabilizations and an acousto-optic programmable dispersive filter (AOPDF, Dazzler from Fastlite, France).

The AOPDF is special as it contains its own internal oscillator that is locked to an external oscillator frequency and can be triggered by external delay cards (that should also be triggered by the external oscillator). A low jitter < 1 ns in the acoustic waveform generated by the AOPDF is important, as it influences the carrier envelope phase (CEP) of the diffracted optical wave considerably. According to [32], a delay in the acoustic domain affects the temporal domain as: $\tau_{\text{opt}} = \tau_{\text{acoustic}} \frac{6.3 \text{ ps}}{42.5 \mu\text{s}}$ and the phase jitter therefore is given by

$$\Delta\phi_{\text{jitter}} = \frac{2\pi}{7 \text{ fs}} \frac{6.3 \text{ ps}}{42.5 \mu\text{s}} \Delta\tau_{\text{acoustic}} \quad (4.1)$$

where 7 fs is the field cycle period at 2.1 μm . This yields CEP jitter of 130 mrad for 1 ns of electronic timing jitter.

In order to observe the correct PLL settings used in the Dazzler hardware, two measures were taken. First, the output of the AOPDF driver can be monitored directly using a RF attenuator. An example is shown on the left of fig. 4.2, where the PLL settings are not perfect for better illustration. This is how electronic timing jitter $\Delta\tau_{\text{acoustic}}$ in the AOM leads to phase-jitter in the diffracted wave according to eq. (4.1). For better configurations, the timing jitter of the acoustic wave could be minimized below 150 ps (measurement limited by the trigger jitter of the oscilloscope).

Second, in the optical domain, a small Mach-Zehnder interferometer was built that allowed the observation of the CEP and spectral phase of the diffracted pulse using spectral interferometry [106]. On the right of fig. 4.2, the interference fringes between the diffracted Dazzler wave and the reference arm are shown. As the diffraction efficiency is rather low, the modulation depth is limited for the metallic beam splitters available to us. Also spatial chirp from the AOPDF [79] can limit the contrast considerably. The blue fringes on the right of fig. 4.2 indicate correct triggering of the Dazzler electronics. The green fringes show the case of a badly triggered Dazzler, where the CEP during the integration time (50 ms) experiences jitter and the interference fringes are washed out. Note however, that for long integration times the diffracted signal still appears phase-stable, and the fast jitter is not observed after averaging. Therefore the fringe contrast is of special interest when characterizing the CEP stability of the OPCPA in section 5.5.

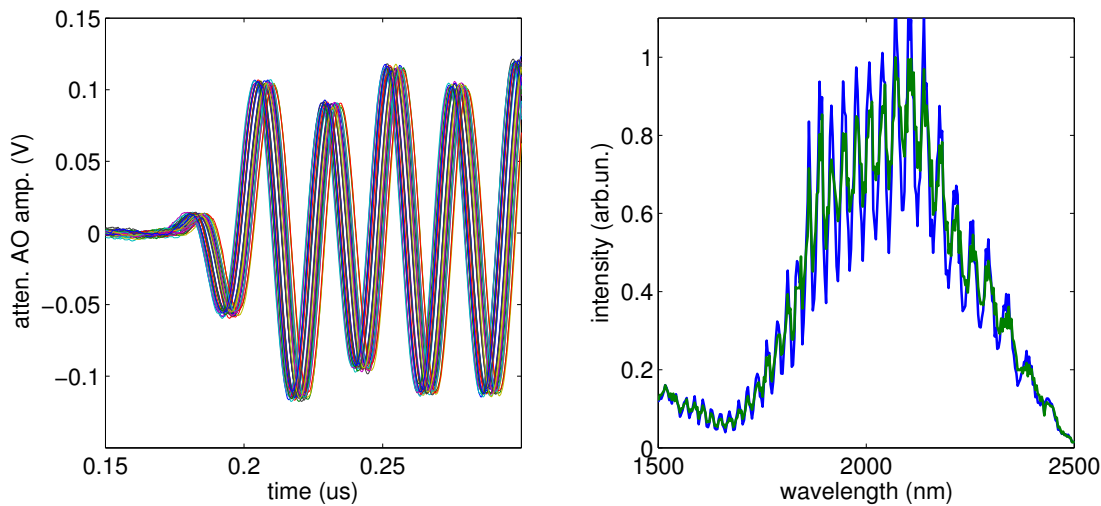


Figure 4.2: Left: The output of the AOM driver when the PLL is not perfectly adjusted. Right: Electronic jitter leads to a fast fluctuating CEP and therefore reduced f-2f fringe contrast with constant integration time.

4.2.2 Dispersion calibration

The spectral interference setup allows the absolute phase of the AOPDF to be measured (given the known phase of the transmitted interferometer components). Since the AOPDF self-compensation function did not work properly from the factory, but left a group delay difference of several ps across the diffracted spectrum, new settings for self-compensation were obtained:

GD (fs)	GDD (fs ²)	TOD (fs ³)	FOD (fs ⁴)
9000	-2350	-25200	70000

These values proved suitable for making the Dazzler approximately transparent, as indicated in fig. 4.3. Also the opportunity was used to compare analytical dispersion values (based on Sellmeier equations that calculated table B.2) with the OPCPA components later used in chapter 5. Shown in fig. 4.3 is the compensation of 5 mm silicon and 2 mm LNB. Since the fringe modulation (shown on the right of fig. 4.2) is limited below 1.8 μm and above 2.3 μm , the GD diverges there, because of spectral filtering in the retrieval algorithm. In the center however, very flat group delay could be obtained by self-compensating with analytical dispersion. This was confirmed by applying the retrieved phase of fig. 4.3 to the AOPDF. While the center flattened even more, the diverging outer parts did not significantly change. Therefore we can conclude that the AOPDF works as expected and the employed Sellmeier equations prove valid and enable us to precompensate for a large part of the dispersion in the OPCPA. While the obtained values were precise enough to build up the OPCPA stages (using appropriate chirp factors for the pump window), fine control of the dispersion was performed later during compression using (X)FROG measurements (see section 5.4).

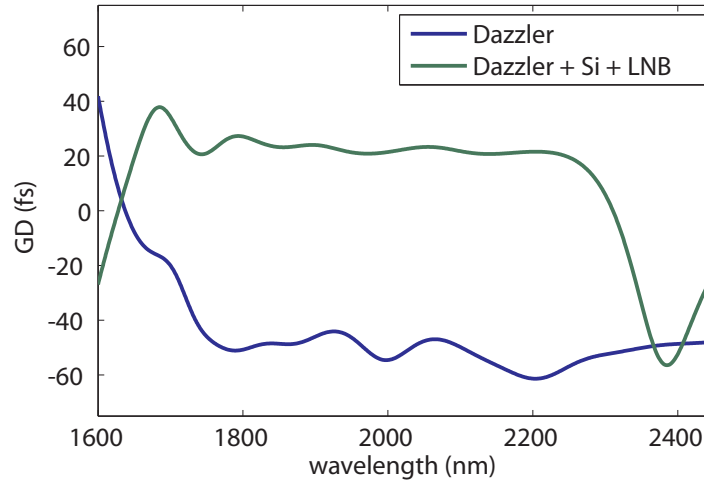


Figure 4.3: The retrieved group delay (using spectral interferometry) of the AOPDF itself and a combination of materials, later used in chapter 5, after compensation with calculated phases.

As a consequence of the well-behaved spectral phase of the seed (see section 2.4.2) and the analytically calculated material dispersion, we will see how only small corrections need to be made for good pulse compression (shown in fig. 5.8).

A general advantage of the AOPDF here is that it does not need a high resolution spectrometer, as typically encountered when large GD values are to be measured. Instead it keeps the overall dispersion in the interferometer balanced, leading to well-resolved fringes even when using broad-band low-resolution IR spectrometers, like in our case.

It should be noted that the AOPDF efficiency is severely reduced from the large TOD needed to compensate for itself. When GDD is dominating (and the AO waveform is maximized), it reaches its maximum efficiency, which is around 4%, using $GD = 6500$ fs and $GDD = 15000$ fs². At the values used for compression later, the TOD of the device itself is dominating, which limits the diffraction efficiency to about 0.25%.

4.2.3 CEP control

The AOPDF can also directly modulate the CEP, as shown in fig. 4.4. There, the CEP is first flipped (by π) between the two arms of the linear interferometer a few times. Starting at shot 300, this flipping is applied to every other pulse, which makes the interferogram (integration time 50 ms) disappear. In chapter 6 we will rely on this method, as the current for a constant CEP will vanish over few laser shots. Also this allows us to use a lock-in amplifier for CEP sensitive processes in general. Measuring the phase-stability of the AOPDF throughput directly with optimized PLL settings, a CEP jitter of 46 mrad was evaluated. This would be equivalent to an electronic jitter of 350 ps in eq. (4.1). However, since the interferometer stability itself is limited, an optical path length jitter of 15 nm would lead to the same result. Therefore, this CEP

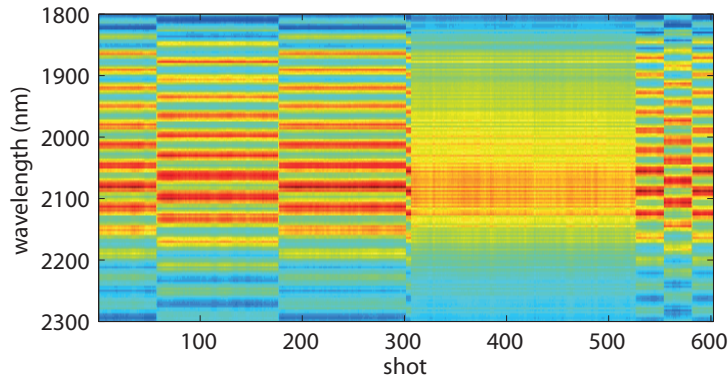


Figure 4.4: f-f interferogram of the diffracted AOPDF signal

jitter contribution of the AOPDF can only serve as an approximated upper limit.

As the transfer of the carrier envelope of the acoustic wave to the optical wave can be used to actively stabilize the CEP phase without influencing any other system parameter (like moving wedges would), it could in principle also be used for a slow-loop. Unfortunately, the AOPDF driver is limited in its memory to only two acoustic wave-forms in our configuration. However, an upgrade for single-pulse CEP control is commercially available by now. Since the acoustic wave inside the dazzler takes about $42.5 \mu\text{s}$ to travel through the crystal, the regulation bandwidth in such a loop could reach almost 25 kHz [37]. After all, for experiments that only require a constant CEP, the OPCPA of chapter 5 drifts very marginally (provided that pump and seed are actively synchronized) and therefore no slow-loop is needed.

4.3 Optical synchronization

4.3.1 Setup

Figure 4.5 shows a simplified scheme of the optical synchronization between seed pulses (amplified in a multipass Ti:Sapphire amplifier and broadened in a hollow core fiber, see chapter 2) and pump pulses (amplified in a regenerative Yb:YAG amplifier, see chapter 3). The amplification delay for both amplifiers is very different. As the thin disk has little gain, around 100 round trips of 40 ns each have to be completed. In comparison, the thick Ti:Sa crystal offers larger gain and needs only 9 passes to reach saturation, leading to a delay of few 10 ns. CPA-related elements can add to the build-up of jitter between pump and seed pulses considerably, when beam pointing perturbations inside of them [73] are present. Beam-pointing jitter in the beam delivery paths translates into temporal jitter as well (as we will see in section 4.3.6), but its contribution is very small in comparison.

However, not only fluctuations after the dichroic beam splitter (that separates pump and seed amplifier spectral components and is shown in fig. 4.5) are leading to jitter in the OPCPA system.

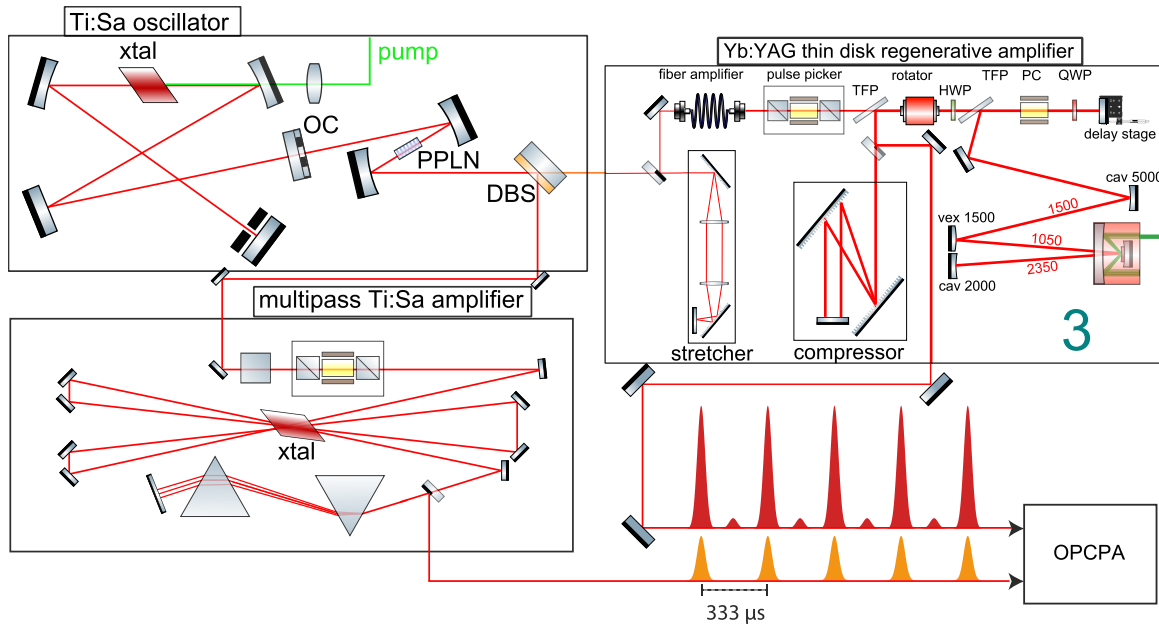


Figure 4.5: Scheme of the optical synchronization. A dichroic beam splitter (DBS) separates the seed for both amplifiers. The amplified pulses then need to be synchronized in the OPCA.

The different amplification delays mean that optical synchronization does not overlap identical oscillator pulses in general. Rather it depends on a stable mode-locked oscillator with very little (integrated) jitter, as one pulse is coupled out earlier to the longer amplification arm, whereas a later oscillator pulse is coupled out for the shorter arm. Effectively, the first pulse in our setup has oscillated in the regenerative amplifier cavity for around $4 \mu\text{s}$ instead of in the oscillator cavity. That means variations in both cavity lengths within this period lead to temporal jitter in the OPCA synchronization.

4.3.2 Limits of optical synchronization

Optical synchronization is a very simple and effective approach for OPCA with long pump pulses. For ever shorter pulses from pump lasers that developed in the last years [103, 118, 57, 74, 88] however, the jitter in temporal delay between pump and seed pulses starts to be no longer insignificant. Given the needed synchronization level of $\ll 150 \text{ fs}$ (or $\ll 50 \mu\text{m}$), this issue is quite obvious. Over more than 100 round trips, this would mean that only $< 5 \mu\text{m}$ (or $< 0.4 \text{ ppm}$) round trip length fluctuations would be tolerable (given that at these high frequencies, the cavity optics can be considered as mechanically decoupled from the breadboard) during the amplification period.

Fast jitter in an OPCA will lead to a fluctuating amplified signal and a shift of the amplified spectrum, as the stretched seed is gated by the temporal pump window. Consequently even the compressed pulse durations are affected.

Influence on the CEP

Very recently the coupling of timing jitter to CEP jitter was measured in a NIR OPCPA system [48]. The main contribution was attributed to the shift in center wavelength of the amplified OPCPA pulses. For a sinusoidal delay modulation of 90 fs (peak-to-peak, in air the induced CEP-slip can be neglected), the CEP followed with 0.8 rad, while the center wavelength only shifted by 5 nm (amplified spectrum about 700–1200 nm). The concrete experimental conditions (like the chirp of the seed pulse and the material dispersion in the OPCPA) determine the coupling. Because of the much shorter pump pulses (470 fs) this is therefore significantly higher than the estimation of our OPCPA (in section 5.5). Again, this shows how better synchronization is needed for future decreasing pump pulse durations.

In fact the shift of the center wavelength is only a reshaping of the envelope (with a chirped carrier). The analogy to section 4.2.1 is obvious, where a delay in the acoustic pulse (compared to the delay in the optical pump pulse considered here) also leads to jitter in CEP, however on a different time scale. In both cases, the envelope of the pulse is shifted with regard to the carrier, either by amplification or diffraction. As the carrier remains unchanged for a delay in the pump pulse (since the optical setup is not moving), this way the CEP is altered (as discussed in section 1.1.1). Indirectly, energy fluctuations also couple into the CEP by means of XPM, SPM (section 1.2.3) and the optical parametric phase [27]. All of these effects depend heavily on the parameters of the OPCPA system, but become more and more severe in modern ultra-broadband ps-pumped setups. Finally, it should be noted that the measurement of $f-2f$, when depending on filamentation, also couples intensity to CEP noise, as described in [4].

4.3.3 Measuring technique

For characterizing temporal delays of less than 10 ps we resort to a technique developed by Miura et al. [89]. By stretching the broadband seed pulse to a duration much longer than the compressed narrow-band pump pulse, the gating of the resulting sum frequency generation (SFG) leads to a spectrally resolved cross-correlation that allows calculating the delay between both pulses in a single shot (see Figure 4.6). This makes the method potentially more powerful than competing SFG-based techniques.

A balanced optical cross-correlation (BOC) [113] in comparison is built up as two identical sum frequency generation setups with a different delay between both pulses. Subtraction of the (spectrally integrated) photo diode signal yields an error-signal that is proportional to the delay around the zero-signal crossing. This then allows driving a feedback loop. To avoid intensity jitter cross-talk perfectly balanced SFG stages are required. Monolithic BOC designs as described in [70] relieve this issue partially, but are limited by sum frequency phase-matching requirements and still depend on carefully balanced optical setups.

Making use of the spectral resolution however, a single SFG stage yields an error-signal which is in principle independent of intensity fluctuations. Different from BOC, the spectrally derived

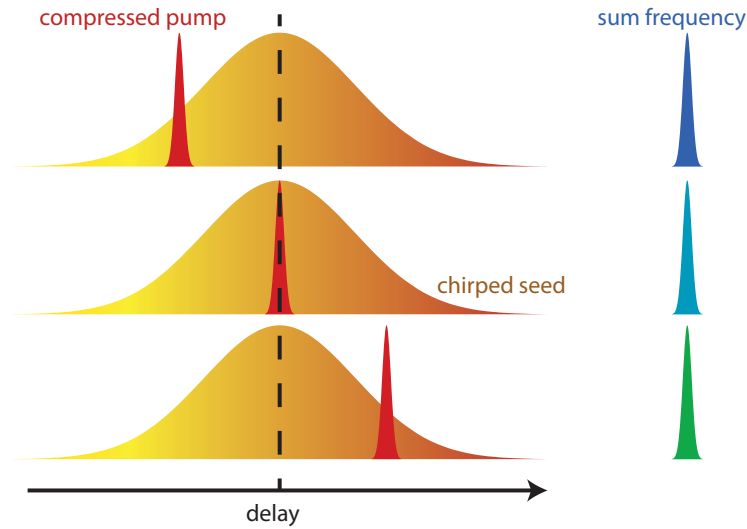


Figure 4.6: Spectrally resolved cross-correlation between a broadband chirped seed pulse and a compressed pump pulse maps the temporal delay into frequency space.

error-signal is strictly monotonic over the whole temporal overlap. This again is very beneficial for a simple regulation loop that cannot fall out of lock any more.

Moreover, the large (and well-known) dispersion of the seed pulse allows the calculation of the pump pulse duration for each shot. However, phase-matching bandwidth needs to be sufficient in order to not underestimate the pulse duration. For our pump laser, the data shown in the inset of fig. 4.7, yields a pulse duration of 1.8 ps FWHM averaged over 10000 shots.

4.3.4 Software-based feedback loop

The first realization of a feedback loop is shown in fig. 4.7. A LabView-based stabilization was developed to correct for delay drifts, so the work on the OPCPA stages was possible over an extended time. For the measurement of the sum frequency, a high resolution miniature spectrometer (HR4000, Ocean Optics) was used. The temporal delay was then calculated by the center of weight of the sum frequency signal. This error signal was centered to a defined set point around 450 nm by means of a motorized translation stage at a repetition rate of 1 to 3 Hz.

Measurement of long-term drifts

Apart from fast jitter components, also slow temporal drifts over minutes and hours start to become noticeable and need to be measured and compensated to ensure stable long-term operation. This section therefore describes the efforts in characterizing the temporal delay.

In order to measure a long-term drift, we need active feedback in order to not loose the sum

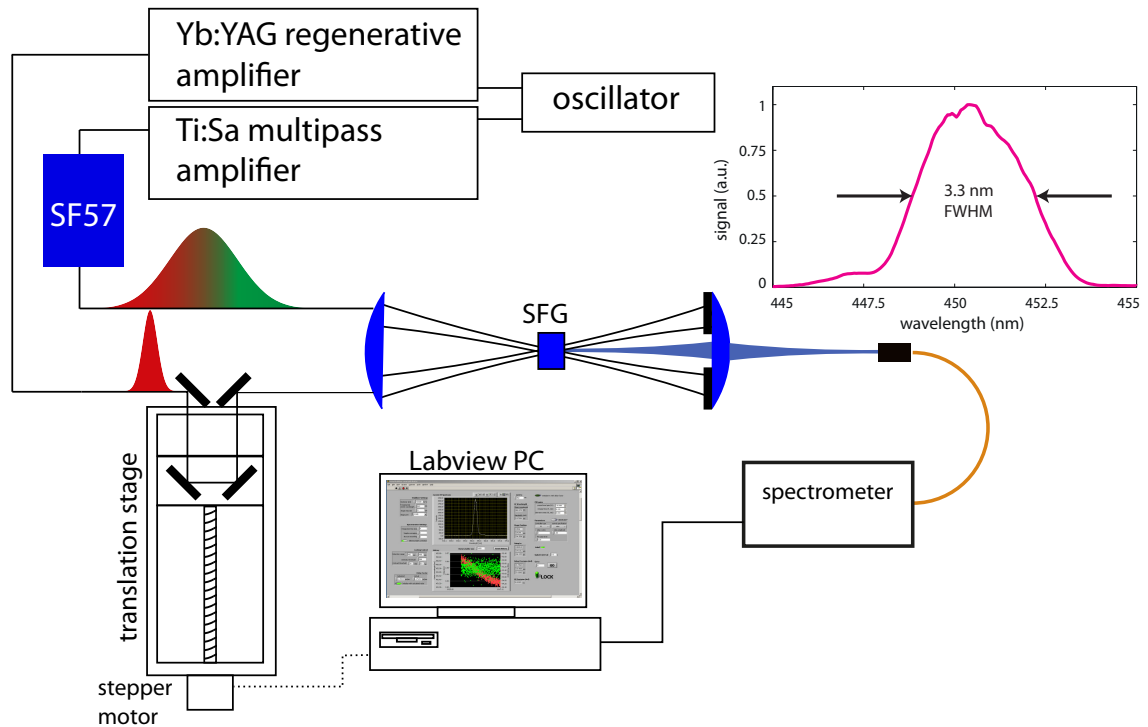


Figure 4.7: Setup of the SFG-based synchronization using a LabView PID algorithm; top right inset: The spectrally resolved cross-correlation shows a spectral width of 3.3 ± 0.1 nm (FWHM). Given a stretching ratio of $D = 550$ fs/nm this equals a pulse duration of 1.8 ps.

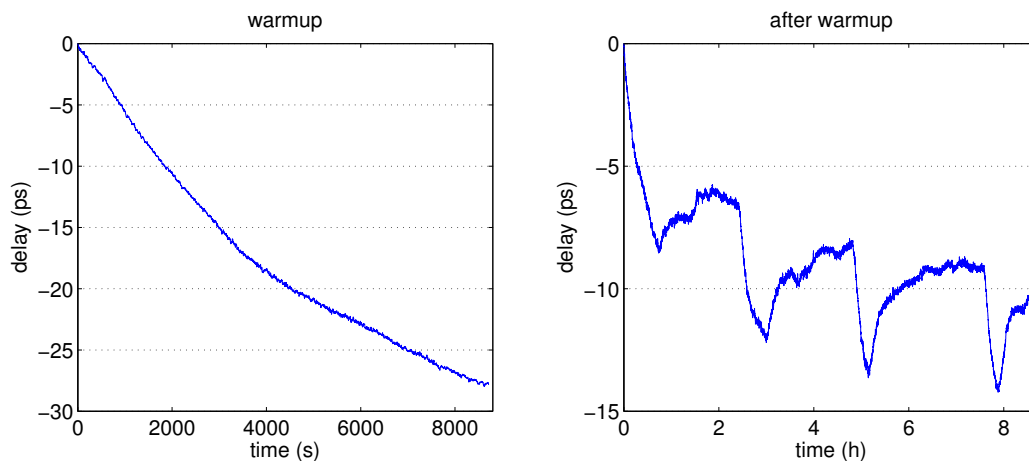


Figure 4.8: Long-term drift of optical delay in the OPCPA system. On the left, during the warm-up time a significant drift over a relatively short operation time is shown. On the right, after warm-up the delay keeps oscillating by several ps over many hours.

frequency signal. The movement of the compensating translation stage is logged (once a second) and shows the slow temporal drift that is illustrated in fig. 4.8. As the long-term drift is much larger than the fast jitter, logging the amount of feedback is appropriate for this characterization. On the left, a warm-up period of several hours is shown. Clearly, for a ultrafast pump laser, this needs to be actively compensated even for an optically synchronized system. After some warm-up time (that seemed to depend on the air conditioning of the lab environment), the delay oscillates (see the right of fig. 4.8) with an amplitude of several ps. The exact shape of these oscillations was somewhat arbitrary over time, but always showed repetitive patterns. A (probably oscillating and poorly tuned) regulated air-conditioning could explain this behavior.

The effect of an extending oscillator cavity cannot sufficiently describe the magnitude of the observed drift. An RF analyzer was used to monitor the repetition rate and therefore an increase of effective cavity length. During the about 360 round trips (the delay between seeding both lasers), the cavity length shift did not assume values that would explain more than a few fs of temporal delay. Also thermal expansion of transmitted pump laser cavity components cannot lead to a ps-scale drift. A potential source is the fiber pre-amplifier for the pump laser seed (see section 3.1.2), as it contains a very long actively pumped fiber, however this is part of a future investigation.

Limits of the software-based feedback loop

Note that during the characterization above, the center wavelength of the sum frequency signal was logged as well and for the data shown on the right part of fig. 4.8 results a stabilized value of $\lambda_{\text{center}} = 452.0$ nm and a standard deviation of 105.3 fs ($\lambda_{\text{center}} = 450.0$ nm and 118.2 fs for the left part of fig. 4.8). As the sum frequency was integrated over 10 ms however, fast jitter components are suppressed here.

As [73] reported about significant jitter arising from their pump laser stretcher and compressor setup at the time of the measurements, we rebuilt the compressor of our pump laser (see section 3.1.2) using more rigid opto-mechanics. When measuring the fast jitter components again, this time with a miniature spectrometer recording single shots (Thorlabs LC1-USB; since the HR4000 used above had a minimum integration time of 3.8 ms), we can evaluate a jitter level of 48.6 fs remaining after the stabilization. This level could be reproduced consistently after rebuilding the compressor, indicating that mechanical vibrations are probably playing a major role in the jitter we still observed. Housing the compressor in an air-tight box [72] and replacing the stretcher by a volume Bragg grating could further reduce the amount of jitter.

However, even the feedback loop could benefit from a higher bandwidth, as indicated in fig. 4.9, where a rolling average of 10 Hz is applied to the measured jitter values (sampling rate 200 Hz). Since the software-based PID loop and connected stepper motor stage only regulate at 1 to 3 Hz, the effective cut-off for slow jitter components lies below 1 Hz. The rolling average indicates oscillations on shorter time scales. As the delay is still fluctuating considerably for our short pump window, this would also cause intensity and CEP fluctuations (as described in section 4.3.2) in

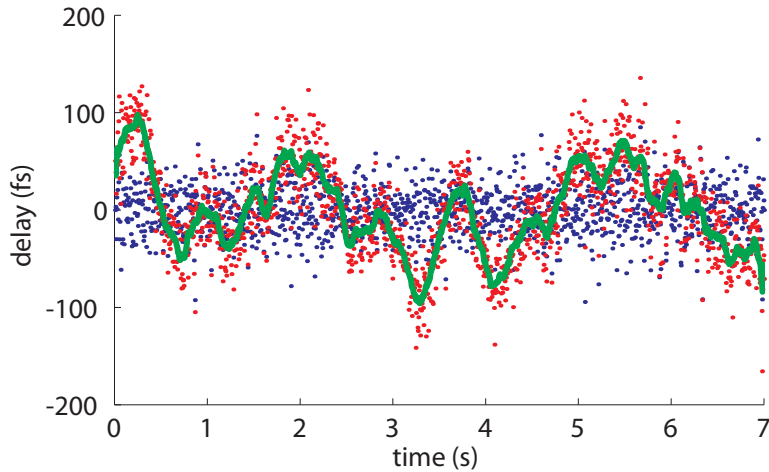


Figure 4.9: Timing jitter when compensated by the LabView PID driven stepper motor stage (red, 48.6 fs), rolling average at 10 Hz (green) and jitter limit for faster feedback (blue, 24.7 fs).

the OPCPA. Using a much faster feedback (and detection), with an effective cut-off at 10 Hz would further reduce the jitter to 24.7 fs as indicated blue in fig. 4.9. Unfortunately, here both software (interfacing with spectrometer and stepper motor controller) and hardware (large loads on the translation stage) are just too slow for this kind of feedback. Therefore the next section aims at rebuilding the setup for better performance.

4.3.5 Hardware-based feedback loop

After assessing the slow software feedback loop, for high frequency timing jitter a faster delay stabilization proved to be desirable. There we no longer use a commercial spectrometer read out in software, but need to build up a fast optical detection system that can ideally yield a single-shot directional error signal.

Since photo diodes are available with large bandwidths, intensity-based measurements like the BOC can be advantageous in case of high regulation bandwidths, achievable by acousto-optic or electro-optic modulators. However our sampling rate is limited to the repetition rate of the laser at 3 kHz. While this is still too fast for a standard CCD-array to be read out for each shot, a position sensitive detector (PSD, or lateral effect detector) can be read out continuously and offers enough bandwidth (typically $\tau_{RC} \approx 70 \mu\text{s}$, depending on the detector size and read-out electronics) for our application. As its outputs allow the fast calculation of the center of mass independent of the beam shape of the intensity on the detector, this is ideal for our application. Also the spatial resolution can be on the order of sub- μm (depending on the noise in the associated electronics and on the optical signal itself), which clearly trumps a CCD array. However, the sensitivity is somewhat lower compared to CCDs or photo diodes and the position is calculated by normalizing to the integrated intensity, making it susceptible to intensity fluctuations.

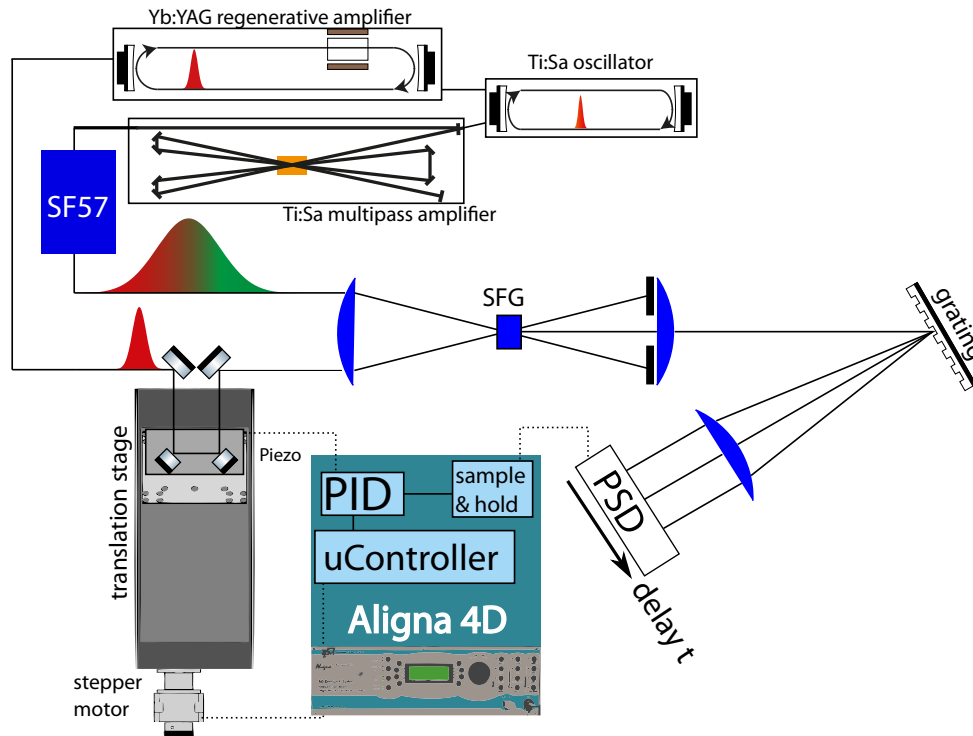


Figure 4.10: Setup of the hardware-based synchronization

As a diffraction grating can resolve our spectrally encoded delay information in space, the SFG setup only needs to be upgraded with a spectrometer-like detection setup. Imaging provides the frequency-space mapping and the strong chirp of the seed pulse achieves the time-frequency mapping, resulting in time-space mapping of temporal delay between pump and seed. The center of mass then yields this delay and provides a direct error signal.

This is realized in the lab by splitting small fractions of pump (10 mW) and seed amplifier (2 mW). Next, the seed pulses are stretched using an AR-coated block of SF57 glass. This proved to be advantageous, as a grating stretcher can easily introduce angular dispersion, if not aligned properly. Spatial chirp in the focus then showed to be problematic in the frequency resolved SF stage. As the spot sizes are rather large to avoid B-integral issues (see section 3.2.1), telescope arrangements are used for optimizing the intensity for the SFG process. Both collimated and parallel beams are then sent through a $f = 100$ mm plano-convex lens, to overlap their foci in a 1 mm long BBO crystal, cut at $\theta = 29$ deg. As the telescopes allowed close matching of the spot sizes in the crystal (approximately $90 \mu\text{m}$), the sum frequency at 450 nm output is rather high at 0.2 mW, especially given the stretched seed. While the fundamental beams are blocked, the SF is collimated and sent onto a diffraction grating (1200 lines/mm) that showed a diffraction efficiency of 45%. The angular dispersion is then translated to spatial chirp by use of another lens that focuses on the PSD (Hamamatsu S599-01). This results in a very elliptical intensity profile, where beam position along the fast axis (x_{PSD} in the following) indicates the pump-seed

delay τ according to

$$\frac{dx_{\text{PSD}}}{d\tau} = \underbrace{\frac{\partial x_{\text{PSD}}}{\partial \lambda_{\text{SF}}}}_I \underbrace{\frac{\partial \lambda_{\text{SF}}}{\partial \omega_{\text{seed}}}}_II \underbrace{\frac{d\omega_{\text{seed}}}{d\tau}}_III \quad (4.2)$$

where I is given by the imaging system of lens and grating, II by the wavelength of the pump laser and III is proportional to the chirp of the seed pulse. I and III allow tuning of the system for higher resolution or longer temporal range. Limiting however is the size (4 mm) and the signal-to-noise ratio (SNR) of the PSD, as well as the finite pump pulse duration.

While a larger stretching factor III increases the sensitivity, it limits the temporal overlap and therefore also the generated SF signal. This then decreases the SNR (and consequently the resolution) of the PSD. A similar argument for I can be made.

In the perpendicular direction y_{PSD} , the jitter from beam pointing amounted to $0.7 \mu\text{m}$, which is equivalent to 6 fs for our configuration. This is larger than the theoretical (no sample & hold noise) resolution of the PSD ($0.2 \mu\text{m}$). A similar beam pointing is also expected along x_{PSD} , leading to some cross talk with the beam stabilization in our jitter stabilization. Equation (4.2) provides the solution if this cross talk is too severe. Note that beam pointing here does not necessarily mean the focus position is moving (which could be improved using I), but the PSD could vibrate as well.

The refined setup is shown in fig. 4.10. To minimize the engineering effort, a commercial beam stabilization (Aligna 4D, TEM Messtechnik Hannover) like in section 3.2.3 was employed. Instead of four spatial dimensions, it now stabilizes one temporal (appearing as a spatial) dimension in the following manner: The PSD signals are fed to sample & hold stages (S&H), before the position is calculated. Given this error signal, a PID controller tries to center the delay by moving a fast piezo stage (nanoX 200 with 30V300 amplifier, open-loop, Piezosystems Jena, $240 \mu\text{m}$ range). A micro-controller uses a linear translation stage (LIMES 84-120-HMS, OWIS) to center the piezo voltage at about 75 V for better linearity and range. This way the piezo stage (with a resonance frequency of 500 Hz at a retro-reflector weight of 40 g) can compensate for fast jitter, while the slower stepper motor stage is ensuring long-term temporal overlap.

Measuring the jitter with this solution yielded the data shown in fig. 4.11 and fig. 4.12 in temporal and frequency domain, respectively. While the free-running jitter amounted to $\sigma = 127$ fs (shown in blue), the stepper motor stage alone could only compensate for frequency components below 1 Hz, similar to section 4.3.4, which resulted in comparable $\sigma = 45$ fs. Using the faster PID-regulated piezo stage, the effective regulation bandwidth was increased by more than one order of magnitude, as shown in fig. 4.12. This enables jitter compensation down to 24 fs, a small fraction of the pump pulse duration. The right axis of fig. 4.12 shows the integrated timing jitter, given by $\sigma = \sqrt{\sum_f P_f}$, where P_f is the power spectral density plotted on the left axis. We see that the piezo can limit the jitter below 220 Hz to around 10 fs. However, there we experience vibrations on the optical table. Devices like turbomolecular pumps work in this frequency range and increase the timing jitter significantly. It should be considered, that the significant shot-to-shot jitter of 15 fs derived from the data shown in fig. 4.11, is located beyond the Nyquist

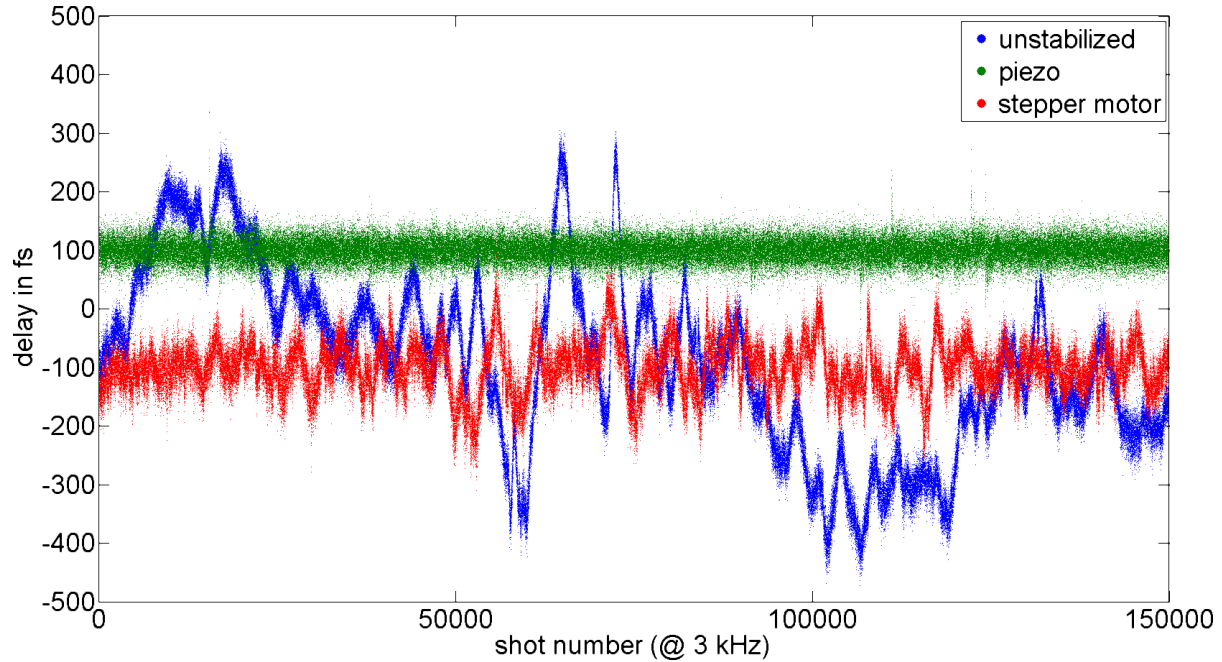


Figure 4.11: Temporal jitter as measured from the PSD error signal. Curves are offset by 100 fs for better visibility.

frequency and is mirrored onto lower frequency components (aliasing). The strong perturbation at 220 Hz could therefore be located at 2780 Hz (or further above) and be of electro-magnetic origin. In fact, in chapter 6 an elevated noise floor was observed in this frequency range. For the measurement of fig. 4.11, this was already reduced by a simple home-made low-pass filter at 10 kHz.

When tuning the PID loop more aggressively (less I and more P), the high-frequency components can even increase, since the perturbations drive the loop into oscillation or even resonance. Also the limited sturdiness (due to weight limitations) of the retro reflector mounted on the piezo stage can lead to oscillations in the regulation loop. This may even be fostered by cross-talk, since coupling of the error signal to beam pointing or intensity is to be expected to a certain extent in our detection scheme.

4.3.6 In-loop and out-of-loop performance

Different from the setup of [113], where two oscillators are synchronized and collinearly combined within the regulation loop, OPCPA (especially in the non-collinear fashion) needs detached delivery beam paths for both pump and seed. Therefore fluctuations between these two delivery arms will induce further temporal jitter. The control loop (as most beam stabilizations) only regulates to some virtual reference point (given here at the SFG stage), pulse interaction beyond this point will not be temporally stabilized (it is out-of-loop). Imaging could in principle be used

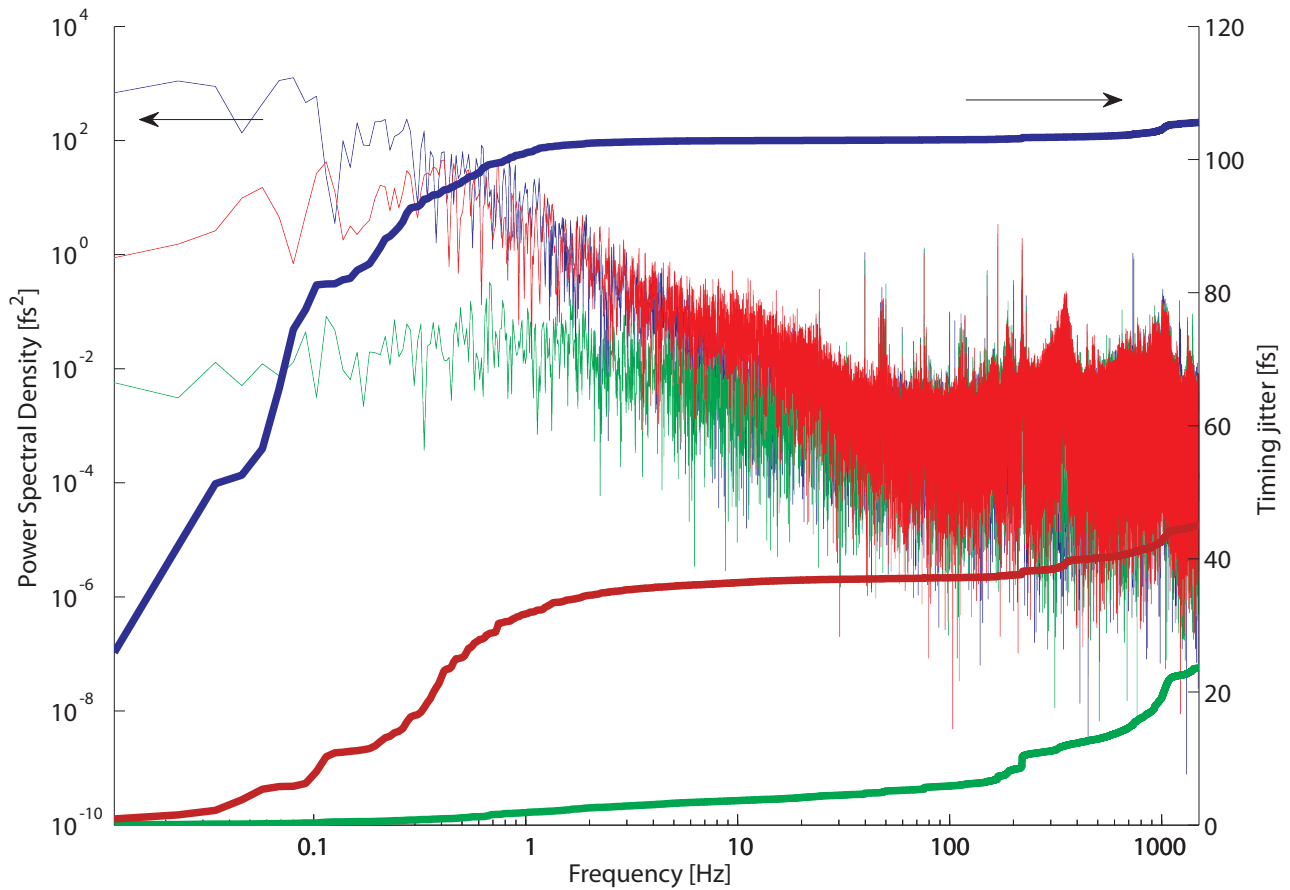


Figure 4.12: FFT of the timing jitter shown in fig. 4.11, with identical color coding. The Nyquist limit is 1500 Hz.

to compensate deviations between in-loop and out-of-loop for each OPCPA stage, however this would result in a more complicated and less versatile setup. Also instead of the sum frequency approach, spectrally resolved difference frequency generation derived directly at an OPCPA stage would place one amplification stage inside the regulation loop [48]. However, to obtain optimum conversion efficiency and high pulse energies, several stages are usually needed. These stages would therefore be out-of-loop again. As the delay synchronization should merely serve as a useful add-on to the OPCPA system, to demonstrate its usefulness, we need to characterize the out-of-loop performance.

To compare the performance of both in-loop (SFG1) and out-of-loop (SFG2) stages simultaneously, we use a bifurcated delivery fiber for our existing spectrometer. Phase-matching at SFG2 is slightly detuned to distinguish both signals (see inset in fig. 4.13). Compared to an OPA stage, this allows a much more detailed comparison of the performance, as instabilities of pump or seed energy do not influence the measurement. Also in a broadband OPA stage, the resolution for spectrometer-based jitter detection is limited and the chirp of the seed pulse is not necessarily very linear, let alone the synchronization between two individual spectrometers.

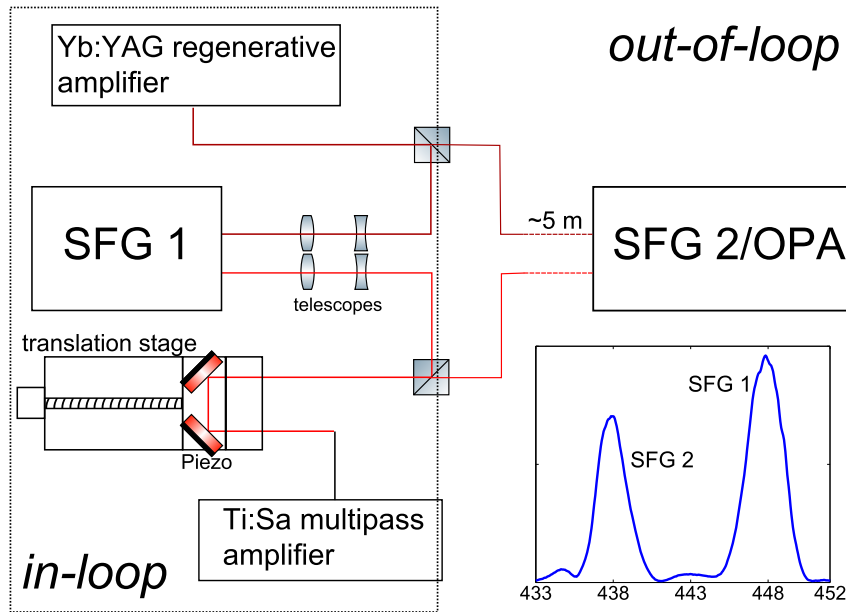


Figure 4.13: Setup using two different SFG stages, for characterizing jitter in and out of the regulation loop.

The beam delivery for SFG1 includes some telescopes for optimizing SFG efficiency, which at the same time manipulate beam pointing. The out-of-loop beam path was about 5 m, however both paths total lengths were similar. Both stages contain their own (and different) glass blocks for chirping the seed pulses. The center of mass for both SFG spectra is plotted in fig. 4.14 over 1228 s, both for the stabilized and unstabilized (SFG1 only) case.

From the inset in fig. 4.14, we can observe that the out-of-loop delay follows the in-loop delay closely. However the timing jitter did increase slightly already from 15.6 fs to 21.9 fs. Note that the jitter now was measured with a spectrometer again, so the integration time of 10 ms does average out fast jitter components, as shown in fig. 4.12, while the PSD with its single-shot measurement can fully characterize the single-shot jitter. However, this serves as a demonstration for the general improvement of temporal overlap in external frequency conversion stages that are located out-of-loop. Since we do not expect the stabilization system to introduce any high frequency timing jitter (this means conservative PID settings), the out-of-loop jitter should still remain below 30 fs.

4.3.7 Conclusions and outlook

The jitter between pump and seed, that leads to jitter in both the OPCPA intensity and CEP, was reduced in this chapter from over 100 fs, to 48.6 fs using a slow software-driven feedback loop and to 24 fs, when employing fast detection and feedback. As the shot-to-shot jitter between adjacent pulses was evaluated to be 15 fs, this is the limit of possible active stabilization. As

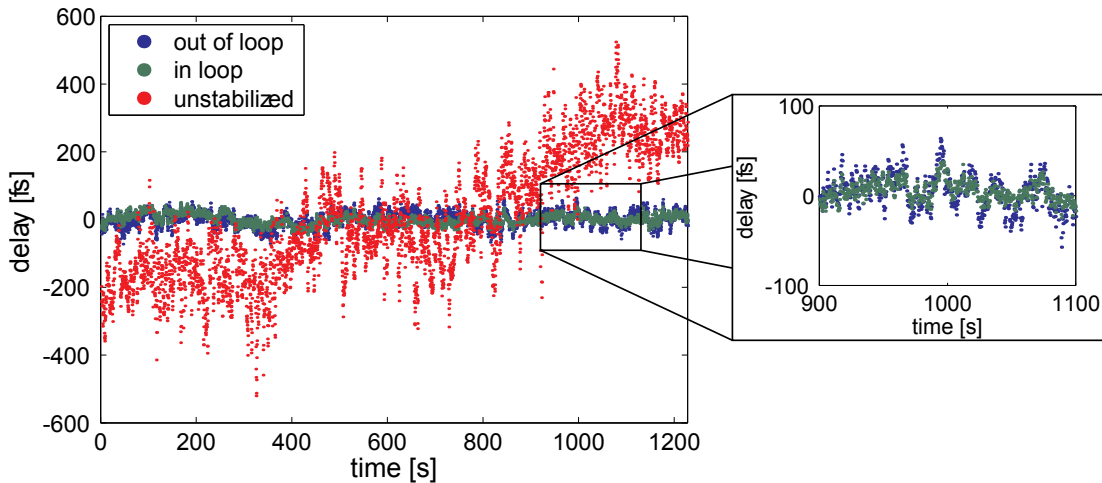


Figure 4.14: Jitter characterized in in-loop and out-of-loop SFG. Inset on the right shows greater detail.

mentioned above, further enhancement of this limit would need a detailed observation of noise and cross-talk in the feedback loop. Furthermore, as indicated in section 3.2.1, the influence of B-integral in the pump laser on intensity to timing jitter coupling needs to be investigated. The reported synchronization here was still characterized with significant temporal pulse distortions in the pump laser (visible in the cross-correlation signal). Avoiding these distortions should decrease high-frequency timing jitter in the future.

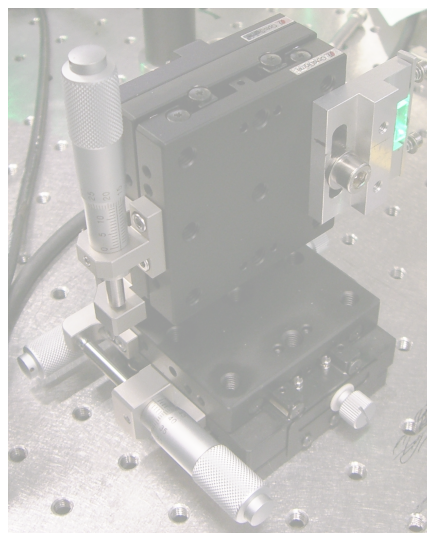
While the detection system can handle the full repetition rate of the system, the feedback was always limited by the resonance frequency (about 500 Hz) of the used piezo stage. As the optics mounted on this stage needs to possess a certain amount of sturdiness to not deteriorate the feedback loop (as seen in section 4.3.5), the load on the stage cannot be further reduced. However, when used inside the regenerative cavity of the pump laser (section 3.1.2), which offers a collimated delay-arm, the stroke of the piezo element could be reduced by the number of round trips. This would allow an even higher effective feedback bandwidth.

A more elegant approach, avoiding moving components altogether, would be shifting the delay for the OPCPA directly in the AOPDF. As it allows bandwidths only limited by the acousto-optic pulse delay inside the crystal (about 25 kHz for our model), this offers great potential for medium repetition-rate OPCPA.

While the detection is fast enough, the sensitivity may be an issue for nJ seed lasers (like un-amplified oscillators). Instead of using SFG, DFG would provide larger gains (see section 1.2.1) then and the idler of a (possibly noncollinear) OPCPA stage could be used for deriving the error signal with the same spectrometer-like PSD-based detection. In a non-collinear OPA, the angular dispersion of the idler could be amplified. As either signal or idler in a phase-stable OPCPA is not phase-locked (unless the pump itself is), this does not come at the cost of seed energy. In fact, only very recently two groups used the amplified signal/idler wave of their OPCPA to calculate

the timing jitter from the center of mass [108] or two differential diodes [48].

On higher repetition rate systems, the shot-to-shot jitter is expected to decrease (at a lower repetition rate of 10 Hz, a value of 70 fs was reported [73]). Also the S&H electronics will become obsolete, which improves the accuracy and SNR of the calculated error signal.



Chapter 5

Building an infrared few-cycle OPCPA

The earlier part of this Chapter is very loosely based on the publication [28]. However significant changes have been made since, that are covered here and in chapter 2.

5.1 Overview

The OPCPA system described in this chapter is shown in fig. 5.1. It builds on the phase-stable infrared seed generation described in chapter 2, the thin disk pump laser in chapter 3 and the synchronization of both sources in chapter 4. As OPCPA is a combination of OPA and CPA, both will be separated in the next sections (as far as this is possible in a nonlinear system). Afterwards, another section is concerned with the CEP stability of the amplified and compressed pulses.

5.2 Stretching

We start where section 2.4.2 ended; the phase-stable IR seed pulses (generated by DFG in a BBO crystal) need to be chirped in order to overlap with the temporal gain window set by the pump pulse duration. As the latter is only about 1.5 ps (see section 3.2.1), the dispersion management is simple compared to much longer pump pulses [134].

Material dispersion allows scalable stretching and compression of the pulses. However higher order dispersion becomes critical over a broad bandwidth. The situation becomes more difficult as many suitable materials have a zero dispersion point (ZDP) close to the short-wavelength edge of our desired spectrum. This means that the higher order dispersion is even dominant, see table B.2. Therefore the resulting chirp in the signal pulse would be very nonlinear, leading to non-flat amplified spectra and consequently an increase in pulse duration after compression.

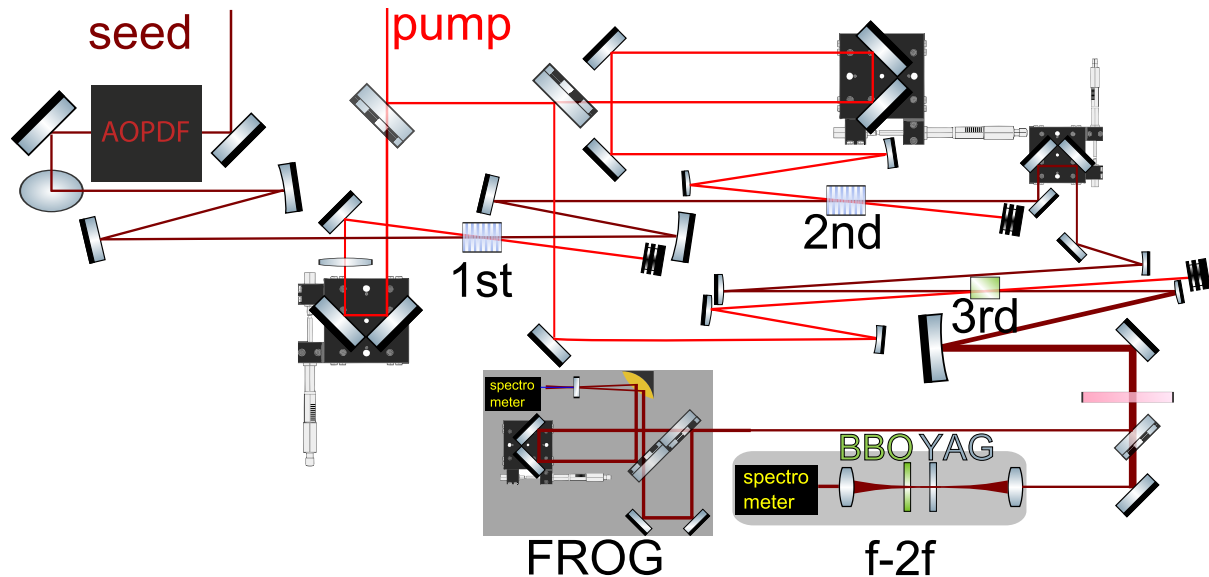


Figure 5.1: The OPCPA setup described here, together with some diagnostics used in sections 5.4 and 5.5. The indicated third amplification stage will be covered in section 7.2.

Typical infrared materials like germanium, silicon and ZnSe are suitable, since their dispersion is more flat overall. Unfortunately germanium does start to absorb below $2\ \mu\text{m}$. As the dispersion of silicon is larger and it can be grown with excellent quality, we use it in our CPA scheme. Moreover, ZnSe does offer a very similar ratio of GDD and TOD (see table B.2), making it a good replacement for silicon, while the total amount of GDD is much lower. This allowed us to use large aperture wedges to tune the dispersion coarsely. Unfortunately, ZnSe has a non-vanishing $\chi^{(2)}$, generating some second harmonic.

As the GDD of silicon and ZnSe (and all typical IR materials, see table B.2) is positive however, a negative counterpart is necessary for CPA. Since the anomalous dispersion of other materials in the infrared would again leave large contributions of higher order dispersion, they are not suitable. Chirped mirrors are routinely used to compress broadband pulses [129]. However, they (by principle) show ripples in the group delay, that lead to pedestals and satellite pulses. While these can be neglected for a few bounces, chirping to our pump pulse duration would decrease the contrast significantly. Also, chirped mirrors cannot be tuned, leading to compression issues that arise with small changes to the system. Tuning of the crystals will result in an altered optical parametric phase [110, 27], and immediately chirp the output pulses. As the intensity of both pump and signal are high in the short-pulse pumped OPCPA, despite using (some) CPA, also other nonlinear effects like XPM, SPM and SHG can modulate the phase of the amplified pulses, as we will see in section 5.4. Therefore an adaptive pulse shaper is preferred for compression down to a few cycles. The used AOPDF in our setup allows negative chirping of infrared pulses over one octave (1500 to 3000 nm) with almost wavelength-independent efficiency. It allows phase and amplitude shaping, which makes it a very useful tool (as indicated in section 4.2 already). The reason why we use it in the stretcher is the limited damage threshold and large

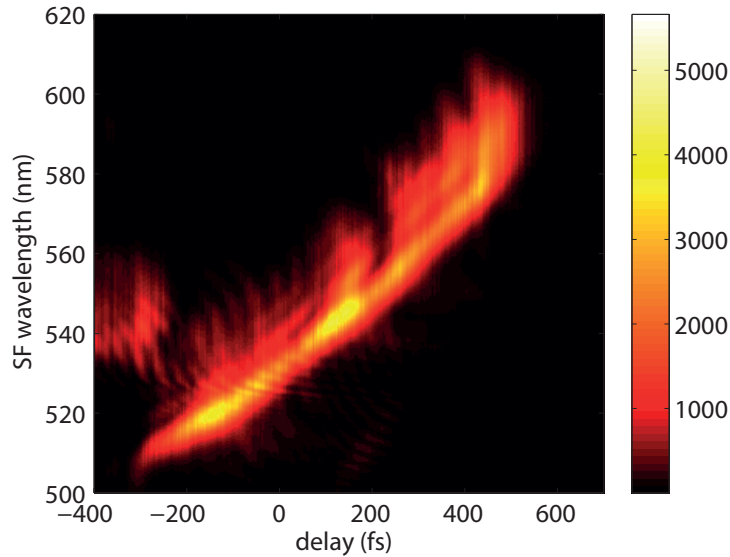


Figure 5.2: SFG XFROG spectrogram of the chirped seed pulse.

n_2 of its crystal (TeO_2). The maximum GD introduced by the AOPDF is limited to about 10 ps, which still allows it to be used as the only stretching element.

Silicon and ZnSe will therefore be used as the compression materials. Large apertures ensure that two-photon absorption (section 1.2.3) and consequently a large B-integral is avoided. The latter is especially important, since the spectral phase of the compressed pulse could be distorted.

The AOPDF throughput is very low (about 0.25%), since the TOD-dominated dispersion of the AOPDF needs to be compensated by the device itself, as mentioned in section 4.2.2. As TOD results in a spiked acoustic waveform (and the peak transducer power is limited), to avoid distortions this requires a re-normalization of the acoustic wave and consequently a lower diffraction efficiency. In order to achieve the given efficiency, additional GDD was introduced by adding 10 mm of silicon in front of the AOPDF (not shown in fig. 5.1) to fill out the 10 ps long window as much as possible. The silicon pieces used for compression are highly transmissive (when TPA can be neglected), they are further described in appendix B.3.

The stretched pulses are observed before and after amplification using the (SFG) XFROG setup described in section 2.4. This allowed us to control the linearity of the chirp and to choose the right chirping ratio for our seed pulse.

As discussed in section 1.2.4 and [91], selecting the chirp is important for a good compromise between efficiency, superfluorescence background and bandwidth. Since we were limited to a finite number of silicon thicknesses for the compressor (and those define the overall chirp), a compressor length of 1.5 mm was chosen as a good compromise for broadband amplification (compare also with section 7.2.2, where more narrowband amplification is intended, which increases the efficiency). A typical XFROG spectrogram of the chirped seed pulse for the first stage is shown in fig. 5.2. From the spectrogram we can already read a pulse duration of about

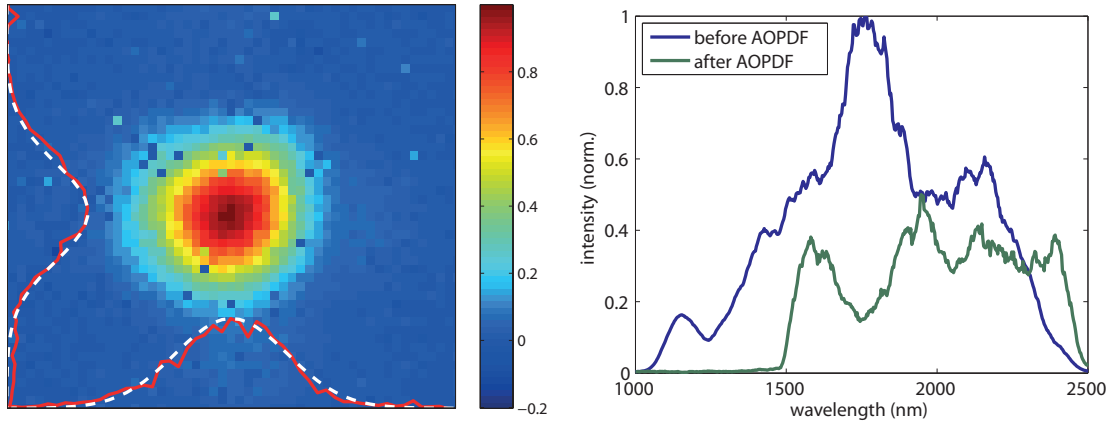


Figure 5.3: Seed beam profile after and spectrum before and after the AOPDF.

750 fs. Given that we do not know the dispersion out of the DFG BBO crystal exactly (since the individual frequency component can be generated anywhere inside), but expect it to be small, this is in good agreement with the 1.5 mm of silicon used to stretch.

Note how the individual amplification crystals also stretch the seed pulse (about 30 fs per 2 mm LNB crystal). However, since the pump window widens with lower gain [91], this works favorably for the OPCPA stages. Individual chirp optimization for each stage was not performed as it would add more complexity to the alignment and consequently limit the reproducibility in experiments.

5.3 Amplification

According to [79], the beam diffracted from the AOPDF contains spatial chirp. In order to minimize the effect for the OPCPA, the aperture of the AO crystal is filled as much as possible without clipping the beam profile (left on fig. 5.3). As the spatial chirp does not necessarily appear in a linear fashion (with respect to wavelength and lateral position), depending on the actual temporal chirp applied, even using a tilted dispersive element can only compensate for it in the first order. Therefore, instead we use an overfilled seed profile (compared to the amplified output), to avoid temporal-spatial distortions after amplification as much as possible. After being stretched, the seed pulses are thus slightly focused inside the first OPA crystal, a 1 mm long (MgO doped) PPLN (MOPO1-1.0-1, covesion Ltd.) with a period of $30.5 \mu\text{m}$, tunable in steps of $0.5 \mu\text{m}$ by selecting between five different ($1 \times 1 \text{ mm}$) gratings. This aperture is large enough for the first stage spot sizes. The profile of the seed beam focus is shown on the left of fig. 5.3 and was taken using an extended InGaAs camera (Photonic Science, $30 \mu\text{m}$ pixel pitch). The dead pixels origin from the sensor and the fit shows a spot size ($\frac{1}{\sqrt{2}}$) of about $700 \mu\text{m}$. The right of fig. 5.3 shows the spectrum generated in the DFG crystal is cut by the octave-wide transmission of the AOPDF. While the extended InGaAs spectrometer (NIRQuest 512, Ocean Optics), loses

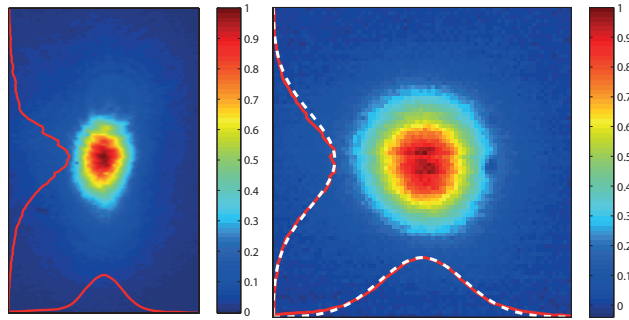


Figure 5.4: Pump and output beam profile of the first amplification stage.

sensitivity above $2.4 \mu\text{m}$, it is obvious that the seed bandwidth is large enough to not limit the target amplification bandwidth shown before on page 18 in fig. 1.3. The part that is not shown beyond $2.5 \mu\text{m}$ unfortunately cannot be optimized (as we have no means of observing it), but also these components contribute little to the final pulse duration and intensity. Furthermore, they are easily absorbed by water vapor or materials containing OH-groups like standard fused silica (as used in the experiment of chapter 6).

A (transmitted) 1.8 W fraction of the pump beam is separated from the remainder with an output coupler. After using telescopes, a translation stage for delay adjustment and a focusing lens, the pump beam profile on the first OPA crystal is shown on the left of fig. 5.4. Since the pump laser compressor does induce astigmatism (as mentioned in section 3.2.2), the profile shows some ellipticity. Its spot sizes are $560 \mu\text{m}$ and $700 \mu\text{m}$ respectively (characterized by the 4σ method), which amounts to a pump intensity of about $250 \text{ GW}/\text{cm}^2$. Moving the crystal towards the circle of confusion can optimize the amplified signal profile, as shown on the right of fig. 5.4.

The alignment of the IR seed is difficult as the diffracted light out of the AOPDF is weak and only frequency components above $1.5 \mu\text{m}$ are diffracted, where infrared viewing cards and standard IR viewers lose most of their sensitivity. Therefore we opted for distorting the acoustic modulator by applying an excessive amount of GDD. This undefined state unintentionally diffracts some visible components from the seed source (described in section 2.4.2) into the first order and allows alignment with visible light. To optimize the diffraction efficiency, a wave plate was also used to rotate the white light polarization. As soon as the beams were roughly aligned, the exInGaAs camera was used to overlap them in the focus.

This allows amplification of the sub-nJ seed pulses to about $10 \mu\text{J}$ with a very good amplified beam profile, shown on the right of fig. 5.4. It was taken with a pyroelectric camera (Pyrocam iii, Spiricon) that has a coarse pixel pitch of $100 \mu\text{m}$ and is orders of magnitudes less sensitive than the exInGaAs camera. However, its silicon window allows the camera to detect radiation in the whole MIR range. The amplified spectrum of the first stage is shown in blue on the right side of fig. 5.5. While in the short-wavelength part of the spectrum, the phase-mismatch diverges (compare to fig. 1.3), the long-wavelength part is only clipped by the spectral sensitivity of the spectrometer. Note how on a linear photon energy scale, there is little integrated energy for the red wing of the spectrum. This is due to the nonlinear GDD of silicon (see table B.2),

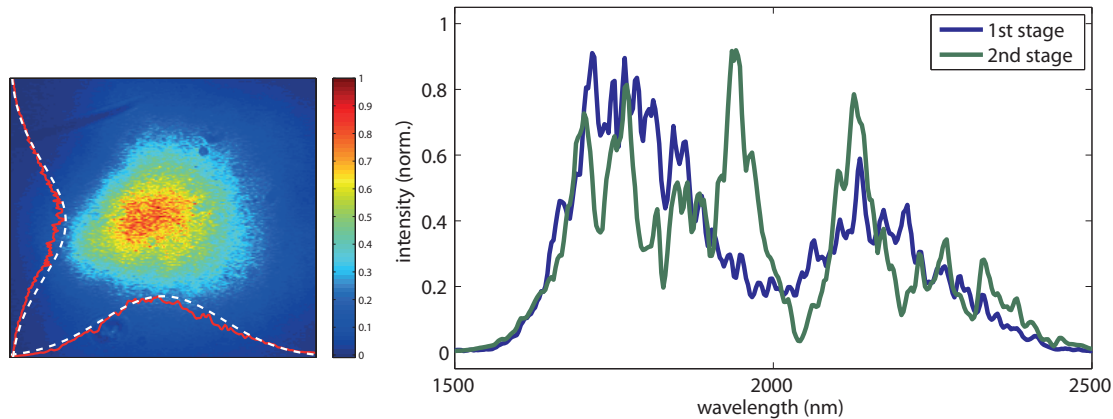


Figure 5.5: Left: Pump profile of the second amplification stage, Right: Spectra of first and second amplification stage

that necessarily needs to be pre-compensated by the AOPDF. It could rather be compensated by chirped mirrors, since most materials have a less favorable GDD to TOD ratio than silicon while being suitable in the MIR. Amplitude modulation of the seed spectrum resulted in a more flat amplification spectrum, however it showed to decrease the efficiency of the AOPDF even more, therefore it was not used.

After re-collimating the amplified output of the second stage with a concave gold mirror, its beam profile is adjusted to a spot size of about 3 mm on the second stage PPLN. The crystals (period $30.6 \mu\text{m}$) stems from a collaboration with the Taira group in Japan and offers an aperture of $5 \times 5 \text{ mm}$. This area is pumped using about 9 W of the pump light. The pump profile in the crystal plane is shown on the right of fig. 5.5. A Gaussian profile fit yields a spot size of 4.6 mm and 5 mm in both axis. This amounts only to a low pump intensity of about $22 \text{ GW}/\text{cm}^2$, however the crystal is 2 mm long and the gain of the stage only about 10 with an output power of $100 \mu\text{J}$. The reason for the poor mode-matching is the typically inhomogeneous aperture of the crystal, as reported in [63]. This is a technical limitation of the growing process for PPLNs and subject to future development. Therefore, the amplified spot size rather depended on the crystal surface than on the beam diameters of pump and seed. While pumping the whole aperture, the pump intensity and seed spot size were optimized for best output performance. The spectrum of this stage is shown on the right of fig. 5.5. The longer crystal does not limit the bandwidth in this case. However we cannot exclude that the inhomogeneity of the aperture does not also effectively chirp the period of the PPLN, yielding larger amplified bandwidths.

The phase-fronts of the amplified signal of the second stage are known to be non-trivial, since broadening of the compressed second harmonic stage in a filament resulted in complicated, but stable spatial profiles. These were directly correlated to the used spot on the crystal. Also, the mode showed very large losses when sent through the compressor and the coupling to a hollow core fiber resulted in a significant portion of the pulse energy inside the cladding, no matter what focusing was used. This will be discussed further in section 7.4.2. After the third amplification

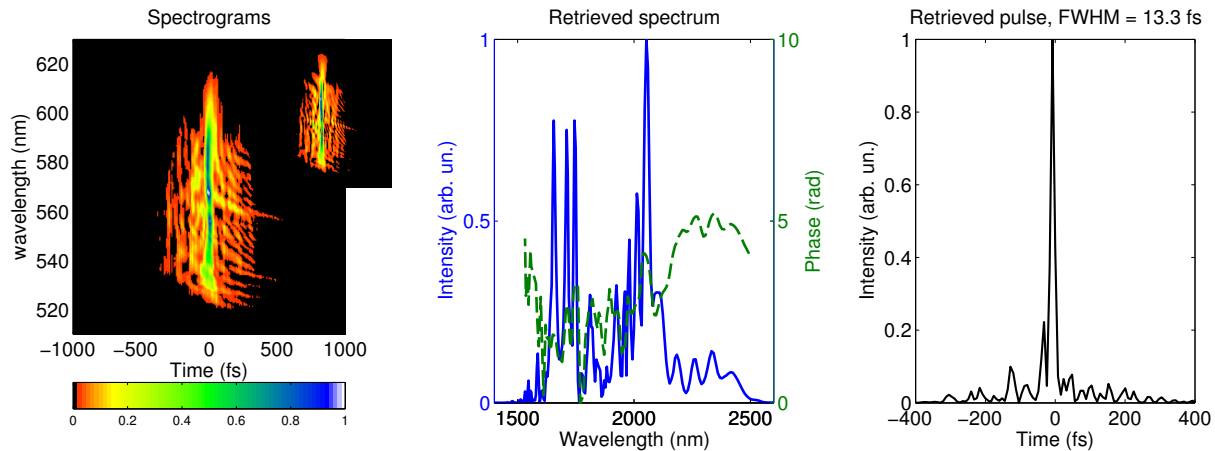


Figure 5.6: SFG XFROG spectrogram and retrieval of the compressed pulse out of the second amplification stage.

stage, the behavior improved, which leads to the suspicion that the next stage act as a spatial filter for the seed. In both the near-field (shown on the right of fig. 7.3) and far-field profiles (fig. 6.2) no irregularities could be observed. However, a more homogeneous aperture crystal is to be wished for in the future, as it would allow power scaling using the remaining ≈ 50 W of pump light.

5.4 Compression

As mentioned before, the compression of the pulses is performed with 1.5 mm bulk silicon. Using the existing XFROG setup, a retrieved spectrogram yielded the residual spectral phase. This was then feed back to the AOPDF for complete compression. Already the very first try (to the surprise of the author) compressed the pulse, as shown in the spectrograms of fig. 5.6. However, the elevated background is obvious. Later, the source was found in the insufficiently smoothed feedback files, that led to a slightly distorted acoustic wave in the AOPDF. This wave then generated a background of satellite pulses all over the diffracted spectrum. As the XFROG technique shows linear response (when based on SFG), it is well suited for detecting such issues. Better feedback (fitting polynomials to the retrieved phase, as shown in fig. 5.8) yielded a much improved background later.

Apart from the AOPDF-induced distortions, the retrieved spectrum shows good agreement with the amplified on-axis spectrum and the retrieved pulse duration is 13.3 fs, which is just below two cycles. The transform limit for the spectrum is calculated to be 12.4 fs.

Despite being close to that limit, the spectrogram shows an S-shape, because the reference pulse is not transform limited itself. Also the delay path for the XFROG was very long and therefore, a compressed pulse directly after the compressor is very hard to achieve. Because of some

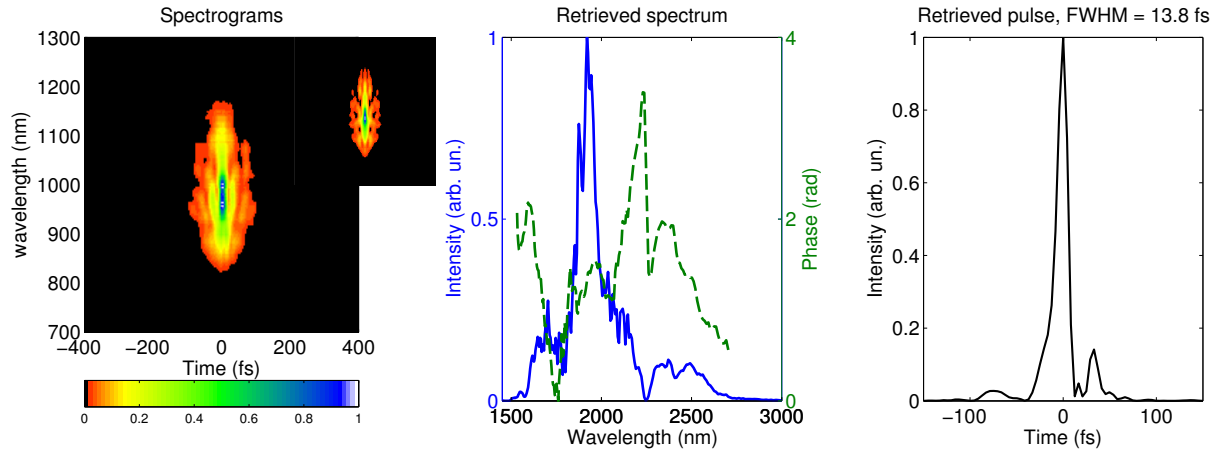


Figure 5.7: SHG FROG of the compressed OPCPA pulses.

uncertainty in the reference (through dispersion of air, etc.) also limits the ability to characterize the very shortest pulses, another (self-referenced) pulse characterization method was needed.

The transient grating method was evaluated, but given up due to the weak IR signal, that was covered by too much stronger NIR stray light on the detectors. Also no IR viewer could be used to find the diffracted signal.

Third harmonic generation (THG) on a surface proved to be hampered by the early onset of continuum generation in the material. Since this artificially shortened the pulse to be characterized in the THG FROG the signal was very limited and only a small fraction of the pulse energy could be used, resulting in very long scan times. Also a third harmonic process is less suited for pulses with bad contrast (or weak spectral wings), as its SNR and dynamic range are low (using standard linear detectors).

To prevent the onset of continuum generation, extremely thin samples of SiO_2 were used that showed surprisingly strong second harmonic generation. Also the supported bandwidth seemed sufficient. Therefore, a second harmonic FROG was used as pulse characterization method.

It needs to be mentioned that the second harmonic leads to a problem with detectors, as the frequency-doubled spectrum overlaps only partly with the working bandwidth of InGaAs and silicon detectors respectively. Therefore ideally, both detectors are needed. However, with the limited output intensity of our process, we needed to couple inside a spectrometer slit (or at least its delivery fiber). No method was found to calibrate two spectrometers coupled to one (bifurcated) fiber in a reliable fashion. While the solution of this problem (eventually maybe using piezo-driven fiber switches) is work in progress, for now an InGaAs spectrometer ranging from 800-1700 nm was used, which did cut the blue part of our spectrum slightly and did not allow it to be fully compressed. This results in slightly longer pulses for now.

In the SH FROG the effect of delay smear [138] was minimized by using as large as possible spot sizes with a significant separation on the focusing parabola. The result of the SH FROG is shown

in fig. 5.7. The retrieved spectrum is less modulated than in fig. 5.6, which can be attributed to the corrected AOPDF feedback, preserving the good contrast of the seed pulse. The retrieved pulse duration is 13.8 fs and 83% of the energy is contained in the main pulse. Since the setup is much smaller than the XFROG equivalent, we can provide a short pulse for the experiment of chapter 6. However, with a part of the spectrum cut, the retrieval of this unphysical pulse is not excellent any more. Still, it indicates a pulse duration below two optical cycles.

Most interesting is the dip in the spectrum, here at longer wavelengths compared to fig. 5.5, owing to slightly different second harmonic phase-matching. The reconstructed phase shows a discontinuity at the same position, both can be explained by a cascaded second-order effect.

The generated signal and idler are degenerate in the OPA, so both signal and idler frequency $\omega_{idler} = \omega_{signal} = \omega$ and the respective polarizations are equal. This results in $\omega_{pump} = 2\omega$, and since we use QPM in the two stages described in section 5.3, the polarization of the pump is also equal. So not only the process of OPA ($2\omega - \omega = \omega$) is phase-matched, but also SHG ($\omega + \omega = 2\omega$), following eq. (1.19). As both effects can occur at the same time, they are cascaded. The SH of the signal (or SH of the idler, or SFG between both) has the same photon energy and polarization as the pump. These back-converted photons then pump the OPA process, so signal and idler are regenerated. As the combined processes mimic degenerate four-wave mixing (it may be called SPM or XPM here, but is really degenerate) ($\omega = \omega + \omega - \omega$), this leads to a phase modulation according to eq. (1.29), in the frequency domain¹. This effect (also called self-diffraction in the literature [26]) is in fact a limitation for short pump pulses using QPM at degeneracy. A simulation by Nicholas Karpowicz in appendix D illustrates the process.

With more chirped signal and idler pulses (longer pump pulses), this behavior was not observed before in a similar setup using identical phase-matching [46]. Also the small phase-mismatch using short crystals in a collinear geometry is to blame, that will always lead to some second harmonic inside the amplified spectrum. In fact, by using different PPLN gratings (periods), we could observe a shift of the dip in the spectrum on the right of fig. 5.5.

In a non-collinear geometry (NOPA), idler and signal travel in different directions, so a spatial walk-off is given. Additionally, both can be adjusted to not phase-match SHG (as discussed in [15]). However, for amplified spectra close to one octave SFG between idler and signal can still lead to unwanted interference inside the amplified spectrum, even taking these precautions [111]. Also the bandwidth and gain of QPM is unrivaled by angle phase-matching for our wavelength regime (see section 1.2.2), so longer pump pulses in fact seem like the only option to suppress these phase modulations. As an intermediate measure, a strong depletion of the pump was avoided, to limit the effective crystal length for parasitic second order processes.

Note how (spectral and CE) phase modulation can also be caused by elevated SPM (because of nearby TPA) in the silicon compressor. Using telescopes before and after the compressor to expand the beam, this was avoided as much as possible.

The modulated phase of the spectrum does limit the compressibility, since the transform limit

¹As the effect appears on a chirped pulse, it may also be considered in time domain.

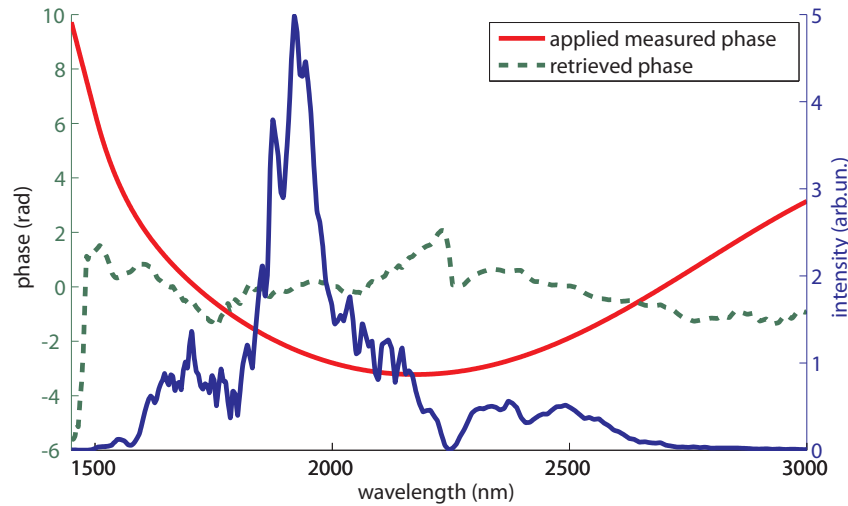


Figure 5.8: The (retrieved) additional phase applied to the AOPDF in order to compress, after analytically compensating for the large bulk dispersion.

of the reconstructed spectrum is 11.7 fs. This is shorter than from the XFROG measurement, because more red components are retrieved, which cannot be measured by the exInGaAs spectrometer used for fig. 5.5 and do also not appear in the measurement of fig. 5.6. However, since we cannot check this spectral range on a daily basis, there may just not be any amplification from day to day. Also these components are weak and do not significantly shorten the pulse.

Note that the compressed pulse shown in fig. 5.7 does not possess a completely flat phase, as the AOPDF only allows one to modulate the phase before amplification. Nonlinear effects (like those mentioned above) can then modulate this phase and lead to a longer pulse. Also repeated feedback did not shorten the pulses any more. As no suitable high-energy adaptive compression method with high efficiency is known to the author, these nonlinear effects rather have to be suppressed to achieve even better compression.

The phase that was applied to compress the pulse was in fact very slight. Analytically calculated phases did already compress the pulse to a large extent, while a single FROG retrieval (and fitting of the retrieved spectral phase using low-order polynomials, shown red in fig. 5.8) shortened it to the above mentioned pulse durations.

As a side-note, efficient compression of the pulses could be observed by eye when using small (unexpanded) beam diameters on the silicon compressor. While being opaque up to 1050 nm (see appendix B.3), the bulk silicon did emit visible (broadband) red light, that could be identified as the third harmonic (TH). Since the absorption coefficient of silicon at 700 nm and room temperature is $\alpha = 1890 \text{ cm}^{-1}$ [43], the TH must be generated in the last $\approx 5 \mu\text{m}$ of the back surface. The dispersion of this thickness leads to less than 3 fs of pulse broadening, so a strong red light did indicate a well-compressed pulse. Also propagation in air lead to build-up of TH for small beams. Unless helpful in alignment of optical setups (like the SH FROG used in this section), the beam was usually expanded to avoid this behavior in chapter 6 and chapter 7. The

tendency toward THG in air and other isotropic media will be investigated more in chapter 7.

5.5 CEP characterization

The CEP was characterized using a collinear f - $2f$ setup, since interferometers using two arms were observed to drift too much over extended measuring periods. The pulses were first broadened by focusing into a (2 mm thick, uncoated) YAG crystal and then doubled using a (1 mm thick, uncoated) BBO crystal. The fringe contrast was optimized by a cube polarizer, since it provides an indication of fast CEP jitter (see section 4.2.1). The modulation depth shown in the bottom graph of fig. 5.9 is quite good given the integration time of 100 ms. This is especially important to exclude large hidden high-frequency CEP jitter. The dead time of the spectrometer is about 2%, so the interferograms are recorded at a rate of almost 10 Hz. Analyzing the green fringes, we evaluate a CEP jitter of 155 mrad, shown in the middle of fig. 5.9. It is obvious that almost no drift occurs in the measured period of 2895 s. In fact the fitted CEP drift is only 100 mrad/h , and for most experiments a slow loop is therefore not necessary. However, using a rolling average filter, we estimate that a slow loop with a bandwidth of 0.5 Hz, would reduce the CEP jitter to 91 mrad. The shot-to-shot jitter accounts for 51 mrad. This could be reached by controlling the CEP directly using an upgraded version of the AOPDF.

Disabling the delay stabilization of section 4.3.5, the CEP stability decreased considerably. The interferogram in fig. 5.10 is fluctuating and the retrieved CEP jitter is 402 mrad. This allows us to calculate the timing jitter to CEP jitter coupling (discussed in section 4.3.2). Assuming an unstabilized jitter of 127 fs (from section 4.3.5), together with all remaining sources of fast CEP fluctuations that amount to the 51 mrad shot-to-shot jitter mentioned above, this would lead to a coupling constant of $\frac{320 \text{ mrad}}{100 \text{ fs}}$. It compares well with [48], if the different seed chirp is considered.

Again, using a 0.5 Hz slow loop, the CEP fluctuations could be decreased to 106 mrad. Also the shot-to-shot jitter is increased to 59 mrad, confirming the high regulation bandwidth of the delay stabilizer described in section 4.3.5. Over longer periods, the overlap between seed and pump pulses was even lost slowly.

As discussed in [4], the filament used for broadening couples intensity and CEP jitter in the typical f - $2f$ interferometer. To avoid this, for the spectrum given, a $3f$ - $2f$ interferometer would be necessary, that overlaps the third harmonic of $2.4 \mu\text{m}$ and the second harmonic of $1.6 \mu\text{m}$ without any filament. Doing both measurements synchronized (maybe even using the very same spectrometer, as in section 4.3.6), together with a simple photo diode measurement of the intensity would yield the coupling constant between intensity and CEP. At the time of the measurement, this equipment was not available to us, but should be considered in the future.

In comparison to other (actively and passively) CEP stabilized OPCPAs, our system (without slow-loop) is very comparable. While we experience more jitter than [55] (78.5 mrad), which has the advantage of being very compact and pumped by a fiber laser (as beam-pointing couples to CEP as well, see [4]), the cited system also suffers from considerable CEP drift. This may

be explained by the idler being generated in a high average power stage. Another system [90] centered at $2.2\ \mu\text{m}$ and using DFG in a PPLN, following power amplification in PPLN/PPLT reports 150 mrad over 10 s. And an OPCPA system around $2.1\ \mu\text{m}$ [125] employing BiB_3O_6 pumped with Ti:Sa pulses showed 260 mrad over 35 s and 410 mrad over 10 min, illustrating how important long-term assessment of the CEP stability is.

After the publication [119] of a part of chapter 4, a NIR OPCPA system [48] (pumped by fiber lasers again) reported explicit timing stabilization in their first OPCPA stage as a means of reducing the CEP jitter from 100 mrad to 86 mrad over a period of 40 min.

While actively stabilized amplifier systems also report CEP jitter on the level of 100–200 mrad, they do exhibit faster oscillations from the fast loop usually hidden by the integrating f - $2f$ measurement, but can be correctly characterized with a single-shot method like in [77]. Since passive stabilization removes this source of fast jitter, spectral interference methods that integrate over several shots are more appropriate here for characterizing the CEP stability.

In summary, the delay stabilization of chapter 4 stabilizes the CEP of the OPCPA to a large extent. While the good CEP stability could still be improved to excellent performance (especially given the large dimensions of the setup), the drift is little enough to omit another feedback loop altogether for the following experiment of chapter 6.

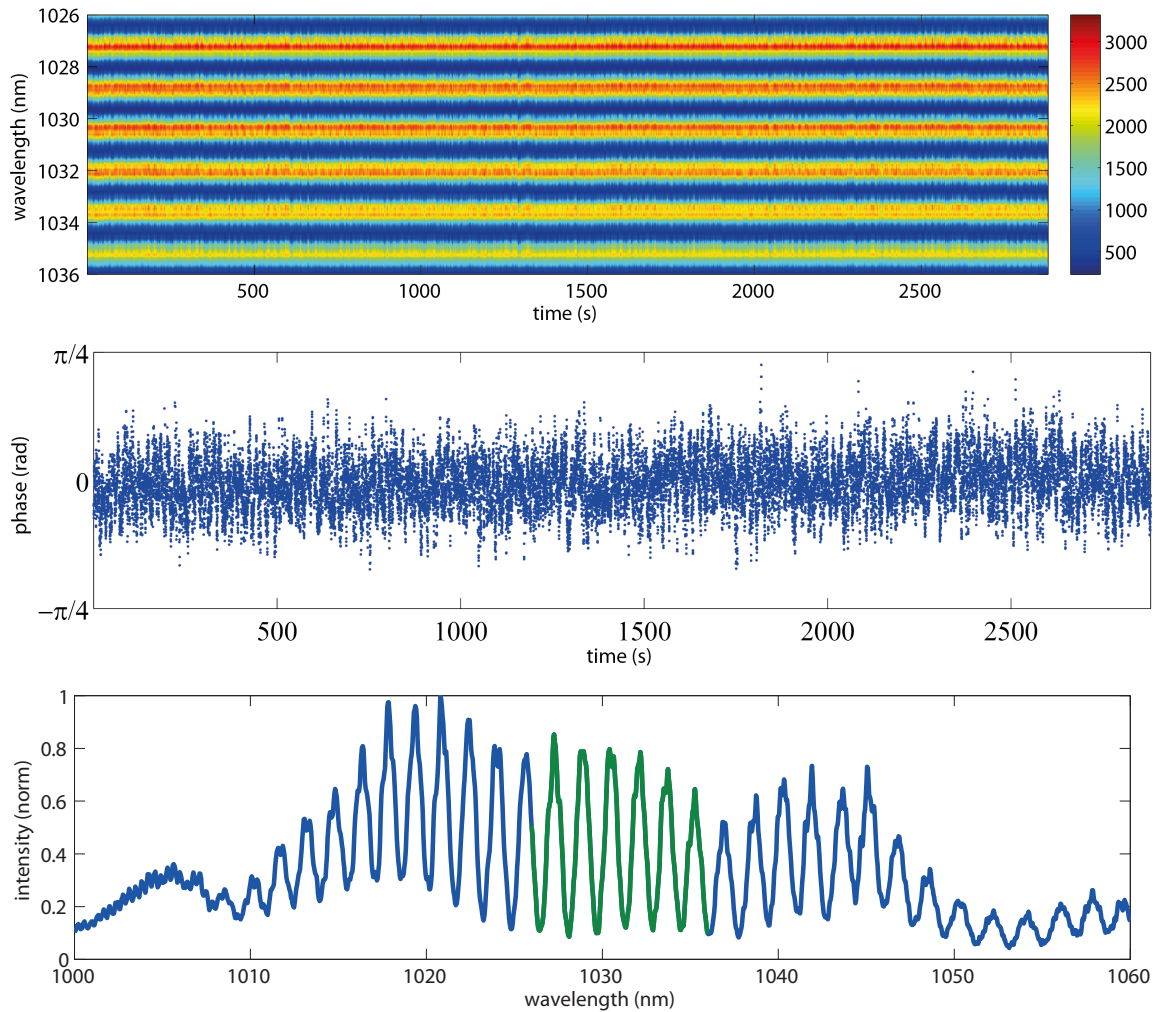


Figure 5.9: $f-2f$ measurement of CEP stability with OPCPA delay stabilization enabled, from top to bottom: $f-2f$ interferogram, retrieved CEP and interferometer spectrum (with analyzed part in green)

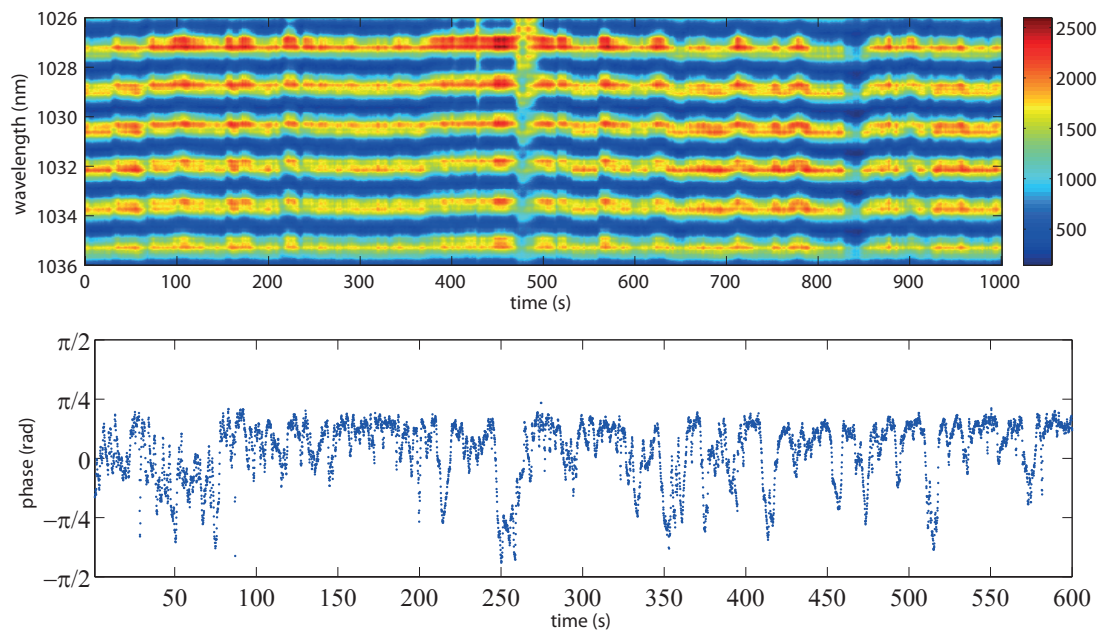
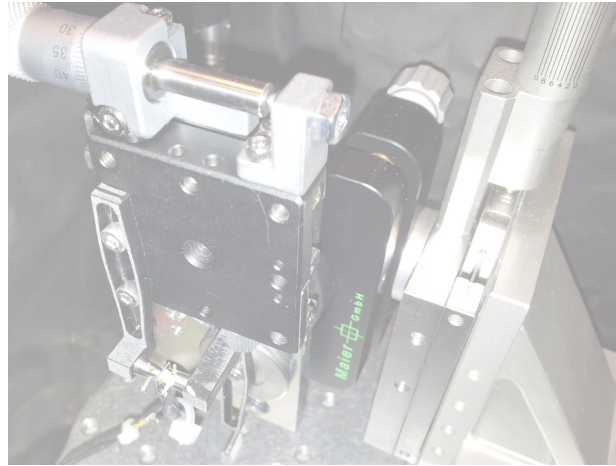


Figure 5.10: Degradation of CEP stability with OPCPA delay stabilization disabled, from top to bottom: $f-2f$ interferogram and retrieved CEP



Chapter 6

First prototype experiment: controlling currents in a dielectric using IR few-cycle pulses

This chapter will add laser field control of current in dielectric media as an example experiment to prove that the OPCPA can be used for the experiments it was built for according to the introduction.

Currents induced by optical fields in dielectrics [114] were discovered very recently in our group and the almost instantaneous carrier injection (within ≈ 1 fs) promises applications in high-speed metrology, like a simple light-phase detector [98] or a petahertz oscilloscope [71]. The latter could serve in super-octave synthesis for measurement and control of a sub-cycle NIR pulse, seeded from the source described in chapter 7. The present chapter simply aims to reproduce the first measurement of *Schiffirin et al.* [114], previously performed with a sub-4 fs actively stabilized and HCF-broadened Ti:Sapphire amplifier. The OPCPA of chapter 5 is suited for this experiment since it amplifies phase-stable infrared pulses with a duration below 2 cycles and reaches similar intensities in the dielectric. Also we are able to switch the CEP by use of our AOPDF, which allows lock-in amplification of the pA currents, that would otherwise be hidden in the noise background.

6.1 Current control theory

In order to explain the injection of carriers into the dielectric qualitatively, there are two very recent approaches both from the original publication (*Schiffirin et al.* [114]) and a theoretical investigation of *Kruchinin et al.* [80]. The latter approach is based on perturbation theory and includes the interference of multiple quantum channels (by multi-photon ionization) that lead to an asymmetry of the electron wave-packet in the conduction band in k-space, which means a

non-vanishing electron velocity $\hbar\vec{k}$. While it fits well to the previously published data of [114] for low fields, for high fields the approximations did break down. This is where the theory of [114] steps in, using a quasi-static electric field on the modified band structures (that show attosecond response time). These energy structures do correspond to Wannier-stark localization and explain the increased polarizability at highest fields by a combination of Zener tunneling and the process of adiabatic transfer. For IR fields and consequently smaller Keldysh parameters $\gamma = \sqrt{\frac{I_p}{2U_p}}$ (with the ponderomotive potential U_p given in eq. (1)), naturally the probability of multi-photon ionization decreases, while the probability of tunneling increases (as the field oscillation period is extended). Therefore the theory given in [114] (which is appropriate for very large fields over 1 V/\AA), is considered more relevant here.

In order to measure a charge after an optical pulse, the injection process needs to be a nonlinear one (that means, it must happen at some instant during the pulse), since in a linear transport over the whole pulse there would be no net charges transported. Similar to the situation in attosecond streaking [69], the vector potential in the coulomb gauge $A_L(t) = \int_t^\infty F(t')dt'$ would just average out to zero for $t \rightarrow -\infty$, leading to no acquired momentum $\Delta p = eA_L(t)$ of the electrons.

When a field F is applied to a periodic crystal, this lifts the translation invariance inside the bulk dielectric, leading to wave functions that localize at different crystal sites l , where N is the number of lattice periods and $l = -\frac{N}{2}, \dots, \frac{N}{2}$. The energies of the bands of these so-called Wannier-stark states (WS), are equally spaced in energy on the so-called Wannier-stark ladder. Now for both valence and conduction band such a WS ladder does exist, with energy states

$$E_{nl} = E_n - |eF|al \quad (6.1)$$

where a is the lattice constant and $z = la$ the coordinate of such an electron wave-packet. With increasing field strengths, the energy states of valence ($n = v$) and conduction ($n = c$) band will eventually cross. For small fields the WS wave-functions do not overlap in space, as they are from very different crystal sites in

$$\frac{E_c - E_v}{|eF|a} = |l_c - l_v| \quad (6.2)$$

As the fields are low, the crossing therefore must occur at large distances $\Delta z = \Delta la$, leading to a very small dipole coupling. Consequently, this also means at larger fields the distances are close and the wave-functions do overlap more. This leads to a anti-crossing splitting $\Delta = \hbar\gamma$

$$\Delta = \frac{|eF|a}{2\pi} \exp\left(-\frac{ma\Delta_g^2}{4\hbar^2 |eF|}\right) \quad (6.3)$$

with the bandgap Δ_g between the bands. This splitting and therefore the tunneling rate γ is exponentially small for low fields and the level crossing is diabatic (with little inter-band population transfer).

For increasing fields, the splitting Δ increases, but the transition rates are still low as the wave-functions barely overlap. For yet larger fields, the rate can become significant and the level

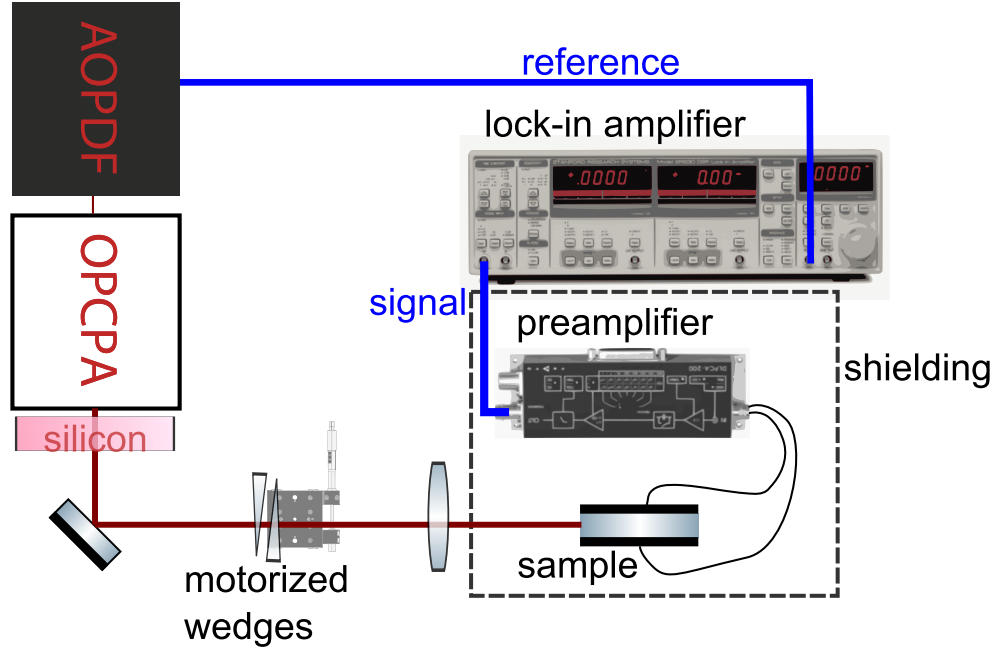


Figure 6.1: The setup used for the described current control experiment.

crossing becomes more adiabatic. This can empty a valence band state and lead to intra-band resonance. The field when this rate becomes significant is given as

$$F_{crit} = \frac{\Delta_g}{|e|a} \approx 1 \text{ V/\AA} \quad (6.4)$$

when valence and the conduction band WS states have the same slope (with respect to the field change) after the anti-crossing, as given by eq. (6.1) and eq. (6.2). For a high field $F > F_{crit}$ that means their wave-functions overlap much more (they are localized closer together). The inter-band transition can be very strong therefore, as the empty high valence band WS state can now be populated from lower states in one-photon processes.

This increase in optical polarizability rectifies the current during the pulse in a nonlinear way, which means that the net current is not averaged to zero after the pulse. We therefore only expect a measurable current for fields above F_{crit} .

The transfer of the charge in the dielectric is still not fully understood both experimentally and theoretically and subject of ongoing investigations, therefore it is not discussed here.

6.2 Experimental setup

Figure 6.1 shows the experimental setup. The driving laser pulse in current control only needs to be phase-locked in principle. However, the currents are still very small (on the order of few

pA) and electronic noise is often synchronized (or even generated) with the laser, so lock-in amplifiers are needed to detect them at a reference modulation frequency.

Using the AOPDF we can modulate the CEP by π for every single pulse using its two integrated memory slots (as demonstrated in section 4.2.3). It also outputs the reference signal to the lock-in amplifier (SR830, Stanford Research Instruments) at half the repetition rate. Since the built-in preamplifier from the SR830 produced too much noise (and long cables would couple in more current noise), a high-gain (10^8 V/A for all our measurements) trans-impedance amplifier is used (DLPCA-200 from Femto, Berlin). Also the electrode (non-coaxial) cabling is kept to a minimum. The whole setup is housed by a metallic shielding (made from aluminum foil) to reduce the environmental radiation background.

The compressed pulses of the second stage (characterized in section 5.4) are transmitted through a pair of thin wedges, which have a thickness comparable to the fused silica beam splitters of the SHG FROG setup used. Therefore they are pre-compensated in the compression. Focusing is done simply by a 100 mm CaF₂ lens, as this material has little dispersion (see table B.2) and no BaF₂ lens was available. The spot size in the NIR is hard to measure with the exInGaAs camera used in chapter 5, since the pixel pitch is 30 μ m. However, comparing larger spot sizes with both silicon and InGaAs detectors, we found that TPA on a silicon CCD [23] can yield the fundamental beam diameter with good precision. This is not trivial, since the collimated compressed beam generates (visible) TH all over its beam path. Even the last few μ m of the silicon plates used to compress emit red light, as mentioned in section 5.4. Therefore we attenuate the beam as early as possible for measuring the beam profile in the focus of the lens. The spot size was then calculated from the silicon CCD image as 60 μ m. As the beam covered only a few pixels, the larger focus spot size of a $f = 750$ mm lens is shown in fig. 6.2. Assuming some aberrations, the spot sizes are consistent and no indication of THG is observed in the fitted profiles.

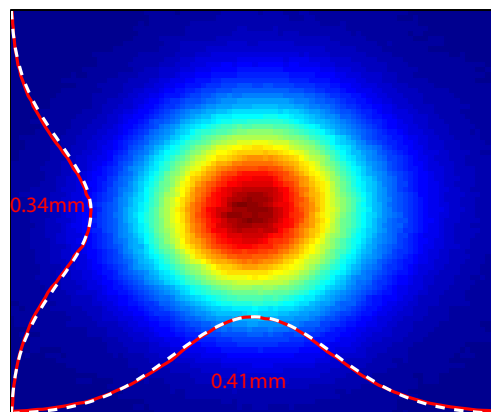


Figure 6.2: Second OPCPA stage output in the focus of a 750 mm lens, measured using TPA on a silicon CCD.

The sample is different from [114] and [98]. As discovered later [97], a more simple sandwich geometry with a (cleaved) dielectric between two coated silver electrodes reduces the photo-electric noise and allows for comparable induced net currents. The dielectric thickness (in our

case $250\ \mu\text{m}$) is large enough not to hit the electrodes with the focus of the OPCPA. For a first trial experiment, fused silica was used for better comparison with data acquired in the visible during the investigations leading to [114] and [98]. The fused silica substrate used was not IR grade (as it was not available from the supplier used before and rather kept constant for reproducibility). However the wedges before the focus are also made out of non-IR grade fused silica as well to absorb any IR components over $2.6\ \mu\text{m}$ that could lead to linear absorption (and damage) at the high focus intensities. In future experiments, that are designed for the IR OPCPA, other dielectrics will be investigated (as discussed in section 6.4).

6.3 Experiment

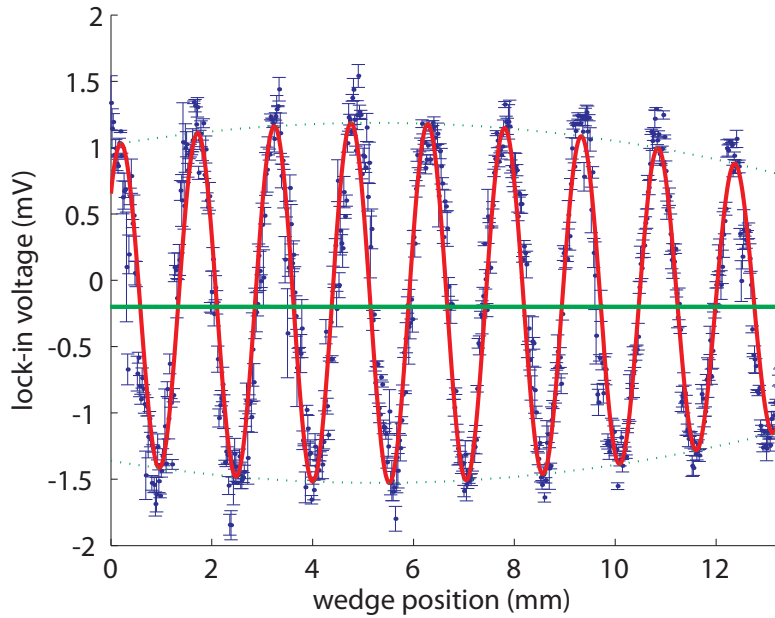


Figure 6.3: Light-induced current (after trans-impedance amplification) measured while shifting CEP and dispersion by performing a wedge scan.

With the characterized focus spot size ($60\ \mu\text{m}$) and the applied output power (between 60 and 210 mW), the intensity assuming 14 fs pulses at a repetition rate of 3 kHz equates to a peak of $350\ \text{TW}/\text{cm}^2$ ($\approx 4.3\ \text{V}/\text{\AA}$). It should be mentioned however, that due to spatial parts of the OPCPA output that cannot be focused properly (as indicated in section 7.4.2), the effective field strength could be considerable lower. In the future this could be corrected for by using a hollow core fiber as a spatial filter, like performed in [122]. This way, not only the focusability would be ensured, but also spot sizes and beam pointing could be made constant. Beam pointing before the fiber would result in mere power fluctuations, that are easier to detect and treat statistically in the measurement.

The first measurement was to observe how the induced current changes with CEP. Note that the carriers are still injected at any phase, but there is no net polarization after the laser pulse for certain values. To find these, the pair of thin wedges (apex angle measured as 2.8°) transmitted by the OPCPA beam scans the optical path length in the material. This changes both CEP and duration of the pulses. Therefore we expect an oscillating current with an envelope (that indicates that longer pulses inject and drive less carriers). Compared to [114], fused silica in the IR will not disperse the pulse as much as in the visible domain. The CEP slip however is not too different. At a center wavelength of $2.1 \mu\text{m}$ the decoherence length is given by $L_d = 32.6 \mu\text{m}$ (also see table B.2), while at 600 nm it decreases to $L_d = 15 \mu\text{m}$. This equals a wedge movement of $655 \mu\text{m}$ to offset the CEP by π .

In fig. 6.3, we see the result of one of these scans, performed at an input power of 170 mW . The amount of glass that could be introduced was limited by the dimensions of the wedge and the large beam size (needed to avoid unwanted nonlinear effects, see section 5.4). The step size was set to $47.6 \mu\text{m}$ ($1000 \mu\text{steps}$ of the used stepper motor) and 281 position were evaluated. The signal was taken as the mean of 3 consecutive measurements at each point with an integration time of 100 ms . The error bars indicate the standard deviation of these 3 shots. Over this measurement period, CEP drifts of the OPCPA can be neglected, according to section 5.5.

A sine function with quadratic envelope was assumed and fitted to the obtained data. The result is a period of $657 \mu\text{m}$, which is in excellent agreement to the expectation. The peak voltage was fitted as 1.36 mV .

The charge Q_p transferred can be calculated from this as follows: The measured voltage from the trans-impedance amplifier was taken at an amplification 10^8 V/A setting. For a measurement of 1.5 mV therefore, a charge of $1.5 \cdot 10^{-11} \text{ C}$ was induced per second. For a repetition rate of 3 kHz , this means an induced charge of 5 fC (or about 31000 electrons) per laser shot.

Figure 6.3 shows a measured signal that is not centered on zero exactly, but contains an offset of -0.17 mV . This was first attributed to electronic background noise. However, when we blocked the light incident on the sample, the noise floor was only $1.2 \mu\text{V}$ (standard deviation) (and with the cover removed $4.0 \mu\text{V}$) and centered at zero. The situation changed when the sample was illuminated. Without covers (and without moving the wedge), we observed oscillations on the order of 1 mV . These could be heavily reduced when enclosing the sample by our aluminum cover. We attribute this to radiative noise that is coupled into our measuring circuit, when the light makes the sample a photo-conductive switch. As the lock-in frequency is around 1.5 kHz , where many turbo-molecular pumps work in the lab, we suspect the signal oscillations to be slight variations in their (regulated) rotation speeds. The magnetic fields of these pumps then could have coupled into our current measuring circuit. With a time-constant of 100 ms , the rotation speed variations can easily oscillate in and out of this frequency window.

However, using the shielding the offset could still be observed. As it was also constant over the measurement period, it appeared as being part of the measurement. A CEP-flip of the AOPDF, that is not exactly π , would explain the offset. The oscillation in current then does not exactly add up coherently in the lock-in technique. Instead, a part of the signal is not recovered, which

equals exactly the offset. While we can calculate this error to be only 1 % (this means the real measured peak current is 1.37 mV), the unintended offset in the CEP-flip is 120 mrad. In future measurements, this can easily be compensated by readjusting the CEP in the AOPDF until the offset vanishes.

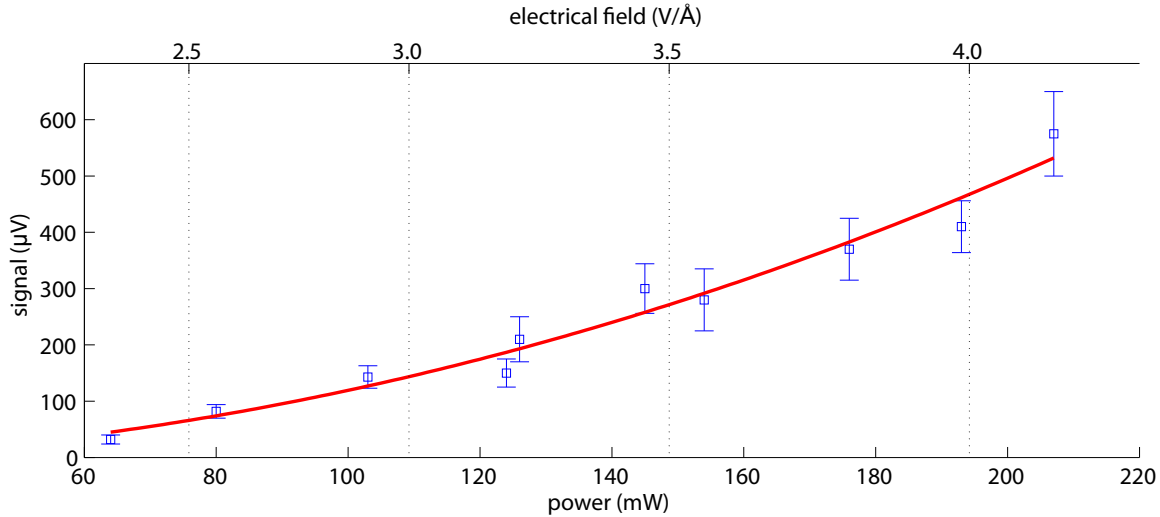


Figure 6.4: Measured peak signal over input power. The fit in red indicates a critical field offset.

Another measurement was performed to find the relationship between applied field and induced maximum current, comparable to [114]. As a means of attenuating the intensity, the pump power of the second stage of the OPCPA was changed. This avoids closing an aperture, which would lead to changing beam diameters. While these are hard to measure using IR detectors anyway, more severe is the spatial response of the sample. Translating only by about 50 μm did sometimes reduce the induced current by about 50%. Similar behavior was observed for the laser source used in [114], so this is not an issue of the OPCPA. Therefore leaving the beam profile unchanged and rather alternating the pump power of the second stage promised being more reproducible. However, slow drifts of the second stage output could be observed over some minutes, leading to a drop in current as well. This was compensated for by alignment of the sample, as a beam stabilizer for the IR was not available to us yet. For consistency, the power scan was not taken in a monotonous fashion, to avoid any thermal hysteresis behavior. The intensity was scanned from about 110 to 350 TW/cm^2 (2.4 to 4.3 $\text{V}/\text{\AA}$). Lower intensities produced a signal hardly distinguishable from the background noise, while the peak intensity was limited by the focusing capabilities of the 100 mm CaF_2 lens.

6.4 Discussion and conclusions

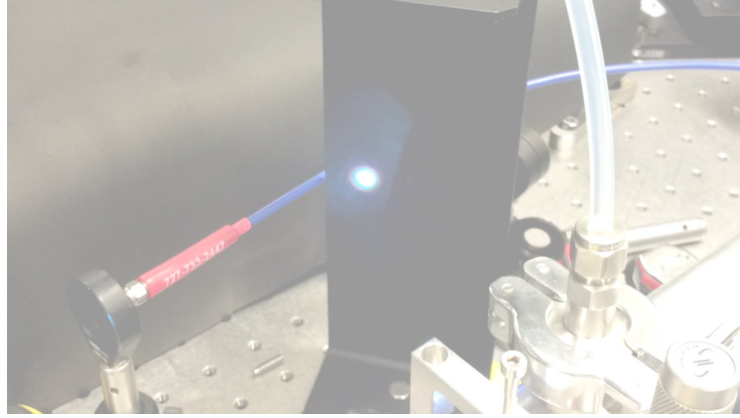
The results shown in fig. 6.4 can be fitted using a quadratic function of the applied power (that means it would be linear in electric field). This yielded the curve indicated in red ($a(x - x_0)^2 +$

$b(x-x_0)+c$ with $a = 0.013 \mu\text{V}/\text{m}^2\text{W}^2$, $b = 0.3 \mu\text{V}/\text{mW}$, $c = -6.9 \mu\text{V}$ and $x_0 = 12 \text{ mW}$). From the fit an offset of 23.2 mW can be extrapolated (about $1.43 \text{ V}/\text{\AA}$). This should be equivalent to the critical field F_{crit} from section 6.1, where the adiabatic passage leads to a non-vanishing tunneling rate and induces a polarization in the dielectric. Why this tunneling rate does not scale exponentially above threshold, is not really clear. It could be attributed to defects in the amorphous fused silica used (therefore a cross-check with crystalline quartz should be performed).

The measurements shown here only serve as a demonstration for the usability of the OPCPA developed in the previous chapters. The induced current is comparable to what was observed in the visible domain before [114] and a clear offset in induced current is shown, indicating a critical field F_{crit} . Still some measures could significantly improve the experiment: First, alignment appeared to be very critical. The warm-up of the crystal when varying the pump current leads to a shift in the output beam pointing and therefore the sample needed re-alignment. To avoid this source of systematic error, a beam stabilizer (as described in section 2.1) using InGaAs position sensitive devices will be used in the future. Second, the intensity of the OPCPA output should be varied without the need to change the characteristics of an amplification stage. Therefore a pair of wire-grid polarizers will be used in the future, to avoid changes in the temporal as well as spatial profile of the used pulses. Both measures should make long-term measurements possible, even without using a slow CEP feedback loop (see section 5.5).

Another effect in the IR to be considered is the anomalous dispersion, which can lead to significant pulse shortening inside the sample [52]. In fact, chapter 7 observes self-compression of the IR pulses in the 1.0 to $1.8 \mu\text{m}$ regime, however in a gas-filled hollow core fiber (with its own dispersion characteristics). More detailed modeling of the pulse propagation is therefore needed to interpret the data better.

The total current measured at the electrodes should be the sum of the currents generated inside the dielectric. Therefore, with infrared pulses (where dielectrics are in general less dispersive) the decoherence length L_d should determine the overall measured current (neglecting higher order effects like SPM). An interesting idea is therefore using BaF_2 as dielectric, which shows very little dispersion ($\text{GDD} = -6.6 \text{ fs}^2$) and an extremely large decoherence length of $L_d = 157 \mu\text{m}$ at $2.1 \mu\text{m}$ (vs. for example fused silica with $L_d = 32.6 \mu\text{m}$, see also table B.2). This combination is unmatched by any other suitable material and should yield much higher current. As the dispersion is so favorable, even quasi-phase-matching of the generated currents could be envisioned. By patterning the electrodes as a comb with the spacing of L_d , over 20 of such electrodes could add up (linearly) to a sizable current before the pulse duration has doubled by dispersion (or over 40, when pre-compensating for the chirp). Together, this could increase the induced current by about two orders of magnitude to the nA level. However, at the used intensities nonlinear effects will probably become significant. Chirping the electrode comb distance would be a possibility to compensate for those.



Chapter 7

Generation of phase-stable continua spanning three octaves

7.1 Motivation for super-octave spectra centered in the NIR

In chapter 2, we used difference frequency generation (DFG) to generate more than one octave of phase-stable infrared spectrum with sub- μJ energy. Although this concept is scalable with an efficiency of over 10% [34], it still relies on broadband seed and pump pulses, which are difficult to generate efficiently. Also, the pulses are chirped by the DFG crystal to some extent and the CEP cannot be modulated at high speeds, as needed in experiments like the one described in chapter 6.

In order to reach higher energies, chapter 5 showed the amplification of a broadband OPCPA around $2.1\ \mu\text{m}$. Energies of over $100\ \mu\text{J}$ could be reached with pulse durations below two field cycles. Although scalable in principle, the used PPLNs are not available in large apertures and with good poling quality in the near future [63]. To overcome this limitation and allow for scalability using future OPCPA pump sources, in this chapter the amplified signal of chapter 5 will be first boosted by a third amplification stage. Using a bulk lithium niobate crystal the pulse energy can be increased further to over $1\ \text{mJ}$. As the phase-matching of the bulk crystal is inferior to its poled counterparts, the amplified bandwidth is limited (see fig. 1.3), but still supports sub-three-cycle pulses.

Then, broadening in a gas-filled hollow core fiber (HCF) will be used to extend the spectrum. We will see that this works even much better than using traditional Ti:Sa-based NIR sources like in section 2.2. Low-order harmonics and cross-phase-modulation stimulate the process and provide us with a remarkably flat super-octave spectrum, while the throughput remains over 60%.

This phase-stable and scalable light source should then allow sub-cycle pulse generation using a waveform synthesizer, very similar to [50]. Future application after field synthesis would the comprise probing the sub-fs dynamics of the carriers generated in chapter 6 and the generation

of isolated attosecond pulses in the water window, with a setup as described in [102]. In fact it was shown previously [6] that HCF-filtered IR OPCPA sources provide a significantly improved HHG yield. Cleaning up the mode profile of the OPCPA is especially important in our case, since we found that the PPLN inhomogeneity in the second stage is already quite severe. This limited the achieved throughput of the HCF setup. To increase the efficiency of the booster stage further, we also test a limited-bandwidth OPCPA configuration. Since the spectral broadening appeared comparable at slightly higher pressure and the output power was increased to about 1.3 mJ without any further optimizations in the OPCPA stages, this was found to be a viable path to mJ-level three-octave-spanning spectra at 3 kHz repetition rate in the very near future.

The efficiency of the super-octave generation is of special interest, since a competing approach of synchronizing individual OPCPA channels [58] in principle offers higher throughputs. While the latter approach allows for efficient non-collinear NIR OPCPA [35] and direct phase-control using AOPDFs in each channel (which is closer to the idea of a real synthesizer), it also requires sub-fs synchronization of whole OPCPA stages including the necessary CPA setups. Moreover inherently CEP-stable seed generation is not easily available at shorter wavelengths, which dictates the use of another (CEP-locking) servo loop. All these difficulties are circumvented by our DFG-seeded collinear approach that instead takes advantage of the impressive spectral broadening in the IR regime.

7.2 Boosting the OPCPA output to mJ level

7.2.1 Broadband amplification using bulk lithium niobate

Using the same seed stretching ratio as in chapter 5, the bandwidth supported by bulk lithium niobate is reduced compared with the highly nonlinear and better phase-matched (see section 1.2.2) PPLN. This is why the crystal length was held short, but using 1.5 mm, the necessary pump intensity for ample amplification was excessive and very close to the damage threshold. With a 2 mm long crystal a compromise between high pump intensity and more phase-mismatch was used to amplify the full bandwidth shown on the left of fig. 7.1. The output power typically reached 3.0 W and was also affected by the compromise between pump depletion and bandwidth.

A second harmonic FROG (as performed in chapter 5), yielded the spectral phase shown on the left of fig. 7.1. As it deviated by less than π over most of the bandwidth, the pulse was sufficiently compressed for the spectral broadening, which again would induce chirp to the 20.2 fs pulse, still being a little less than 3 cycles. Because of the limited phase-matching of bulk lithium niobate, the transform limit is only 16.1 fs. This shows how much the short-wavelength spectral components below 1.7 μm helped to shorten the pulse in chapter 5.

The beam profile of the amplified output is shown on the left of fig. 7.2. It was recorded with a pyroelectric camera (Pyrocam III, Spiricon) and is not exactly Gaussian, but shows large pedestals. Later this issue with beam quality could be attributed to the crystal of the second stage, see sec-

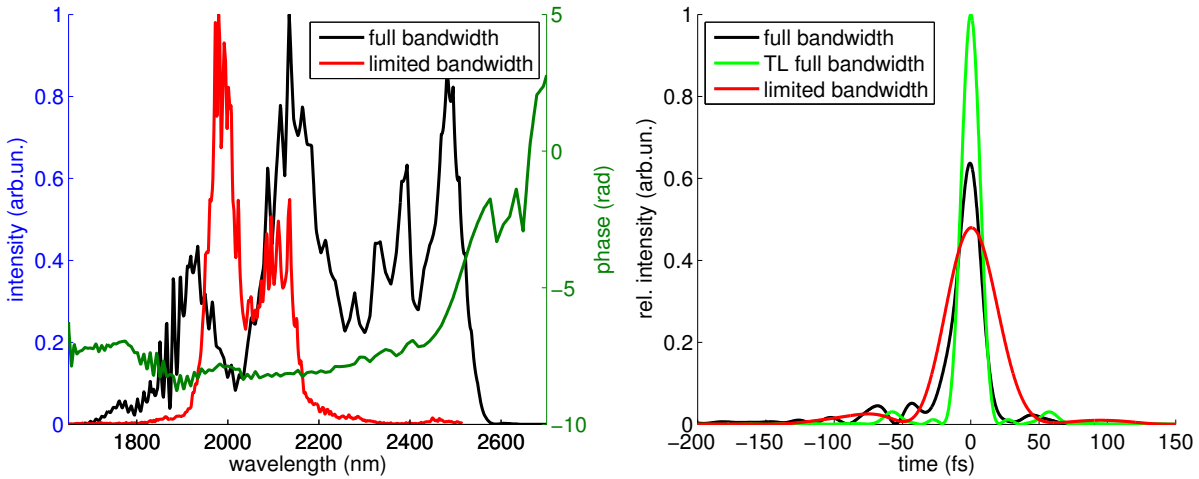


Figure 7.1: Left: The spectral amplitude and phase of the amplified booster stage (at full bandwidth) and the spectrum of the limited bandwidth configuration. Right: Temporal pulse profiles (normalized to the respective intensities) of the booster stage for both broadband and narrowband configurations (transform limit 16.1 fs, full bandwidth 20.2 fs, limited bandwidth 43.3 fs).

tion 7.4.2. As the pyroelectric camera works with high frame rates, it was used to estimate the stability of the amplified output. The pixel-values shown on the left of fig. 7.2 were integrated and are plotted over time (framerate of the camera was about 25 fps). The output did show significant fluctuations, as shown on the right of fig. 7.2, particularly over longer periods, where sudden spikes occurred. These can be attributed to two distinct effects.

First, the pump diodes of the pump laser (see chapter 3) are not frequency stabilized. Therefore the internal chiller valve opening leads to a shift in the pump wavelength around 939 nm. As a consequence, the absorbed pump energy on the thin disk is altered and so is the output power. This happens on a time scale of a few seconds, and long periodic power fluctuations in the OPA are the result.

Second, the Ti:sapphire based amplifier is phase-stabilized with the assistance of a slow loop. Since the DFG-based seed generation is phase-locked anyway, this CEP offset is not of any interest to us. However, the slow loop actuates with the piezo-induced movement of one of the compressor prisms. Using fused silica, a CEP shift of π is induced by an additional optical path of 28.9 μm around a center wavelength of 800 nm. This however is equivalent to a shift in delay of 96 fs. As the compensating synchronization in chapter 4 is limited in fast piezo stroke and the long-range stepper-motor based translation stage is tuned to working rather slowly, this change in optical path can deteriorate the stability of the OPCPA significantly (as the delay in all stages is offset). The measurements in chapter 4 were performed with no slow loop running therefore.

Unfortunately, most devices employed to act on the CEP will change the temporal delay, so apart from using a AOPDF or a 4f-shaper, no other appropriate solution is known to the author for this issue.

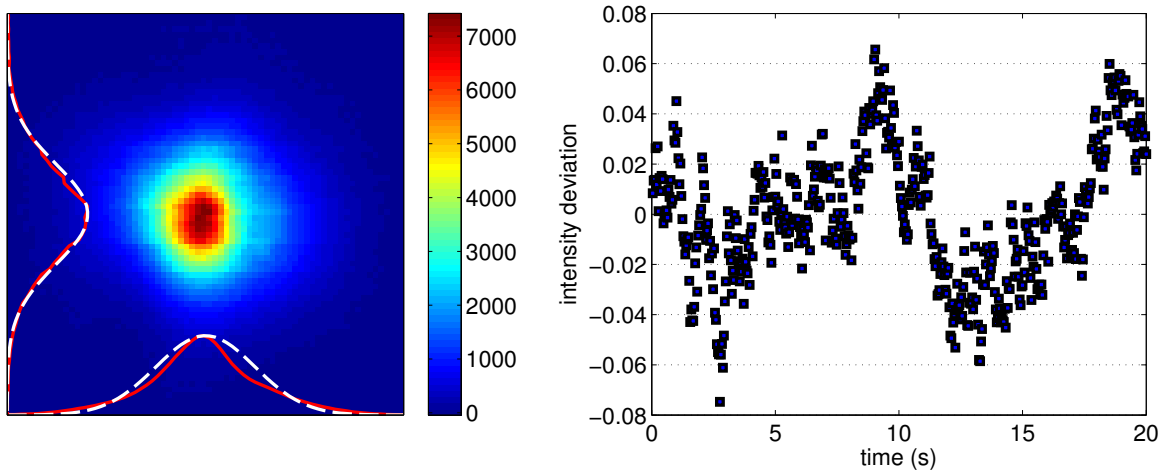


Figure 7.2: Left: Beam profile of the third amplification stage, right: Fluctuations of third stage output amount to 2.81%.

Compared to first and second stage, the third stage amplifies very little in comparison, meaning that the amplification is less sensitive to timing jitter there [91]. In fact, the fluctuations seemed to be inherited from earlier stages, as sharp spikes in output power were more prominent there, while short term stability was better. In order to increase the overall stability therefore we would need to limit our stretching in first and second stage even more at the expense of efficiency.

Pump and seed beam profiles in the third stage were optimized for efficiency. They are shown in fig. 7.3 with their Gaussian fitted spot sizes. The seed spot size was increased by use of a mirror telescope. The pump intensity amounted to about 45 GW/cm^2 .

Important for a high-gain and low seed OPCPA is the superfluorescence (SF) level. In order to estimate an upper value for it, we block the seed in front of the first stage. This is important, since the SF is given by the total amplification of the OPCPA system (which is typically highest in the first stage). Usually the later stages alone do not show any recognizable SF at all. Since we do not extract any pump energy out of the crystal when not seeding it, the amplification is higher than in the seeded case. Therefore this can only be a worst-case estimate. Figure 7.4 shows the (seeded) amplified signal and the unseeded SF. The latter was integrated on the pyroelectric camera, where also noise from ambient optical sources was detected. Since only the emission on the beam axis is of interest here, an aperture with a fitted radius of $2w$ was applied. When summing both pixel areas and dividing them, a SF level of $8.1 \cdot 10^{-4}$ is found. This is a lot better than published in [28], since the BBO-based DFG seed generation (described in section 2.4.2) is much more efficient, and consequently the total amplification could be reduced.

A more sophisticated way of characterizing SF would be to slice spectral holes inside the seed pulse and detecting how SF fills these spectral vacancies [46]. However, this is limited by the dynamic range of the spectrometer at low levels. In our case the NIRQuest512-2.5 (Ocean Optics) is specified with a minimum dark noise of 16 counts (RMS) at 10 ms integration time, so the 16 bit resolution would not allow any reasonably precise measurement even for an undepleted

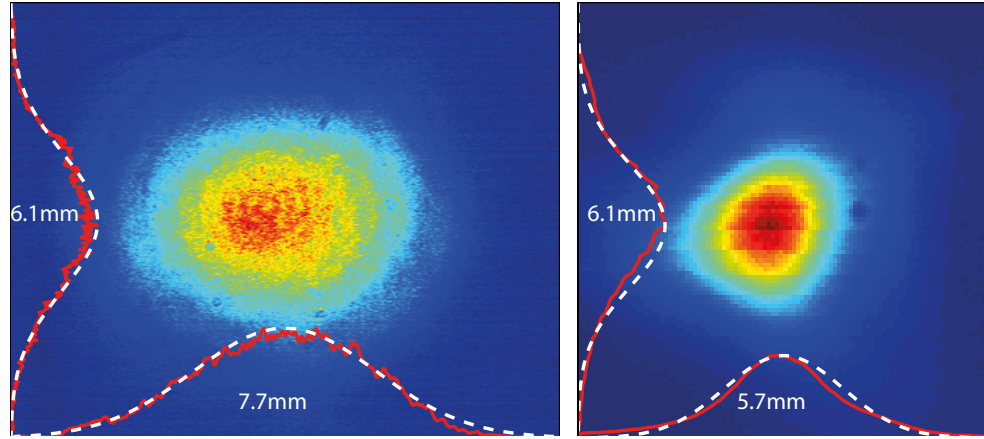


Figure 7.3: Beam profiles of pump (left) and seed (right) of the third amplification stage together with Gaussian fitted spot sizes ($2w$)

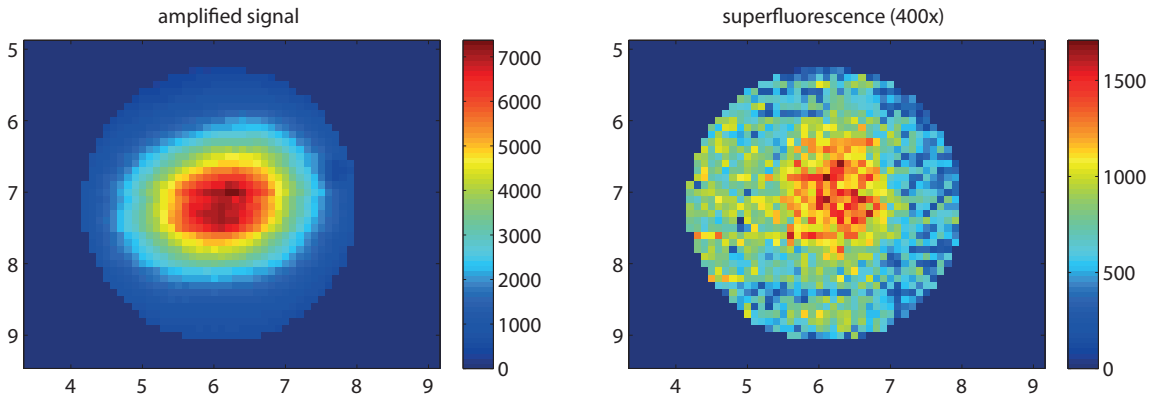


Figure 7.4: Superfluorescence level measured with pyroelectric beam profiling camera when blocking the seed. Spatial units in mm.

pump.

SF was recently investigated [56] and an effective input noise power could be found as

$$P_{\text{noise}}^{\text{OPA}} = 2 \frac{n^3}{2\pi} \hbar \omega \Delta \omega \quad (7.1)$$

Larger bandwidth $\Delta \omega$ (or longer pump pulses) will consequently lead to more SF energy. $P_{\text{noise}}^{\text{OPA}}$ competes with the seed signal for gain, but will usually experience better phase-matching (as it is perfectly seeding the pump profile in space and time) and small-signal gain (unless the pump is depleted) [91]. The signal-to-noise ratio (SNR) can therefore be defined as the ratio between P_{seed} and $P_{\text{noise}}^{\text{OPA}}$. Placing the AOPDF after the first stage would decrease its total gain (in favor of a better SNR and better pump depletion), but unfortunately is not possible in the OPCPA of chapter 5, as the specified AOPDF damage threshold [31] is significantly below the first stage

amplified signal. Furthermore, as we overcompensate the positive dispersion in the AOPDF (for efficiency reasons, see section 5.2), the transmitted pulse is even compressed within the AOPDF crystal. This would lead to more unwanted B-integral, as discussed in section 5.4 and hamper the compression considerably.

7.2.2 Narrow band amplification for more efficient super-octave generation

The spectral broadening with a HCF and Argon gas lead to extremely broad spectra for the full third stage OPCPA spectrum (of section 7.2.1) indicated in fig. 7.5. Since the broadened spectrum seemed to be not limited by the input bandwidth, longer OPCPA pulses were also tested to achieve a similar result.

If the seed pulses are stretched longer than the pump pulse duration, the center wavelength can be tuned by simply choosing the delay. The bandwidth is then selected by the stretching ratio. While usually 1.5 mm of silicon is employed to compress our pulses, here 6 mm is used. Note that the frequency bandwidth is only constant for different pump-seed delays when applying a strictly linear chirp in frequency. As mentioned earlier however, silicon shows a little higher order chirp (although much lower than most dielectrics, see appendix B.1).

Limiting the bandwidth also increases the efficiency of the AOPDF (as it is limited by transducer power), so all stages benefit from enhanced seeding as well as less phase-mismatch and better temporal overlap of pump and seed pulses. Possibly, more narrow-band DFG seed generation (compared to section 2.4.2) could be even more efficient and increase the seed energy considerably. According to eq. (7.1), less bandwidth would improve the contrast of the OPCPA even beyond this effect.

Using the same crystals and pump intensities like before, the output increased to 80 mW in the first stage and 460 mW in the second stage. The third stage output was increased to 3.8 W. However, for a limited bandwidth longer crystals could be used in the DFG and OPCPA stages to boost this amplification further. This should allow one to drive the third stage further into saturation without damaging the crystal by excessive pump intensity, while stability would also improve. At the same time, second harmonic generation (as discussed in section 5.4) of seed and idler (that was very considerable in this stage and could reach over 50% of the output power) would be further limited by using non-collinear geometry [15]. However, for the experiments conducted below these resources were not available. Nevertheless, it seems possible to compensate for the loss induced by spectral broadening with more efficient use of the pump energy in a narrow-band OPCPA.

Since all OPCPA stages easily support the limited bandwidth, their spectra look about identical. The center wavelength was optimized towards best performance with regard to the spectral broadening. This means tuning all the delay stages. The used limited spectrum is shown on the left of (fig. 7.1, limited bandwidth). Since the applied phase was identical to the broadband

case characterized before (full bandwidth in fig. 7.1) and the additional silicon dispersion was compensated by the AOPDF (as demonstrated in section 4.2.2), the retrieved phase should apply here to a very good approximation as well. This increases the pulse duration to 43.3 fs. However, from the temporal intensity shown on the right of fig. 7.1 the energy content in the main part of the pulse was calculated to be 91.9% for the transform limit, 81.8% for the full bandwidth and 91.6% for the narrow bandwidth case. As SPM of intensity components outside the main pulse will only complicate the spectral phase, a longer but better-compressed pulse is beneficial for spectral broadening.

The slightly reduced intensity with longer output pulses is not an issue. In section 7.4 HCFs with core diameters from 200 to 400 μm were used together with Argon pressures of 500 to 2000 mbar (absolute pressure). Tuning these parameters always resulted in good performance, with some variations in throughput and mode profile quality (a typical profile is shown on the right of fig. 7.9). The numbers in the following sections are therefore typical values.

7.3 Indications of spectral broadening in the NIR

While still running the OPCPA with full bandwidth, clear indications of efficient harmonic generation were already obvious (also compare with section 5.4). The limits for high and low gas pressures are explored in this section and the spectrometers used for the characterization of the generated super-octave in section 7.4 are photometrically calibrated in appendix C.2.

7.3.1 Onset of THG

To align the coupling of the invisible OPCPA beam into a (250 μm core diameter) HCF, low gas pressures of Argon or Neon were used. With Neon, no significant broadening was reached at 2 bar, but a clear broadband third harmonic was generated. The same applied for lower gas pressures in Argon (below 500 mbar). In fig. 7.5 the broadband OPCPA output is illustrated together with the generated third harmonic (TH). Note that the third harmonic part is scaled up and the fundamental is clipped above 2.5 μm by the spectrometer detector. Still, the outer limits of both spectra match well, so the process appears very broadband, due to little phase-mismatch. Also one can observe some second harmonic (SH) of the OPA that was transmitted through the silicon compressor ($> 1060 \text{ nm}$). This is back-converted light and also explains the modulation in the fundamental (see section 5.4). The dip in the third harmonic can probably be attributed to the onset of a higher order mode inside the HCF. It is very sensitive to alignment and did not show for smaller core sizes or in a filament.

The HCF did not provide any advantage in THG over using a filament. In fact, by coupling into the HCF, the third harmonic beam profile degraded and coupling was very hard to obtain (compared with the broadened case for higher pressures). There did not seem to be sufficient guiding of the TH mode. Also no fifth harmonic was detected in Neon yet. Since we did not

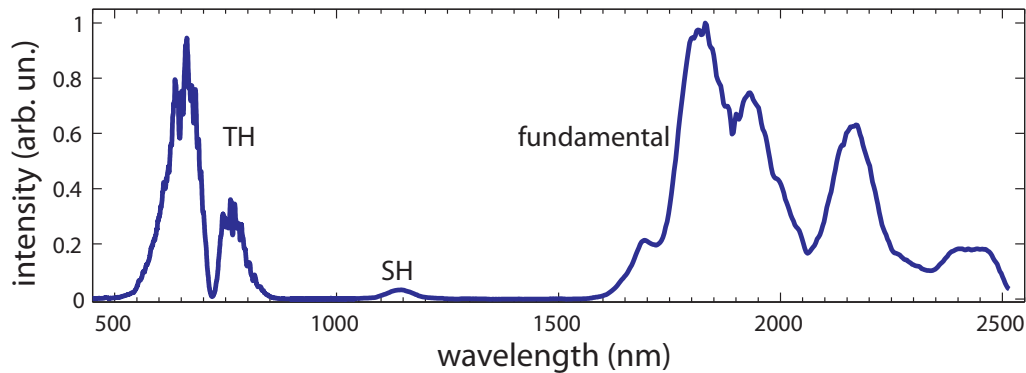


Figure 7.5: Spectrum of fundamental and third harmonic for Neon gas (2 bar). The third harmonic was scaled up for visibility.

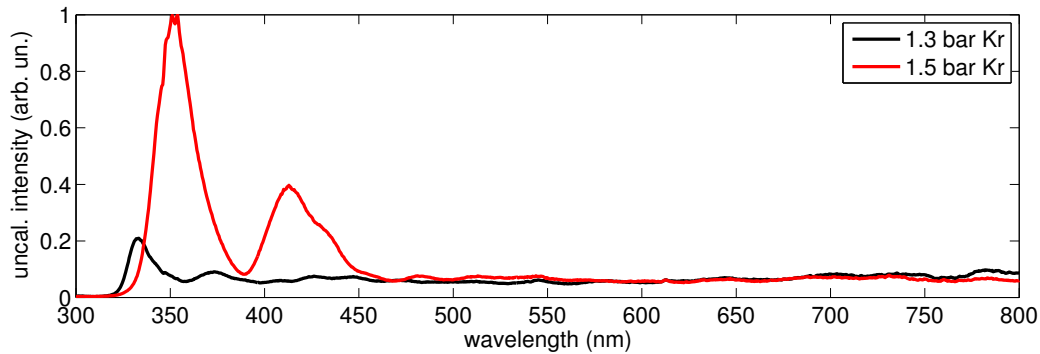


Figure 7.6: Improvement of fifth harmonic for higher (Krypton) gas pressure.

want to increase the pressure to much for Neon gas, Argon was selected for more broadening with moderate pressures. Also smaller core sizes (200 μm) are used in the following to avoid higher order modes.

7.3.2 Onset of fifth harmonic and blue white light

For high pressures of Argon (1500 mbar) inside a HCF, the spectrum is much more shifted to the blue side and the fifth harmonic becomes prominent. Since our VIS spectrometer can only measure down to 350 nm, at this wavelength, the calibrated noise is already pretty considerable. Therefore using a more suitable (UV-enhanced) spectrometer (Maya2000, Ocean Optics) allowed an uncalibrated look for the case of the broadband OPCPA. Also Krypton was used in order to not increase the Argon pressure too much and avoid more broadening towards the blue part of the spectrum. It reveals that with 1.3 bar Kr the broadening already fills out the visible region (the Maya spectrometer does have a quite linear response in this region). At the cutoff that reaches down to 320 nm, the fifth harmonic of the spectrum is clearly observable, it is limited

by the short-wavelength edge of our broadband OPCPA configuration at 1600 nm. With 1.5 bar Kr the generated continuum appeared even more blue. The spectrum in the UV exhibited a clear spiking while not shifting any more to shorter wavelengths. Fifth harmonic phase-matching seemed to benefit from the even higher pressure and seemed to define the limit of the continuum in the UV under these conditions. Maybe using (less dispersive) Argon and much smaller core sizes for higher intensities could extend the spectrum further into the UV and be interesting for generating VUV in the future.

It is known that low order harmonic generation in HCFs using broadband pulses does show a clear optimum pressure [41]. This is generally reduced for low ionization potential noble gases. Therefore with Argon we also could generate a strong fifth harmonic, however the broadening towards the blue part of the spectrum is already very pronounced then.

In conclusion, at higher gas pressures the fifth harmonic is enhanced and the spectrum does not broaden any further beyond the fifth harmonic. Since the parameters allow us to work with Argon around 1 bar, this is the (very economical) setting that will be used in the following section. Also the fact that the OPCPA bandwidth had little influence on the process (and could be compensated by more gas pressure), can be used to our advantage. Using the narrow-band configuration (of section 7.2.2) in section 7.4, the continuum should be generated most efficiently.

7.4 Generation of a super-octave continuum

7.4.1 Experimental setup

In the following experiments, only the narrow band OPCPA configuration of section 7.2.2 will be used. Also the second stage of the OPCPA will not be used any more (see section 7.4.2). Therefore 500 μJ pulses around 2.1 μm at 3 kHz with a bandwidth of around 250 nm (compressed to 43.3 fs) were focused with a $f = 750$ mm CaF_2 lens into a 200 μm HCF with a length of 365 mm and an absolute pressure of 1 bar (Argon). The dispersion was optimized in second order (with higher orders previously compensated using the AOPDF) for optimum broadening after the fiber. Brewster windows were CaF_2 for the input side and IR grade fused silica for the output (1 mm thickness each). The calibration for the spectrometers used in the following sections is described in appendix C.2.

7.4.2 Issues with beam profile

The useful input power for the HCF was limited by the 2nd stage crystal. The PPLN did not seem to amplify clean wavefronts. This was visible by the mode structure of a filament directly after the compressed 2nd stage. The movement of irregular shaped modes directly correlated to the movement of the PPLN crystal. Since we are aware of the inhomogeneities of these large aperture PPLNs [63], this is a technical limitation that we can currently not overcome. Because

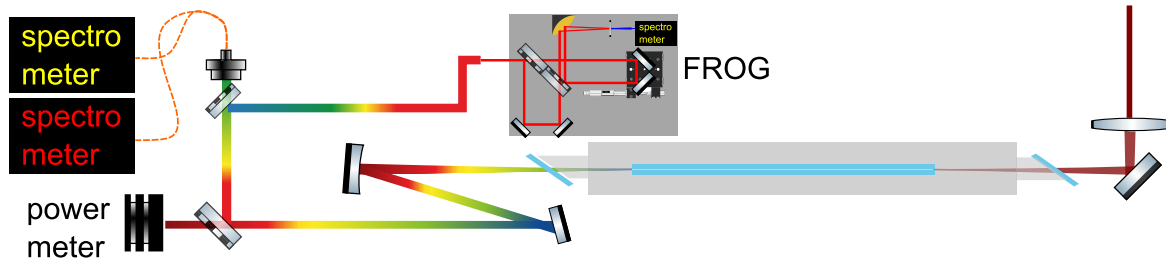


Figure 7.7: Setup for the spectral broadening of the OPCPA output and the following characterization.

of this degradation of the beam profile there is a significant part of the focused light coupled inside the HCF cladding. The efficiency of the coupling consequently dropped to less than 35% with all OPCPA stages pumped. Thus, for further investigation the OPCPA was run without second stage and the input power of 1.5 W resulted in an output power of 1.0 W. This clearly indicates that with a clean spatial OPCPA profile, the throughput of the HCF with 2.1 μm pulses is very good and can be at least comparable to traditional Ti:Sa-based sources [17]. It could be explained by the lack of significant ionization for the compressed long-wavelength components.

Replacing the 2 mm thick PPLN with a thicker bulk lithium niobate crystal in the future would not limit the OPCPA bandwidth any further, while providing comparable amplification. Using OPCPA crystals with high quality also avoids generated light inside the cladding of the HCF to appear on the measured spectra.

7.4.3 Increasing the pressure

The spectral broadening in the HCF was then scanned over Argon pressure. Without the amplification from the second stage, the third stage is not seeded sufficiently any more, therefore the stability of the output is slightly impaired.

The pressure scan from 700 mbar to 1000 mbar is shown in fig. 7.8 and was performed using a 200 μm HCF. The reason for this not very wide range is that the coupling to the fiber changes because of self-focusing before the fiber. Therefore a large range would change the transmission and require realignment of the focus position or even a change of the focusing optic and fiber diameter. However this would make the measured on-axis spectra very dependent on alignment and not show a clear trend that helps understand the broadening process, which is the primary motivation for this measurement. Note how at low pressures SPM, THG and the 5th harmonic start building up. Since the input spectrum is limited, we only expect UV components down to 400 nm here. With increasing gas pressure, the fundamental and TH are broadened and finally their spectral components will merge. Around the spectrometer overlap region at 1 μm (gray area in fig. 7.8), both spectrometer detectors are quite insensitive and the TEC cooled NIR spectrometer can build up a significant thermal offset over time. Therefore the steps in some spectra are not to be taken too seriously. Note that some background around 1.1 μm even for low pressures,

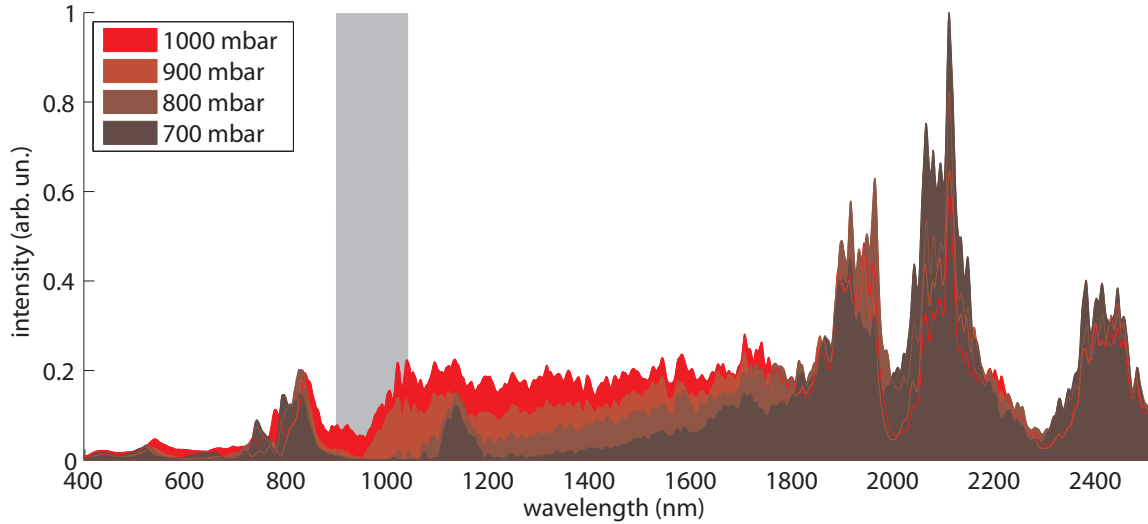


Figure 7.8: Spectrum of the 200 μm HCF broadened output using Argon

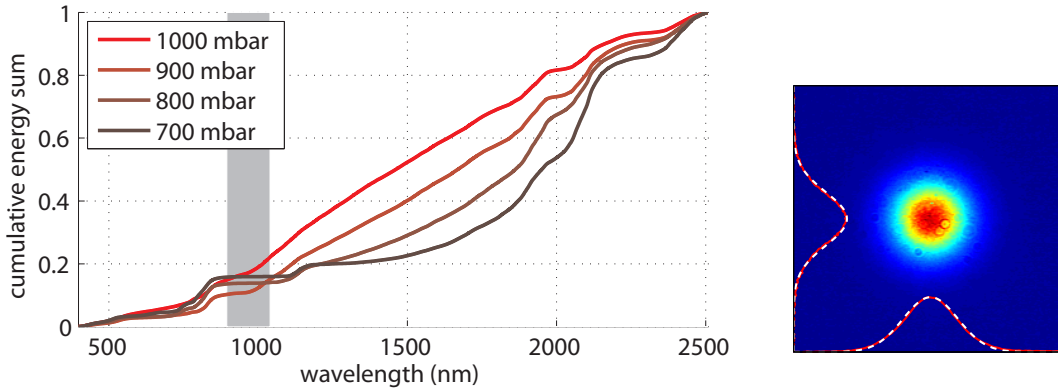


Figure 7.9: Left: Cumulative sum over fig. 7.8, corrected for photon energy, right: Beam profile out of the HCF, measured with a silicon CCD.

is due to the back-conversion/SHG in the OPCPA that passed through the silicon filter. As these components are not compressed, they will not contribute to the broadening process.

For pressures beyond 1 bar (not shown here) the white light starts to appear more and more blue (compare to section 7.3.2), for a pressure of 1500 mbar the short wavelength parts even become very dominant. Since we are more interested in a homogeneous spectrum that is easily compressible using synthesizer optics, this part is less interesting there.

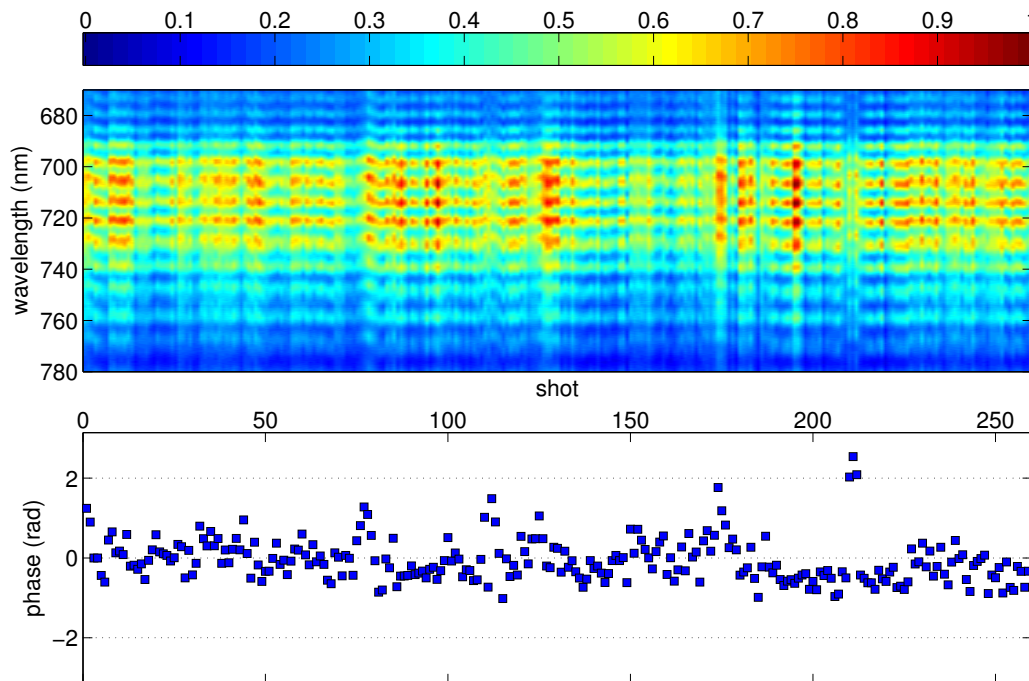


Figure 7.10: f - $2f$ measurement of generated continuum.

7.4.4 Phase stability

In principle, for generating sub-cycle pulses the CEP stability becomes even more critical than using usual few-cycle pulses. Therefore, inherently CEP-stable sources (like those derived from DFG) are a perfect light source for further spectral broadening. However, the phase needs to be preserved in the process, which means high stability requirements for power and beam pointing. But as we have seen in section 7.2.1 already, stable output naturally collides with the principles of ultra-broadband OPCPA [91], especially when suffering from timing jitter. Therefore the measurement here was performed with a limited OPCPA bandwidth.

Since the broadened OPCPA is CEP stable, we do not see any beating between the generated spectral components inside the HCF and expect the output to be CEP stable over the whole frequency range as well. A very simple measurement for this is shown in fig. 7.10, where a 1 mm BBO was used to frequency-double a part of the spectrum collinearly (in the collimated beam), however the stability was impaired by the lack of a beam stabilization before the fiber. The integration time was 100 ms for the shown 260 consecutive shots. A polarizer was used in front of the spectrometer to project both signals onto the same polarization axis and enhance the contrast. The fringes were checked for CEP-dependence by flipping the CEP of every single pulse using the AOPDF, which made them vanish, as demonstrated in section 4.2.3. Fast beam pointing fluctuations into the HCF significantly impaired the measurement (640 mrad RMS), as the interference fringes wash out and are not very deep, however clearly the spectral components appear phase-locked to each other. The interferogram fringes rather drop in intensity or lose

modulation instead of moving. Ref. [142] treats the coupling between intensity inside the HCF and the derived CEP of f - $2f$ measurements in more detail. Given the excellent CEP stability of the driving OPCPA (see section 5.5), we expect to improve this situation considerably using a suitable beam stabilizer in the future.

Note that using a more narrowband OPCPA should decrease the coupling of timing-jitter to phase-jitter in the amplification chain and is therefore preferable in general even beyond the higher conversion efficiency.

7.4.5 Pulse characterization

Using XFROG

In order to prove the well-behaved phase of the continuum, a XFROG measurement was performed and showed a simple spectral phase in the MIR and NIR part. However, the XFROG setup could not retrieve spectral components below $1\ \mu\text{m}$ for the pulse shown in fig. 7.11. The phase-matching did not seem to be responsible, as confirmed by angle tuning. The visible components are certainly stretched very much by the long air path of the measurement setup (about 6 meters for the spectrogram shown in fig. 7.12) and were covered even more by the less dispersive and compressed NIR spectral components in the measurement. A scanning XFROG with dynamic exposure time (and maybe even dithering of the phase-matching angle) could possibly enable this measurement with some effort.

A more fundamental limitation of the light-source to be characterized is poor (chromatic) mode-matching. In both cases (filament and HCF) the beam was re-collimated using spherical metallic mirrors and then translated over large distances for temporal overlap with the reference pulse from the seed laser. Non-perfect collimation caused by aberrations and angular dispersion from slightly wedged output windows could have lead to spatio-temporal distortions in the pulse that effectively limit the sum frequency (and thus the retrieved) spectrum. As the setup itself was quite cumbersome, this was not investigated further. Instead a shorter self-referenced FROG was set up to avoid these possible issues.

SHG FROG

To still obtain information about the spectral phase (especially of our newly generated frequency components), a SHG FROG was performed, using silver coated balanced beam splitters and a $20\ \mu\text{m}$ BBO crystal. Type-I phase-matching was angle-tuned towards the NIR part, so that other spectral components are largely discriminated in the retrieved spectrum. Also the SHG signal was delivered using silver optics into the spectrometer slit, absorbing fundamental frequency components below 600 nm. Nevertheless, the shorter and therefore less dispersive setup allowed measuring the spectral phase of the short-wave visible components of the continuum. Since their phase seems to be well-behaved, we do not expect any issues from the low-order harmonics

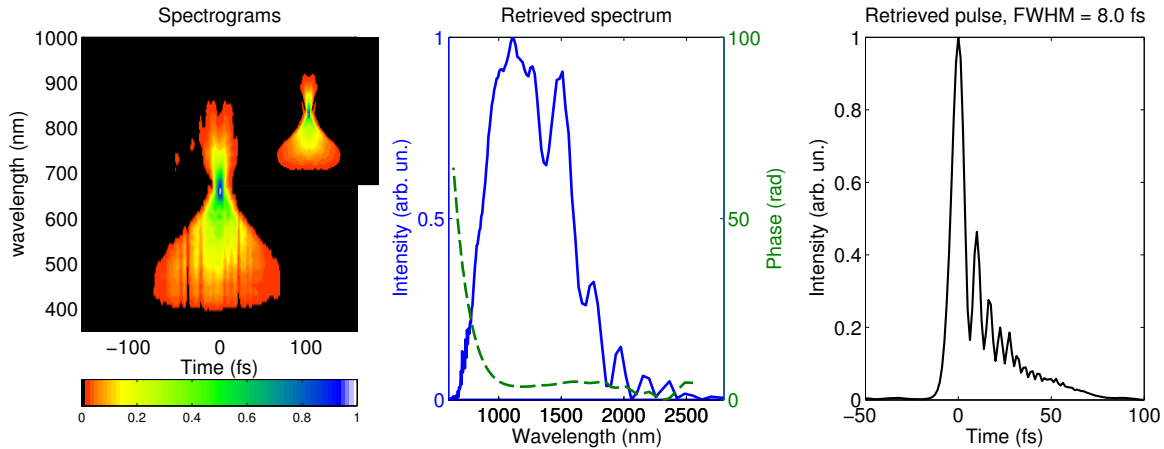


Figure 7.11: Second harmonic FROG of the broadened OPCPA after the HCF.

leading to the considerable width of the broadened spectrum. The pulse duration for the retrieval (shown in fig. 7.11) is 8.0 fs (ignoring the discriminated and chirped VIS and NIR components), the temporal intensity clearly indicates dominant third order dispersion. Note how the phase between 1000 nm and 1800 nm is almost compressed, indicating that the HCF was used under self-compressing conditions. This spectral part alone (centered at about $1.3 \mu\text{m}$) accounts for a pulse duration of 7.9 fs (7.5 fs transform limited), which is around 1.8 cycles. To our knowledge, only [14] created pulses centered at $1.3 \mu\text{m}$ with similar pulse duration (8.5 fs), however at low energy ($> 2 \mu\text{J}$) and not CEP stabilized.

This also compares well to [82] and [115], where two narrow-band OPAs centered around $1.8 \mu\text{m}$ (> 6 cycles) were broadened in a HCF. Compressed by bare fused silica, they yielded 1.5 and 1.6 cycle pulses. Their CEP measurements showed phase-stability on the order of 400 to 600 mrad (RMS).

7.4.6 Brief results in a filament and differences

Before employing a HCF for spectral broadening, filamentation in the same gas cell was performed. The third stage of the OPCPA was still used with its full bandwidth. Yet, the output power is far from the critical power P_{cr} that would let the collimated beam profile collapse in the gas cell and lead to a long filament with significant broadening, so the input beam was focused into 1 bar of Xenon using a $f = 750 \text{ mm}$ plano-convex lens. The filamentation could be stabilized using an aperture in front of the focusing lens, which limited the input power to 900 mW.

The total output power was measured as 650 mW, while long- and shortpass filters together with silicon were used to estimate the relative powers. As the second stage crystal was used, we attribute the limited throughput to unfocusable parts of the beam (that ended up in the HCF cladding before), which did diffract too much before the gas cell output window.

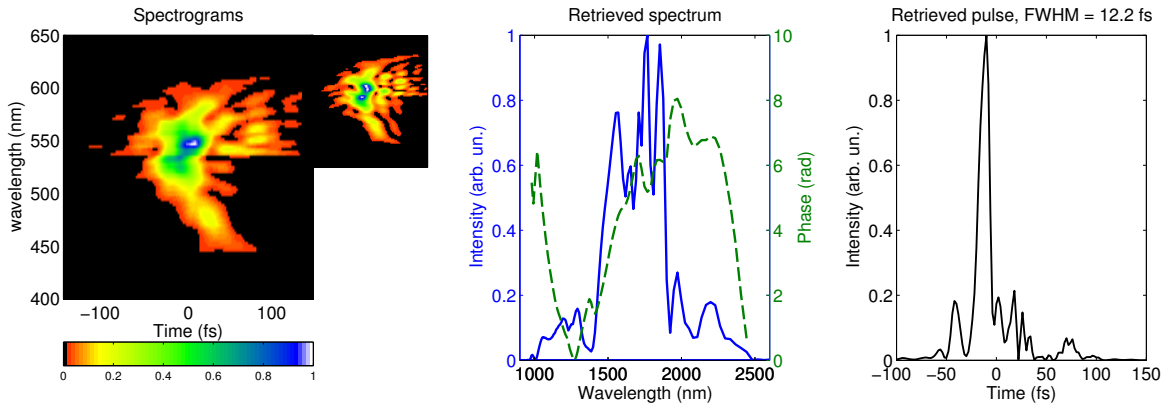


Figure 7.12: SFG XFROG of the OPCPA broadened in a filament.

Obtaining extremely broadband dielectric filters is very difficult and absorption filters often do not provide sharp edges, therefore the following method was devised to estimate the spectral power distribution: FEL1500 (Thorlabs) is a long-pass filter with transmission over 1500 nm and very high attenuation below. The measured 330 mW transmission of the filter thus indicates the fundamental power, over 1.5 μm . Adding coated silicon windows (used to compress the OPCPA) only decreased the throughput by 10 mW. This drop is likely from two-photon-absorption (TPA) or imperfect coating. The silicon window alone transmitted 580 mW, leaving 60 mW to be contained in the short-wavelength part below 1.05 μm .

This was double-checked by using the FES1000 short-pass filter (also Thorlabs), which obviously transmits below 1000 nm, but also above 1500 nm. Used alone it gave 440 mW transmission, while in combination with silicon, 380 mW were measured. This confirms the 60 mW below 1.0 μm . It is especially important to double-check this because the silicon could likely show even more TPA between 1.0 and 1.5 μm , while over 1.5 μm we already observed TPA to be marginal. The residual 260 mW can be attributed to the NIR part between 1.0 and 1.5 μm . It should be noted that the filter transmissions are idealized in this estimation, the actual transmission curves are shown in fig. B.1 in the appendix.

In fact the spectrum was observed on standard spectrometers to be continuous and to possess a visible tail (see fig. 7.13). Both the visible and infrared spectrometers were calibrated over their respective ranges and the absolute count rate between both was calibrated using the above estimation.

An XFROG measurement was performed and is shown in fig. 7.12 to find the spectral phase. The retrieved spectrum is centered at 1.5 μm and the spectral phase dominated by third order dispersion. The retrieved pulse duration is 12.2 fs.

It must be concluded here that filamentation could indeed lead to sufficient broadening. However, the observed filament was only a few centimeters long. Longer focusing (or better yet collapsing of the collimated beam) close to the critical power would have led to a longer filament and better broadening, as shown in [68]. However, a filamentation cell with dimensions of several meters is

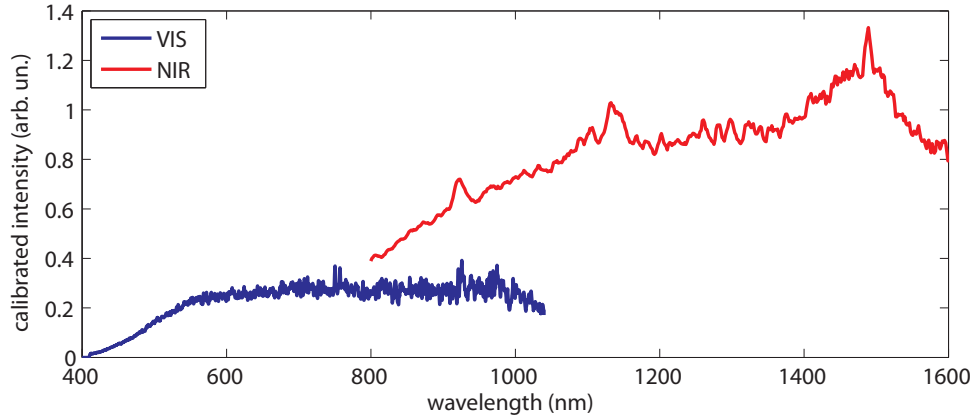


Figure 7.13: Spectrum of broadening by filamentation.

not practical for seeding a waveform synthesizer, which in our case is to be set up next to several compact vacuum chambers. Therefore, the very short HCF used in the previous sections was preferred.

Also the filament did not show the same self-compression behavior as the HCF. The pulse duration did decrease significantly (12.2 fs FWHM), but the pulse is still chirped and the spectral phase nowhere as flat as for the HCF case shown in fig. 7.11. Unfortunately, the SH FROG used in this investigation was not available to us yet when performing the filamentation.

7.4.7 Discussion and conclusions

Limitations of the characterization

The author is aware that the spectral amplitude and phase measurements are not well calibrated/phase-matched yet. However, for a calibrated spectral measurement from 300 to 2700 nm, only very special optics can be used (fluoride delivery fibers and lenses), for collimating the generated output, any metallic material would absorb some part and dielectric mirrors or filters typically offer too little bandwidth. The careful characterization described in [68] gives hints for better (future) characterization. Also standard thermal power-meter heads are not calibrated over the characterized bandwidth, explaining the non-continuous calibrated spectra of fig. 7.13.

The SH FROG is only used to demonstrate the well-behaved (and even self-compressing) nature of the spectral phase. The retrieved spectrum heavily discriminates the MIR parts that were barely phase-matched.

A SFG-based XFROG was performed as well (with the Ti:sapphire seed amplifier as the reference), unfortunately it also has its shortcomings (as discussed in section 7.4.5). The author is not aware of any more broadband characterizations for chirped pulses, but a rough compression

and part-wise characterization of the single synthesizer channels (using wavelength-independent processes like a transient grating) could mitigate the problem.

Discussion and Conclusions

Compression of broadband infrared pulses has seen much interest very recently. *Hemmer et al.* [52] have shown self-compression of 20 μJ pulses at a center wavelength of 3.1 μm by simply inserting a YAG plate into the focus. From appendix B.1, this occurs obviously in the anomalous dispersion regime. The same laser system also showed super-continuum generation inside a solid spanning over 3 octaves [124], however with rather low energy fractions away from the pump wavelength. Around the same time, broadening to 3 octaves in a (Argon) filament has been observed by *Kartashov et al.* [68] using 3.9 μm 12 mJ pulses. The spectral power distribution here was almost flat, which makes this source usable even beyond mere seed generation or low intensity spectroscopy applications.

The hollow core fiber concept on the other hand allows for comparable large pulse energies on the mJ-level as well since the critical power scales favorably in the infrared (see eq. (1.31)) and the ionization rates are heavily reduced. Therefore the typical maximum energy of around 1 mJ achieved by traditional Ti:Sa-based broadened sources [120, 21] can be easily surpassed. Given the scalability of the whole OPCPA (especially in the narrowband configuration of section 7.2.2), this scheme of continuum generation is therefore currently rather limited by the available pump laser (an area which is rapidly progressing, see section 3.1.1 and [135]).

While so-called induced phase modulation [86] (mixing the fundamental with some second harmonic) is usually beneficial for extended spectral broadening, different from theoretical predictions [42], it was not necessary to obtain ample spectral width. Instead, THG is enhanced, since the wave-vector mismatch between third harmonic and the fundamental is much smaller in the infrared [126]. While a previous simulation predicted no prominent effect from the THG at a wavelength of 1550 nm [126], such as XPM, another theoretical investigation [1] and the very recent results of [68] at 3.9 μm have shown both theoretically and experimentally, that the generated TH leads to induced fifth harmonic generation (from four-wave mixing $5\omega = 3\omega + \omega + \omega$). Similar to fig. 7.5, the harmonics were simply frequency-converted fundamentals. At higher pressures they experienced significant broadening that could be quantitatively explained by XPM with the fundamental. It was shown that the broadened third and fifth harmonic did even overlap with each other (caused by XPM), before the fundamental experienced a significant blue-shift (by SPM). Finally it was concluded that the efficient harmonic generation leads to the efficient broadening over several octaves.

In the experiments described here, exactly the same behavior can be observed. For the more broadband OPCPA configuration fifth harmonic generation down to 320 nm was observed, together with a cut-off around 2.7 μm . The generated spectrum therefore even spans over three octaves.

Surprisingly, this is not confirmed by broadening experiments around 1.8 μm in a hollow core

fiber, where SPM did broaden the spectrum, but only to one octave [115, 82]. However, the observation of harmonics is not reported. Given that the OPCPA spectrum used in our experiment did contain $1.8\ \mu\text{m}$ (at least for the broad bandwidth configuration), this seems astounding.

In our experimental setup the broadening using a filament did not yield significant wavelength components below the third harmonic, likely because the interaction length was very limited as the (visible) filament appeared short (2–4 cm). In the HCF broadening however the interaction length is given by the fiber length and the fifth harmonic was clearly visible for higher gas pressure (or more nonlinear gas, see fig. 7.6).

Very interesting was the sufficient spectral broadening even for a limited OPCPA bandwidth, supporting only around 7 optical cycles. This is almost comparable to the situation of most Ti:Sa amplifiers, that are spectrally broadened inside hollow core fibers for a visible continuum (see also section 2.2). Apart from the fifth harmonic reaching down to 320 nm and the more uniform spectrum in the visible part, the broadening using a broadband OPCPA did not show any considerable advantage over the more efficient narrow-band variant. That the process seems to be mainly driven by low-order harmonics and their cross-phase-modulation could be an explanation. It should be noted that here the input pulse was not simply chirped; this in fact should have lead to issues with broadening, as the temporal pulse-shape is then very complicated (given the modulated OPCPA spectrum). Effects that rely on a pulse transient (like SPM and XPM) thus would modulate the phase in a very complicated way, or could even destabilize the broadening mechanism (for example, pre-ionization of the gas by satellite pulses). Instead, first a spectrum comparable to the large bandwidth configuration is generated by SPM. As the pulse does experience much less dispersion around the fundamental than in the visible, this generated fundamental pulse is probably barely longer than in the broadband-OPCPA case, as indicated by the spectral phase in fig. 7.11. Especially the blue wing, that appears to be nearly transform limited in this measurement, is then shifted further to lower wavelengths, while the third harmonic just depletes the whole fundamental slightly (see fig. 7.8). On the left of fig. 7.9 this energy shift to the region 1000 - 1500 nm is clearly visible. In the end, the cumulative sum is rendered almost flat on a wavelength axis, in frequency (that defines the temporal space much better in the synthesizer to follow) the long wavelength components are still more dominant.

Our goal here is to seed a waveform synthesizer comparable to [50], so compressibility of each spectral part of the generated continuum is of paramount importance. Thus the continuum should show a well-behaved spectral phase that can be compensated easily with chirped mirrors. The guiding fiber itself adds dispersion from its geometry. As the effective zero dispersion point (ZDP) can be varied to some extent this way, significant broadening (at least comparable to a filament) is to be expected.

While the pulses of [68] were not temporally characterized, we see a clear indication of material-based dispersion in the filament pulse (fig. 7.12), that probably arises from the fused silica windows of the gas cell. This leads to a dominating third order dispersion part, while several meters of propagation in air (and the broadening gas itself) shift the effective ZDP a bit over that of fused silica (given in appendix B.1).

In the FROG measurement of the HCF broadened spectrum (fig. 7.11), the spectral phase appears much less modulated. Obviously some fiber dispersion shifted the ZDP inside the NIR range and self-compressed regions in the spectrum are the consequence. Note that the identical gas cell was used in both cases.

A more broadband characterization of the generated pulses is necessary to evaluate the compressibility of the spectral parts below 800 nm. The SH FROG shown in fig. 7.11 there shows a diverging phase that stems from absorption of the used silver mirrors to deflect the generated second harmonic and also the phase-matching is clipping the spectrum. However, the temporal characterization in fact can be simplified by measuring the separated channels [50] in the synthesizer later, which then relaxes the requirements on the characterization technique considerably.

Since the waveform synthesizer to follow this setup starts at a wavelength of 700–800 nm (due to the enormous technical challenges in the optical coating design over the given bandwidth), any further extension of the spectrum is not necessary for now. In the near future waveform synthesis of the generated spectrum should yield extremely short pulses (or even field transients). The super-octave shown in fig. 7.8 for 1 bar Argon can be divided into several channels, each compressed individually before being combined again using ultra-broadband beamsplitters. From the spectral phase shown in fig. 7.11, the choice of three channels is quite obvious: while the center channel (1000 to 1800 nm) is self-compressed close to its transform limit (TL) (7.0 fs), the blue channel (700 to 1000 nm) (7.5 fs TL) and the red channel (1800 to 2500 nm) (20.0 fs TL) show much more dispersion, but the bandwidths can be kept below half an octave. Therefore compression to within 20% of the TL should be possible, like in [50]. The center wavelength (calculated by center of mass) is then located around 1420 nm and the TL of the combined spectra (3.4 fs) equals 0.8 optical cycles. It should be noted that linear extension of the spectrum towards the blue end (with a flat amplitude when plotted over frequency) does not yield a shorter pulse in term of field cycles. In this regard, the lower pressure spectra of fig. 7.8 support even less field cycles. Moreover, the envelope loses its meaning at these bandwidths, as the field amplitudes are becoming decisive for even low order nonlinear processes (and therefore pretty much anything of interest).

Conclusions and Outlook

As demonstrated in chapter 2, a CEP-stable octave-spanning infrared seed was generated in BBO, while PPLN failed to achieve comparable output in terms of both spectral bandwidth and output power. Strong contributions from SPM and photo-refraction also showed to be detrimental to the process. Using BBO, spectral bandwidth beyond the requirements of the OPCPA of chapter 5 was generated. In the future, using this source a multiple channel OPCPA system (compare [59]) could be seeded in an inherently CEP-stable fashion, without suffering from low seed energy and a high superfluorescence background as a consequence.

In order to push the limits of phase-matching and therefore support more spectral bandwidth in the OPCPA process, a thin-disk amplifier with a pulse duration of 1.5 ps is employed. The large energies in the cavity lead to a significant buildup of B-integral, which in turn presented major challenges for OPCPA pumping and synchronization. The regenerative amplification worked in a regime of period doubling, so reduction of round-trips (in order to reduce the B-integral) is limited by this dynamics and would require higher input seed levels. For now, the pulse energy was therefore limited to about 20 mJ. Furthermore, the average power was limited by the appearance of higher order transverse modes. Those were the consequence of too large thermal load on the thin disk, leading to both thermal lensing and a non-spherical disk surface.

Since stable OPCPA in terms of output energy and CEP relies on the exact temporal synchronization of pump and seed pulses, an optical synchronization scheme was used in this work. As it still experienced too much jitter for modern few-ps pump sources, active enhancement of the synchronization was performed. A first software-driven feedback loop could reduce the timing jitter to $\sigma = 49$ fs, which allows long-term stable amplification. In order to improve the performance further, our spectrally resolved measurement was adapted to map the delay on a spatial axis. This enabled a standard beam stabilization to be adapted for jitter compensation at high bandwidths, only limited by the actuator speed. The resulting jitter level of $\sigma = 24$ fs also resulted in a stabilized CEP of the OPCPA, as discussed in section 5.5. The single-shot jitter of 15 fs is still very high in our setup and limits the performance of the synchronization. Using higher repetition rates and further investigating and optimizing parts of the amplification chain (as performed in [72]), could reduce this number significantly.

The OPCPA of chapter 5 uses thin, large aperture PPLNs and high pump intensities enabled by the short pump pulses to achieve broadband gain supporting sub-two-cycle pulses centered around 2.1 μm . An output energy of 100 μJ was achieved with excellent short- and long-term

CEP stability, eliminating the need for another slow feedback loop all together for the following chapters. However, limits in terms of scalability were experienced by the insufficient homogeneity of the PPLNs over large apertures and self-diffraction effects in quasi-phase-matched degenerate OPCPA. These effects limit the achieved output power and pulse duration. While many experiments can be easily performed at this energy level, for those requiring larger intensities, chapter 7 provides a solution.

As a first prototype experiment, sub-fs currents in a dielectric are induced by the IR pulses. The results in terms of generated charges were comparable to the ones using a traditional broadened Ti:Sapphire-based system that is actively CEP-stabilized.

Using a two-arm current control setup like in [114] and a waveform synthesizer for the super-octave of chapter 7 (like in [50]), NIR transients would be fully controllable as the electric field could be directly sampled and manipulated. This would resemble a petahertz (solid-state) oscilloscope and function generator with unforeseen future applications. It avoids bulky vacuum-based equipment or HHG techniques such as attosecond streaking (that require large intensities, and scale disadvantageously for larger wavelengths) and could advance the metrology of the shortest IR transients to the PHz regime [71], which is especially important given the difficulties of temporally characterizing the multi-octave pulse of chapter 7.

This was generated exploiting the enhanced tendency of infrared femtosecond sources to generate low-order harmonics. Cross-phase modulation extended the spectrum to about three optical octaves, while the spectral amplitude appeared rather flat after calibration. Therefore, in contrast to bulk filamentation based sources, which are limited in output energy to a few μJ , the compression of these pulses would yield mJ-level IR transients. As self-compression in a HCF was shown to simplify the spectral phase in the NIR, in turn the part-wise compression of the spectrum is simplified further (or not even necessary around $1.3\ \mu\text{m}$). Also the high throughput of the HCF (given OPCPA amplification with good spatial properties) and the conserved CEP stability hold promise for efficient super-octave generation in the IR. Furthermore, the generated continuum bandwidth was not very sensitive to the input pulse duration. This allows a reconfigured narrow-band OPCPA configuration with larger conversion efficiency and could probably compensate for the losses induced by the HCF, while limiting the pump intensities on (potentially) thicker OPA crystals. Overall this represents a much simplified concept for generating CEP-stable mJ single-cycle pulses (and even shorter transients) in the IR. In fact, much shorter pulses than needed in chapter 7 were generated earlier [46], without complicated synchronization and using longer crystals. Sufficient phase-matching of bulk crystals would also circumvent the challenges of large aperture PPLN and allow for better scalability. Even the use of the AOPDF would not be justified then, since 40 fs amplified pulses around $2.1\ \mu\text{m}$ were shown to be compressible using chirped mirror technology [125] alone. With the very well-behaved spectral phase of the generated seed in section 2.4.2, this should not be too challenging.

Future outlook

A designated attosecond beamline was recently set up by Sabine Keiber behind the IR OPCPA. Waveform synthesis of the broadband IR continuum of chapter 7 will be performed there by Olga Razskazovskaya. The field transients then will be used for investigations in solids (like in chapter 6), also employing attosecond pulses from high harmonic generation of the IR driver. Apart from isolated attosecond pulses with a cut-off around 100 eV, which are commonplace using standard Ti:Sapphire driven systems, the NIR transients should push the cut-off into the water window energy regime and beyond (the project of Clemens Jakubeit). Given the high HCF throughput, a more efficient OPCPA configuration and promising results using two color sources like described in [16, 123], the unfortunate wavelength scaling laws for HHG yield could be overcome, providing a bright and broadband soft X-ray source.

Appendix A

Used Acronyms

ADC	analog-to-digital converter
AOPDF	Acousto-Optic Programmable Dispersive Filter
AR	anti reflection
BBO	beta-Barium borate
BiBO	Bismuth Borate
BOC	balanced optical cross-correlator
CCD	Charge-coupled Device
CEP	carrier envelope phase
CPA	chirped pulse amplification
CW	continuous wave
DFG	difference frequency generation
FOD	forth order dispersion
FP 2	Femtopower 2 (Ti:Sapphire amplifier)
FROG	frequency resolved optical gating
FWHM	full width at half maximum
FWM	four-wave mixing
GD	group delay
GDD	group delay dispersion
HCF	frequency resolved optical gating
HHG	high harmonic generation
InGaAs	Indium gallium arsenide
exInGaAs	extended Indium gallium arsenide
IR	infrared
KLM	Kerr-lens mode-locking
KTA	Potassium Titanyl Arsenate
KTP	Potassium Titanyl Phosphate
LBO	Lithium Triborate
LNB	lithium niobate (LiNbO_3)

LWS 1	light wave synthesizer 1
MIR	mid infrared (starting at about 2 μm in this work)
NIR	near infrared (ending at about 2 μm in this work)
NOPA	noncollinear optical parametric amplification
OPA	optical parametric amplification
OPCPA	optical parametric chirped pulse amplification
OPP	optical parametric phase
PC	pockels cell
PID (controller)	proportional-integral-derivative (controller)
PLL	phase-locked loop
PPLN	periodically poled lithium niobate
PPLT	periodically poled lithium tantalate
PSD	position sensitive diode, not power spectral density
QCW	quasi-continuous wave
QPM	quasi phase-matching
regen	regenerative amplifier
RF	radio frequency
RT	round trip (in a cavity)
SF	superfluorescence
SFG	sum frequency generation
SHG	second harmonic generation
SPM	self phase modulation
Ti:Sa	Titanium doped Sapphire
THG	third harmonic generation
TL	transform limit
TOD	third order dispersion
TPA	two photon absorption
UV	ultraviolet
WFS	waveform synthesis
XFROG	Cross-correlation FROG
XPM	cross phase modulation
XUV	extreme ultraviolet
Yb:YAG	Ytterbium doped Yttrium aluminium garnet
ZDP	zero dispersion point

Appendix B

Optics used in the manuscript

B.1 Linear and nonlinear materials

The choice for a suitable nonlinear crystal amplifying around $2\ \mu\text{m}$ is difficult. Many traditional high damage threshold nonlinear crystals used in the VIS and NIR start to absorb either signal or idler wave beyond $2.3\ \mu\text{m}$ (BBO) or just do not show (broadband) phase-matching (LBO,KTA,KTP). Lithium iodate shows very good phase-matching in theory, but failed to cope with large pump intensities. BiBO allows exceptional phase-matching when pumped at 800nm, but absorbs in the MIR as well. Lithium niobate remains as the broadband option, especially when used around degeneracy (when $\omega_{seed} = \omega_{idler}$), which in turn limits the efficiency of the OPA because the idler contains as much energy as the signal wave. Lithium tantalate does not phase-match unless periodically poled. However, LT only offers its high damage threshold advantage in later OPA stages, where PPLT cannot be grown in sufficient sizes and quality. Therefore PPLN (with an even higher nonlinearity than PPLT) was chosen for the lower power stages and bulk LN for the third (booster) stage. However, LNBs relatively high effective nonlinearity of $d_{\text{eff}} = 4.0 \frac{\text{pm}}{\text{V}}$ is an advantage as it allows the use of shorter crystals and larger phase-matched bandwidths.

material (1 mm)	n_2 ($10^{-20} \text{ m}^2/\text{W}$ pump axis)	d_{eff} (pm/V)	GDD (fs ²)
BBO (e)	5.61 [38]	1.9 (SNLO)	-130.8
LNB (e)	13.0 [38]	4.0 (SNLO)	-74.8
PPLN (e)	13.0 [38]	15.9 (SNLO)	-65.5
PPLT (e)		8.8 (SNLO)	
LiIO ₃ (o)		1.5	1.3

Table B.1: Nonlinear materials (in principle) suitable for IR amplification around $2.1\ \mu\text{m}$ at room temperature, n_2 values at pump axis, n_2 Data from David Nikogosyan, Nonlinear Optical Crystals: A Complete Survey

medium (1 mm)	GDD (fs ²)	$\frac{\text{GDD}}{\text{TOD}}$ (fs ⁻¹)	ZDP (μm)	L_d (μm)	transmission (nm)
ZnSe	262.4	0.72	4.82	40.0	500–20000
ZnS	155.2	0.58	3.65	52.5	450–14000
Si	765.4	0.79	-	15.7	1060–6700
LNB(o)	-74.8	-0.08	1.89	15.7	300–5500
FS	-123.3	-0.22	1.27	32.6	210–3710
BaF2	-5.9	-0.07	1.94	158	300–10000
CaF2	-27.0	-0.19	1.56	95.5	150–8000
BBO(o)	-130.8	-0.23	1.38	23.7	196–2200
YAG	-84.5	-0.17	1.61	32.1	210–5500
air	6E-3	0.87	-	1.5E6	230–1690

Table B.2: table of linear materials around 2.1 μm, with group delay dispersion (GDD), its ratio to third order dispersion (TOD), zero dispersion point (ZDP), coherence length L_d and transmission. Sellmeier coefficients from refractiveindex.info and transmission data from Rocky Mountain Instruments Co.

B.2 NIR filters

The NIR interference filters used to estimate the approximate spectral power distribution in section 7.4.6, are shown in fig. B.1. They are taken from the official data sheets. Also the silicon pieces of fig. B.2 are shown, as they were also used in section 7.4.6.

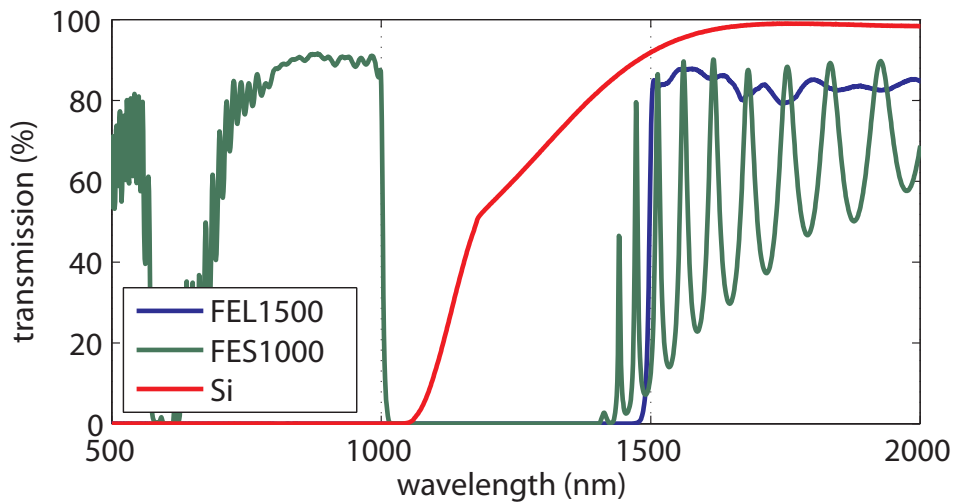


Figure B.1: The transmission of the used NIR interference filters.

B.3 Silicon compressor

The silicon pieces used for compression (manufactured from ISP Optics, Latvia) have an aperture of 2 inches. Very broad AR-coatings ensure efficient stretching and compression of the OPCPA pulses in chapter 5. A throughput of over 98.6% from 1600 to 2600 nm, which means less than 1.5% transmission losses for the main part of the OPCPA spectrum (shown red in fig. B.2) was measured using a photo spectrometer. At higher intensities, TPA is expected (especially below $2\ \mu\text{m}$).

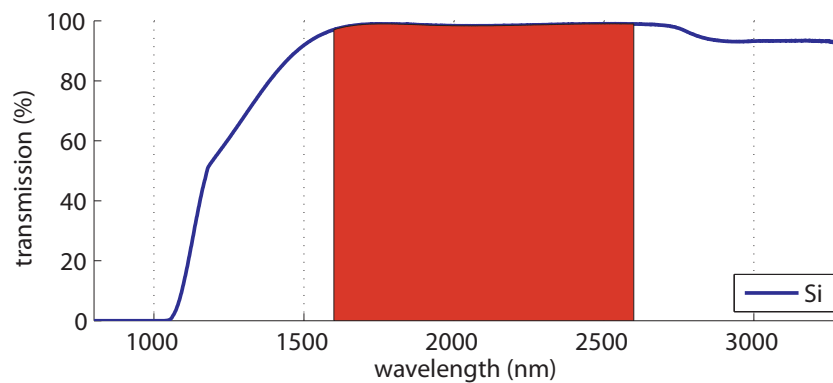


Figure B.2: Transmission of silicon pieces used for compression

Appendix C

Calibration

C.1 Calibration of PSDs

The PSDs, used in section 2.1, section 3.2.3 and section 4.3.5, were calibrated using a micrometer stage and the pump laser of chapter 3. Strong focusing ensured minimal beam-pointing fluctuations on the detector during calibration. The result is shown in fig. C.1, for Hamamatsu S5990-01 with 4x4 mm active area on the left and S5991-01 with 9x9 mm active area on the right. Here, both were read out by BeamLock 4D (from TEM Messtechnik, Hannover) as in section 2.1 and section 3.2.3. The readout electronics for section 4.3.5 is equivalent.

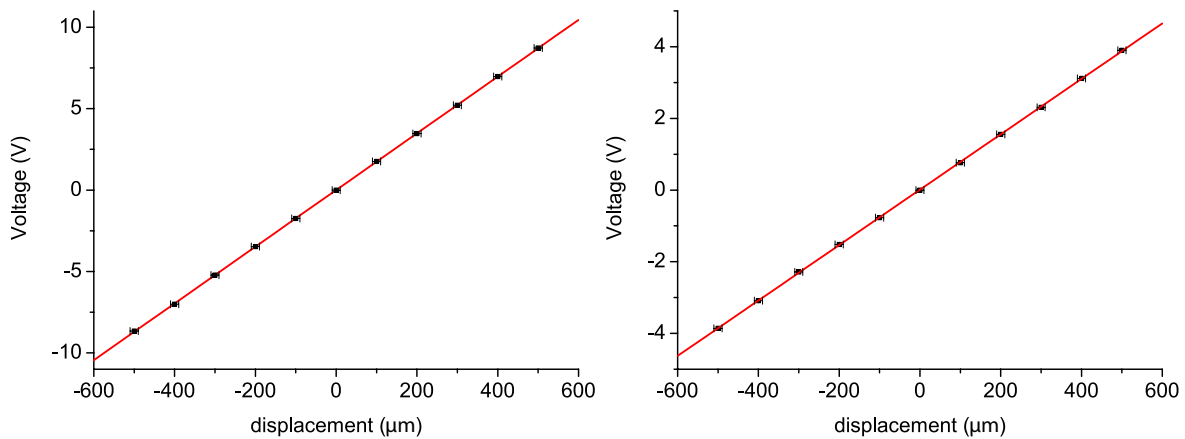


Figure C.1: Calibration of the PSDs used in section 2.1, section 3.2.3 and section 4.3.5.

C.2 Spectrometer calibration procedure

In order to make a more quantitative characterization of the generated continuum in section 7.4 possible, we calibrated our spectrometers using the following procedure. The two main spectrometers used were USB4000 (350-1040 nm, VIS) and NIRQuest512 (900-2510 nm, NIR), both from Ocean Optics. Since they both differ heavily in their spectral response (because of the responsivity of their silicon and exInGaAs detectors and corresponding respective gratings), we calibrated them with a suitable lamp (HL-2000 CAL, Ocean Optics) that was coupled to the delivery fiber (QP200-2-VIS-BX, Ocean Optics). Note that this delivery fiber will start to absorb heavily beyond 2500 nm (and slightly below 400 nm). The attenuation with a ND2 (BK7 substrate) reflection filter was also calibrated externally by a photo spectrometer. It is used to not saturate the spectrometers or damage the delivery fiber.

The HCF output was collimated using a concave silver mirror and its on-axis part was sent on the multimode fiber which is coupled to both spectrometers sequentially for each measurement point. Note that the input face of the 200 μm delivery fiber diameter will couple relatively more short wavelength light inside the spectrometers due to different mode diameters over the broad bandwidth. This linear factor in coupling to the spectrometers was compensated for in the spectra shown in fig. 7.8. VIS and NIR spectrometers were both corrected for their sensitivity as mentioned above and their spectra are stitched together around 1 μm . However, in the UV the calibration is limited by the very low sensitivity and the consequently high noise.

C.2.1 Additional diagnostics

Both spectrometers (VIS and NIR) together could still not completely cover the whole bandwidth, thus for looking at the edges of our spectrum in the UV, a Maya2000 (Ocean Optics) spectrometer was used to visualize the fifth harmonic of the OPCPA. Unfortunately it could not be calibrated to the other spectrometers, since our calibration source did not emit enough UV components. Also an uncalibrated PbSe spectrometer was used without delivery fiber to find the cut-off at long wave-lengths around 2.7 μm , possibly cut by the ND2 (BK7 substrate) reflective filter.

Appendix D

Self-diffraction in QPM OPCPA

As pointed out in section 5.4, for high intensities in degenerate quasi-phase-matched OPCPA, the back-conversion of the signal and idler to pump wavelengths can distort the phase of the compressed signal. Nicholas Karpowicz simulated the behavior in the OPCPA, his results are briefly shown here to compare with the actual amplified and compressed pulse of section 5.4. Figure D.1 shows spectrograms of the IR OPCPA of chapter 5 with increasing pump intensity (the values chosen here are lower than in the actual OPCPA, due to the simple nature of the 1D simulation). It is obvious that some reconversion into the second harmonic appears for higher signal intensities. Therefore the signal spectrum starts to exhibit a hole (see fig. D.2). With the hole depth, the spectral phase also shows a discontinuity, as in the compressed pulse of the OPCPA in fig. 5.7. When comparing both, the sign of the spectral phase seems to be correct, so the time axis in fig. 5.7 (that is not determined in the reconstruction of a SHG FROG) is confirmed. Even the magnitude of the phase jump for a complete spectral hole (like retrieved in fig. 5.8 or measured in the second stage in fig. 5.5), is reconstructed for about 30 GW/cm^2 in fig. D.2. Simultaneously the spectral amplitude is becoming more modulated. The second harmonic of the signal was also detected in the experiment (see fig. 7.5, here cut because of silicon absorption, see fig. B.2).

Note that the diverging phase for short-wavelength components in fig. D.2 is caused by the optical parametric phase, that follows the phase mismatch [27], shown in fig. 1.3. In fig. 5.8 this is compensated by the applied Dazzler polynomial phase. For wavelengths up to $3 \mu\text{m}$, the phase mismatch is rather low.

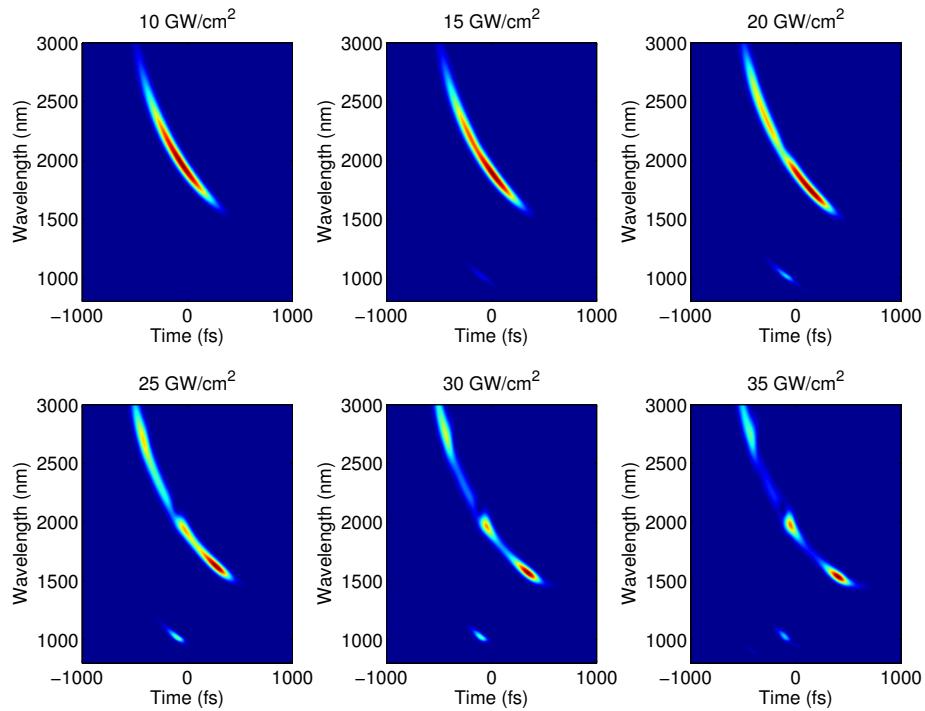


Figure D.1: Spectrograms of saturated amplification in QPM OPCPA.

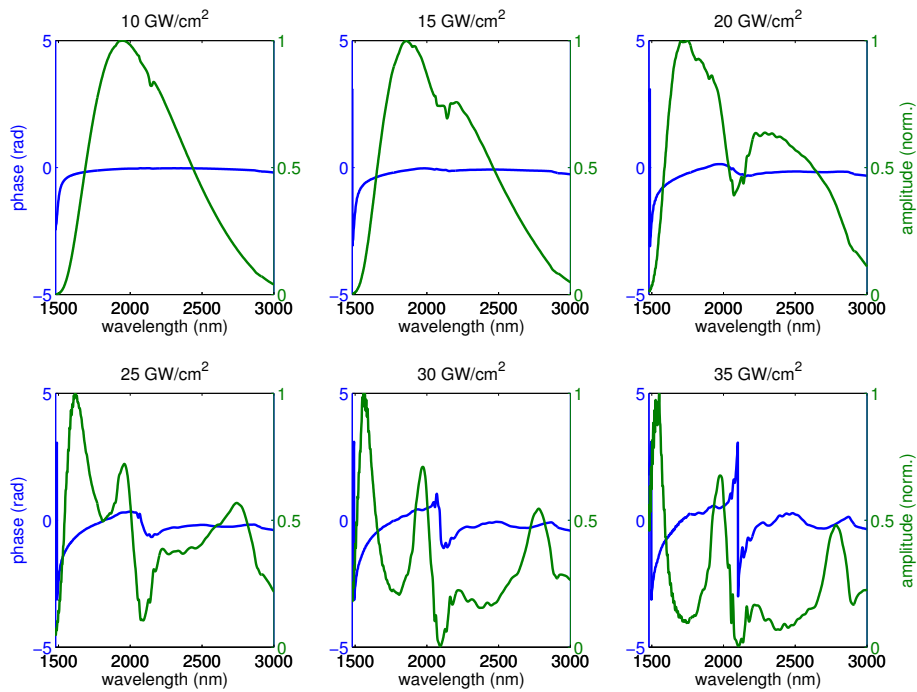


Figure D.2: Spectral phase and amplitude of signal in QPM OPCPA when saturated.

Data archiving

The data shown and discussed in this thesis can be found on the Data Archive Server (DAS) at the Max Planck Institute for Quantum Optics, Division for Attosecond Physics.

In the list of figures one can find the respective folder name in brackets. Every single folder contains exactly one Matlab script to reproduce the figure (the rest are dependencies) and all necessary data. Most of the data is kept as raw data (sometimes as `.mat` or `.zip` files to save space and in very rare cases even proprietary file formats could not be avoided). All data manipulation is performed by Matlab scripts and therefore easily reproducible. Often Matlab even generates the `.pdf`-figure directly (otherwise the `.fig`-file was converted to `.pdf` manually). Loading the script and pressing **F5** should reproduce almost all figures. Otherwise, a `readme.txt`, provides further information.

Matlab R2011a and LabView 8.6/2012 were used, as well as the Matlab libraries of Xun Gu and Nicholas Karpowicz.

Bibliography

- [1] N. Aközbek, A. Becker, M. Scalora, S. Chin und C. Bowden, *Applied Physics B* **77** (2003), 177.
- [2] J.A. Armstrong, *Applied Physics Letters* **10** (1967), 16.
- [3] A. Baltuska, M. Pshenichnikov und D. Wiersma. In *Frequency-Resolved Optical Gating: The Measurement of Ultrashort Laser Pulses*. Springer US (2000), Seiten 257–303.
- [4] A. Baltuska, M. Uiberacker, E. Goulielmakis, R. Kienberger, V. Yakovlev, T. Udem, T. Hansch und F. Krausz, *Selected Topics in Quantum Electronics, IEEE Journal of* **9** (2003), 972.
- [5] A. Baltuška, T. Fuji und T. Kobayashi, *Opt. Lett.* **27** (2002), 306.
- [6] H.C. Bandulet, D. Comtois, A.D. Shiner, C. Trallero-Herrero, N. Kajumba, T. Ozaki, P.B. Corkum, D.M. Villeneuve, J.C. Kieffer und F. Légaré, *Journal of Physics B: Atomic, Molecular and Optical Physics* **41** (2008), 245602.
- [7] M.G. Benedict und P. Földi, *Physica Scripta* **2013** (2013), 014005.
- [8] Bergmann Messgeräte Entwicklung KG, Murnau, Germany. *Digital Delay/Pulse Generator Model BME_SG02p*.
- [9] T. Binhammer, E. Rittweger, R. Ell, F. Kärtner und U. Morgner, *Quantum Electronics, IEEE Journal of* **41** (2005), 1552.
- [10] J.R. Birge, R. Ell und F.X. Kärtner, *Opt. Lett.* **31** (2006), 2063.
- [11] R.W. Boyd: *Nonlinear Optics*. Academic Press; third edition, 2008.
- [12] M. Bradler, P. Baum und E. Riedle, *Applied Physics B* **97** (2009), 561.
- [13] A. Braun, G. Korn, X. Liu, D. Du, J. Squier und G. Mourou, *Opt. Lett.* **20** (1995), 73.
- [14] D. Brida, S. Bonora, C. Manzoni, M. Marangoni, P. Villoresi, S.D. Silvestri und G. Cerullo, *Opt. Express* **17** (2009), 12510.
- [15] J. Bromage, J. Rothhardt, S. Hädrich, C. Dorrer, C. Jocher, S. Demmler, J. Limpert, A. Tünnermann und J.D. Zuegel, *Opt. Express* **19** (2011), 16797.

- [16] F. Calegari, C. Vozzi, M. Negro, G. Sansone, F. Frassetto, L. Poletto, P. Villoresi, M. Nisoli, S.D. Silvestri und S. Stagira, *Opt. Lett.* **34** (2009), 3125.
- [17] A.L. Cavalieri, E. Goulielmakis, B. Horvath, W. Helml, M. Schultze, M. Fieß, V. Pervak, L. Veisz, V.S. Yakovlev, M. Uiberacker, A. Apolonski, F. Krausz und R. Kienberger, *New Journal of Physics* **9** (2007), 242.
- [18] A.L. Cavalieri, E. Goulielmakis, B. Horvath, W. Helml, M. Schultze, M. Fieß, V. Pervak, L. Veisz, V.S. Yakovlev, M. Uiberacker, A. Apolonski, F. Krausz und R. Kienberger, *New Journal of Physics* **9** (2007), 242.
- [19] G. Cerullo, A. Baltuska, O. Mücke und C. Vozzi, *Laser & Photonics Reviews* **5** (2011), 323.
- [20] V. Chauhan, P. Bowlan, J. Cohen und R. Trebino, *J. Opt. Soc. Am. B* **27** (2010), 619.
- [21] X. Chen, A. Jullien, A. Malvache, L. Canova, A. Borot, A. Trisorio, C.G. Durfee und R. Lopez-Martens, *Opt. Lett.* **34** (2009), 1588.
- [22] X. Chen, X. Li, J. Liu, P. Wei, X. Ge, R. Li und Z. Xu, *Opt. Lett.* **32** (2007), 2402.
- [23] P.G. Chua, Y. Tanaka, M. Takeda und T. Kurokawa: *Infra-red image detection with a Si-CCD image sensor due to the two-photon absorption process. Infra-red image detection with a Si-CCD image sensor due to the two-photon absorption process*, In *Lasers and Electro-Optics, 2001. CLEO/Pacific Rim 2001. The 4th Pacific Rim Conference on*, Band 1. (July 2001) Seiten I–I.
- [24] K. Cook, A. Kar und R.A. Lamb, *Opt. Express* **13** (2005), 2025.
- [25] A. Couairon und A. Mysyrowicz, *Physics Reports* **441** (2007), 47 .
- [26] R. Danielius, G.P. Banfi, P.D. Trapani, A. Dubietis, A. Piskarskas und D. Podenas, *Opt. Lett.* **18** (1993), 574.
- [27] S. Demmler, J. Rothhardt, S. Hädrich, J. Bromage, J. Limpert und A. Tünnermann, *Opt. Lett.* **37** (2012), 3933.
- [28] Y. Deng, A. Schwarz, H. Fattahi, M. Ueffing, X. Gu, M. Ossiander, T. Metzger, V. Pervak, H. Ishizuki, T. Taira, T. Kobayashi, G. Marcus, F. Krausz, R. Kienberger und N. Karpowicz, *Opt. Lett.* **37** (2012), 4973.
- [29] J. Dörring, A. Killi, U. Morgner, A. Lang, M. Lederer und D. Kopf, *Opt. Express* **12** (2004), 1759.
- [30] J. Dura, N. Camus, A. Thai, A. Britz, M. Hemmer, M. Baudisch, A. Senftleben, C.D. Schroter, J. Ullrich, R. Moshhammer und J. Biegert, *Sci. Rep.* **3** (2013), .
- [31] Fastlite, Valbonne Sophia Antipolis, France. *DAZZLER Systems: Operating Manual* (March 2005).

- [32] Fastlite, Valbonne Sophia Antipolis, France. *DAZZLER Systems: Low Jitter operation* (March 2006).
- [33] Fastlite, Valbonne Sophia Antipolis, France. *DAZZLER systems: Theoretical overview of the Dazzler Device* (March 2006).
- [34] H. Fattahi, A. Schwarz, S. Keiber und N. Karpowicz, *Opt. Lett.* **38** (2013), 4216.
- [35] H. Fattahi, C. Skrobol, M. Ueffing, Y. Deng, A. Schwarz, Y. Kida, V. Pervak, T. Metzger, Z. Major und F. Krausz: *High efficiency, multi-mJ, sub 10 fs, optical parametric amplifier at 3 kHz. High efficiency, multi-mJ, sub 10 fs, optical parametric amplifier at 3 kHz*, In *Conference on Lasers and Electro-Optics 2012*. Optical Society of America (2012) Seite CTh1N.6.
- [36] H. Fattahi, C.Y. Teisset, O. Pronin, A. Sugita, R. Graf, V. Pervak, X. Gu, T. Metzger, Z. Major, F. Krausz und A. Apolonski, *Opt. Express* **20** (2012), 9833.
- [37] T. Fordell, M. Miranda, A. Persson und A. L’Huillier, *Opt. Express* **17** (2009), 21091.
- [38] R. Ganeev, I. Kulagin, A. Ryasnyansky, R. Tugushev und T. Usmanov, *Optics Communications* **229** (2004), 403 .
- [39] A. Giesen, H. Hügel, A. Voss, K. Wittig, U. Brauch und H. Opower, *Applied Physics B: Lasers and Optics* **58** (1994), 365. 10.1007/BF01081875.
- [40] E. Goulielmakis, M. Uiberacker, R. Kienberger, A. Baltuska, V. Yakovlev, A. Scrinzi, T. Westerwalbesloh, U. Kleineberg, U. Heinzmann, M. Drescher und F. Krausz, *Science* **305** (2004), 1267.
- [41] U. Graf, M. Fieß, M. Schultze, R. Kienberger, F. Krausz und E. Goulielmakis, *Opt. Express* **16** (2008), 18956.
- [42] E. Granados, L.J. Chen, C.J. Lai, K.H. Hong und F.X. Kärtner, *Opt. Express* **20** (2012), 9099.
- [43] M.A. Green, *Solar Energy Materials and Solar Cells* **92** (2008), 1305 .
- [44] M. Grishin, V. Gulbinas und A. Michailovas, *Opt. Express* **15** (2007), 9434.
- [45] X. Gu: *Measuring Ultracomplex Supercontinuum Pulses and Spatio-Temporal Distortions*. Georgia Institute of Technology, Dissertation, 2004.
- [46] X. Gu, G. Marcus, Y. Deng, T. Metzger, C. Teisset, N. Ishii, T. Fuji, A. Baltuska, R. Butkus, V. Pervak, H. Ishizuki, T. Taira, T. Kobayashi, R. Kienberger und F. Krausz, *Opt. Express* **17** (2009), 62.
- [47] A. Guggenmos, R. Rauhut, M. Hofstetter, S. Hertrich, B. Nickel, J. Schmidt, E.M. Gullikson, M. Seibald, W. Schnick und U. Kleineberg, *Opt. Express* **21** (2013), 21728.
- [48] S. Hädrich, J. Rothhardt, M. Krebs, S. Demmler, J. Limpert und A. Tünnermann, *Opt. Lett.* **37** (2012), 4910.

- [49] A. Harth, M. Schultze, T. Lang, T. Binhammer, S. Rausch und U. Morgner, *Opt. Express* **20** (2012), 3076.
- [50] M.T. Hassan, A. Wirth, I. Grguraš, A. Moulet, T.T. Luu, J. Gagnon, V. Pervak und E. Goulielmakis, *Review of Scientific Instruments* **83** (2012), 111301.
- [51] P. Heissler: *Relativistic Laser Plasma Interaction: A Novel Route to Intense, Single Attosecond Pulses*. Fakultät für Physik Ludwig-Maximilians-Universität München, Dissertation, 2012.
- [52] M. Hemmer, M. Baudisch, A. Thai, A. Couairon und J. Biegert, *Opt. Express* **21** (2013), 28095.
- [53] M. Hentschel, R. Kienberger, C. Spielmann, G.A. Reider, N. Milosevic, T. Brabec, P. Corkum, U. Heinzmann, M. Drescher und F. Krausz, *Nature* **414** (2001), 509.
- [54] D. Herrmann, L. Veisz, R. Tautz, F. Tavella, K. Schmid, V. Pervak und F. Krausz, *Opt. Lett.* **34** (2009), 2459.
- [55] C. Homann, M. Bradler, M. Förster, P. Hommelhoff und E. Riedle, *Opt. Lett.* **37** (2012), 1673.
- [56] C. Homann und E. Riedle, *Laser & Photonics Reviews* **7** (2013), 580.
- [57] K.H. Hong, A. Siddiqui, J. Moses, J. Gopinath, J. Hybl, F. Ömer Ilday, T.Y. Fan und F.X. Kärtner, *Opt. Lett.* **33** (2008), 2473.
- [58] S.W. Huang, G. Cirmi, J. Moses, K.H. Hong, S. Bhardwaj, J.R. Birge, L.J. Chen, I.V. Kabakova, E. Li, B.J. Eggleton, G. Cerullo und F.X. Kärtner, *Journal of Physics B: Atomic, Molecular and Optical Physics* **45** (2012), 074009.
- [59] S.W. Huang, G. Cirmi, J. Moses, K.H. Hong, S. Bhardwaj, J.R. Birge, L.J. Chen, E. Li, B.J. Eggleton, G. Cerullo und F.X. Kärtner, *Nat Photon* **5** (2011), 475.
- [60] C. Iaconis und I. Walmsley, *Opt. Lett.* **23** (1998), 792.
- [61] N. Ishii, S. Adachi, Y. Nomura, A. Kosuge, Y. Kobayashi, T. Kanai, J. Itatani und S. Watanabe, *Opt. Lett.* **37** (2012), 97.
- [62] N. Ishii, C. Teisset, T. Fuji, S. Kohler, K. Schmid, L. Veisz, A. Baltuska und F. Krausz, *Selected Topics in Quantum Electronics, IEEE Journal of* **12** (2006), 173 .
- [63] H. Ishizuki und T. Taira, *Opt. Express* **20** (2012), 20002.
- [64] D.J. Jones, E.O. Potma, J.x. Cheng, B. Burfeindt, Y. Pang, J. Ye und X.S. Xie, *Review of Scientific Instruments* **73** (2002), 2843 .
- [65] T. Kanai, A. Suda, S. Bohman, M. Kaku, S. Yamaguchi und K. Midorikawa, *Applied Physics Letters* **92** (2008), 061106.
- [66] D. Kane und R. Trebino, *Quantum Electronics, IEEE Journal of* **29** (1993), 571.

- [67] S. Kane und J. Squier, *Quantum Electronics, IEEE Journal of* **31** (1995), 2052.
- [68] D. Kartashov, S. Ališauskas, A. Pugžlys, A. Voronin, A. Zheltikov, M. Petrarca, P. Béjot, J. Kasparian, J.P. Wolf und A. Baltuška, *Opt. Lett.* **37** (2012), 3456.
- [69] R. Kienberger, E. Goulielmakis, M. Uiberacker, A. Baltuska, V. Yakovlev, F. Bammer, A. Scrinzi, T. Westerwalbesloh, U. Kleineberg, U. Heinzmann, M. Drescher und F. Krausz, *Nature* **427** (2004), 817.
- [70] J. Kim, J. Chen, Z. Zhang, F.N.C. Wong, F.X. Kärtner, F. Loehl und H. Schlarb, *Opt. Lett.* **32** (2007), 1044.
- [71] K.T. Kim, C. Zhang, A.D. Shiner, B.E. Schmidt, F. Legare, V. M. und C. B., *Nat Photon* **7** (2013), 958.
- [72] S. Klingebiel: *Picosecond pump dispersion management and jitter stabilization in a petawatt-scale few-cycle OPCPA system*. Ludwig-Maximilians-Universität München, Dissertation, 2013.
- [73] S. Klingebiel, I. Ahmad, C. Wandt, C. Skrobol, S.A. Trushin, Z. Major, F. Krausz und S. Karsch, *Opt. Express* **20** (2012), 3443.
- [74] S. Klingebiel, C. Wandt, C. Skrobol, I. Ahmad, S.A. Trushin, Z. Major, F. Krausz und S. Karsch, *Opt. Express* **19** (2011), 5357.
- [75] W.H. Knox, R.L. Fork, M.C. Downer, R.H. Stolen, C.V. Shank und J.A. Valdmanis, *Applied Physics Letters* **46** (1985), 1120.
- [76] W. Koechner: *Solid-State Laser Engineering*. Springer, New York, 2006.
- [77] S. Koke, C. Grebing, B. Manschwetus und G. Steinmeyer, *Opt. Lett.* **33** (2008), 2545.
- [78] F. Krausz und M. Ivanov, *Rev. Mod. Phys.* **81** (2009), 163.
- [79] N. Krebs, R.A. Probst und E. Riedle, *Opt. Express* **18** (2010), 6164.
- [80] S.Y. Kruchinin, M. Korbman und V.S. Yakovlev, *Phys. Rev. B* **88** (2013), 079904.
- [81] M. Kruger, M. Schenk und P. Hommelhoff, *Nature* **475** (2011), 78.
- [82] C. Li, D. Wang, L. Song, J. Liu, P. Liu, C. Xu, Y. Leng, R. Li und Z. Xu, *Opt. Express* **19** (2011), 6783.
- [83] H. Li, C. Kam, Y. Lam und W. Ji, *Optical Materials* **15** (2001), 237 .
- [84] E.A.J. Marcatili und R.A. Schmelzter, *Bell Syst. Tech. J.* **43** (1964), 1783.
- [85] O. Martinez, *Quantum Electronics, IEEE Journal of* **23** (1987), 59 .
- [86] E. Matsubara, K. Yamane, T. Sekikawa und M. Yamashita, *J. Opt. Soc. Am. B* **24** (2007), 985.

- [87] T. Metzger: *High-repetition-rate picosecond pump laser based on an Yb:YAG disk amplifier for optical parametric amplification*. Berlin, TU Berlin, Dissertation, 2009.
- [88] T. Metzger, A. Schwarz, C.Y. Teisset, D. Sutter, A. Killi, R. Kienberger und F. Krausz, *Opt. Lett.* **34** (2009), 2123.
- [89] T. Miura, K. Kobayashi, K. Takasago, Z. Zhang, K. Torizuka und F. Kannari, *Opt. Lett.* **25** (2000), 1795.
- [90] J. Moses, S.W. Huang, K.H. Hong, O.D. Mücke, E.L.F. ao Filho, A. Benedick, F.O. Ilday, A. Dergachev, J.A. Bolger, B.J. Eggleton und F.X. Kärtner, *Opt. Lett.* **34** (2009), 1639.
- [91] J. Moses, C. Manzoni, S.W. Huang, G. Cerullo und F.X. Kaertner, *Opt. Express* **17** (2009), 5540.
- [92] G.A. Mourou, T. Tajima und S.V. Bulanov, *Rev. Mod. Phys.* **78** (2006), 309.
- [93] D. Müller: *Pulsenergiestabilität bei regenerativen Kurzpulsverstärkern im Scheibenlaserdesign*. Universität Stuttgart, Dissertation, 2005.
- [94] M. Nisoli, S.D. Silvestri und O. Svelto, *Applied Physics Letters* **68** (1996), 2793.
- [95] K. Okamura und T. Kobayashi, *Opt. Lett.* **36** (2011), 226.
- [96] P. O'Shea, M. Kimmel, X. Gu und R. Trebino, *Opt. Express* **7** (2000), 342.
- [97] T. Paasch-Colberg: *Ultrafast, optical-field-induced currents in solid-state materials*. Technische Universität München, Dissertation, 2014.
- [98] T. Paasch-Colberg, A. Schiffrin, N. Karpowicz, S. Kruchinin, SaglamOzge, S. Keiber, O. Razskazovskaya, S. Muhlbrandt, A. Alnaser, M. Kubel, V. Apalkov, D. Gerster, J. Reichert, T. Wittmann, J.V. Barth, M.I. Stockman, R. Ernstorfer, V.S. Yakovlev, R. Kienberger und F. Krausz, *Nat Photon* **8** (2014), 214.
- [99] R. Paschotta, *Opt. Express* **14** (2006), 6069.
- [100] R. Paschotta. *RP Photonics Encyclopedia - Carrier envelope Offset*. http://www.rp-photonics.com/carrier_envelope_offset.html (January 2014).
- [101] S. Piehler, B. Weichelt, A. Voss, M.A. Ahmed und T. Graf, *Opt. Lett.* **37** (2012), 5033.
- [102] T. Popmintchev, M.C. Chen, D. Popmintchev, P. Arpin, S. Brown, S. Alisauskas, G. Andriukaitis, T. Balciunas, O.D. Mücke, A. Pugzlys, A. Baltuska, B. Shim, S.E. Schrauth, A. Gaeta, C. Hernandez-Garcia, L. Plaja, A. Becker, A. Jaron-Becker, M.M. Murnane und H.C. Kapteyn, *Science* **336** (2012), 1287.
- [103] A. Pugžlys, G. Andriukaitis, A. Baltuška, L. Su, J. Xu, H. Li, R. Li, W.J. Lai, P.B. Phua, A. Marcinkevičius, M.E. Fermann, L. Giniūnas, R. Danielius und S. Ališauskas, *Opt. Lett.* **34** (2009), 2075.

- [104] S. Rausch, T. Binhammer, A. Harth, F.X. Kärtner und U. Morgner, *Opt. Express* **16** (2008), 17410.
- [105] S. Rausch, T. Binhammer, A. Harth, J. Kim, R. Ell, F.X. Kärtner und U. Morgner, *Opt. Express* **16** (2008), 9739.
- [106] F. Reynaud, F. Salin und A. Barthelemy, *Opt. Lett.* **14** (1989), 275.
- [107] M. Rhodes, G. Steinmeyer, J. Ratner und R. Trebino, *Laser & Photonics Reviews* **7** (2013), 557.
- [108] R. Riedel, M. Schulz, M.J. Prandolini, A. Hage, H. Höppner, T. Gottschall, J. Limpert, M. Drescher und F. Tavella, *Opt. Express* **21** (2013), 28987.
- [109] F. Röser, T. Eidam, J. Rothhardt, O. Schmidt, D.N. Schimpf, J. Limpert und A. Tünnermann, *Opt. Lett.* **32** (2007), 3495.
- [110] I.N. Ross, P. Matousek, G.H.C. New und K. Osvay, *J. Opt. Soc. Am. B* **19** (2002), 2945.
- [111] J. Rothhardt, S. Demmler, S. Hädrich, J. Limpert und A. Tünnermann, *Opt. Express* **20** (2012), 10870.
- [112] P. Russbuedt, T. Mans, G. Rotarius, J. Weitenberg, H.D. Hoffmann und R. Poprawe, *Opt. Express* **17** (2009), 12230.
- [113] T.R. Schibli, J. Kim, O. Kuzucu, J.T. Gopinath, S.N. Tandon, G.S. Petrich, L.A. Kolodziejski, J.G. Fujimoto, E.P. Ippen und F.X. Kärtner, *Opt. Lett.* **28** (2003), 947.
- [114] A. Schiffrin, T. Paasch-Colberg, N. Karpowicz, V. Apalkov, D. Gerster, S. Muhlbrandt, M. Korbman, J. Reichert, M. Schultze, S. Holzner, J.V. Barth, R. Kienberger, R. Ernstorfer, V.S. Yakovlev, M.I. Stockman und F. Krausz, *Nature* **493** (2013), 70.
- [115] B.E. Schmidt, A.D. Shiner, P. Lassonde, J.C. Kieffer, P.B. Corkum, D.M. Villeneuve und F. Légaré, *Opt. Express* **19** (2011), 6858.
- [116] O. Schubert, M. Hohenleutner, F. Langer, B. Urbanek, C. Lange, U. Huttner, D. Golde, T. Meier, M. Kira, S. Koch und R. Huber, *Nat Photon* **8** (2014), 119.
- [117] M. Schultze, M. Fieß, N. Karpowicz, J. Gagnon, M. Korbman, M. Hofstetter, S. Neppl, A.L. Cavalieri, Y. Komninos, T. Mercouris, C.A. Nicolaides, R. Pazourek, S. Nagele, J. Feist, J. Burgdörfer, A.M. Azzeer, R. Ernstorfer, R. Kienberger, U. Kleineberg, E. Goulielmakis, F. Krausz und V.S. Yakovlev, *Science* **328** (2010), 1658.
- [118] M. Schulz, R. Riedel, A. Willner, T. Mans, C. Schnitzler, P. Russbuedt, J. Dolkemeyer, E. Seise, T. Gottschall, S. Hädrich, S. Duesterer, H. Schlarb, J. Feldhaus, J. Limpert, B. Faatz, A. Tünnermann, J. Rossbach, M. Drescher und F. Tavella, *Opt. Lett.* **36** (2011), 2456.
- [119] A. Schwarz, M. Ueffing, Y. Deng, X. Gu, H. Fattahi, T. Metzger, M. Ossiander, F. Krausz und R. Kienberger, *Opt. Express* **20** (2012), 5557.

- [120] W. Schweinberger, A. Sommer, E. Bothschafter, J. Li, F. Krausz, R. Kienberger und M. Schultze, *Opt. Lett.* **37** (2012), 3573.
- [121] E. Seres, J. Seres und C. Spielmann, *Applied Physics Letters* **89** (2006), .
- [122] A.D. Shiner, C. Trallero-Herrero, N. Kajumba, H.C. Bandulet, D. Comtois, F. Légaré, M. Giguère, J.C. Kieffer, P.B. Corkum und D.M. Villeneuve, *Phys. Rev. Lett.* **103** (2009), 073902.
- [123] T. Siegel, R. Torres, D.J. Hoffmann, L. Brugnera, I. Procino, A. Zaïr, J.G. Underwood, E. Springate, I.C.E. Turcu, L.E. Chipperfield und J.P. Marangos, *Opt. Express* **18** (2010), 6853.
- [124] F. Silva, D. Austin, A. Thai, M. Baudisch, M. Hemmer, D. Faccio, A. Couairon und J. Biegert, *Nat Commun* **3** (2012), 807.
- [125] F. Silva, P.K. Bates, A. Esteban-Martin, M. Ebrahim-Zadeh und J. Biegert, *Opt. Lett.* **37** (2012), 933.
- [126] S. Skupin und L. Bergé, *Optics Communications* **280** (2007), 173 .
- [127] J. Speiser, *J. Opt. Soc. Am. B* **26** (2009), 26.
- [128] Stanford Research Systems, Sunnyvale, CA, USA. *Digital Delay/Pulse Generator DG645*.
- [129] G. Steinmeyer und G. Stibenz, *Applied Physics B* **82** (2006), 175.
- [130] A. Stingl, M. Lenzner, C. Spielmann, F. Krausz und R. Szipöcs, *Opt. Lett.* **20** (1995), 602.
- [131] D. Strickland und G. Mourou, *Optics Communications* **56** (1985), 219 .
- [132] B.C. Stuart, M.D. Feit, S. Herman, A.M. Rubenchik, B.W. Shore und M.D. Perry, *Phys. Rev. B* **53** (1996), 1749.
- [133] R.L. Sutherland: *Handbook of Nonlinear Optics*. CRC Press; 2 edition, 2003.
- [134] F. Tavella, Y. Nomura, L. Veisz, V. Pervak, A. Marcinkevičius und F. Krausz, *Opt. Lett.* **32** (2007), 2227.
- [135] C. Teisset, M. Schultze, R. Bessing, M. Haefner, S. Prinz, D. Sutter und T. Metzger: *300 W Picosecond Thin-Disk Regenerative Amplifier at 10 kHz Repetition Rate. 300 W Picosecond Thin-Disk Regenerative Amplifier at 10 kHz Repetition Rate*, In *Advanced Solid-State Lasers Congress Postdeadline*. Optical Society of America (2013) Seite JTh5A.1.
- [136] A. Thai, M. Hemmer, P.K. Bates, O. Chalus und J. Biegert, *Opt. Lett.* **36** (2011), 3918.
- [137] W.J. Tomlinson, R.H. Stolen und C.V. Shank, *J. Opt. Soc. Am. B* **1** (1984), 139.
- [138] R. Trebino: *Frequency-Resolved Optical Gating: The Measurement of Ultrashort Laser Pulses*. Kluwer Academic Publishers, 2002.

-
- [139] R. Trebino, K.W. DeLong, D.N. Fittinghoff, J.N. Sweetser, M.A. Krumbügel, B.A. Richman und D.J. Kane, *Review of Scientific Instruments* **68** (1997), 3277.
- [140] M. Ueffing: *A Sub-50-fs Pulse Synchronization System for Pump and Seed Pulses of an OPCPA System*. Technische Universitaet Muenchen, Diplomarbeit, 2011.
- [141] K.F. Wall und A. Sanchez, *The Lincoln Laboratory Journal* **3** (1990), 447.
- [142] H. Wang, M. Chini, E. Moon, H. Mashiko, C. Li und Z. Chang, *Opt. Express* **17** (2009), 12082.
- [143] A. Weiner, *Review of Scientific Instruments* **71** (2000), 1929.
- [144] D. Yoshitomi, X. Zhou, Y. Kobayashi, H. Takada und K. Torizuka, *Opt. Express* **18** (2010), 26027.
- [145] X. Zhang, E. Schneider, G. Taft, H. Kaptyen, M. Murnane und S. Backus, *Opt. Express* **20** (2012), 7015.

Acknowledgments

First of all, I want to thank my doctoral adviser Prof. Ferenc Krausz for giving me the opportunity to work as a PhD student in such an outstanding environment. I also want to thank him for his great encouragement and support which he gave even though the group has grown strongly over the past years and for giving LWS 1 the chance to blossom at last despite all obstacles (that unfortunately delayed my thesis quite a bit).

Second, Nick Karpowicz provided an incredible amount of advice, ideas and simulations. Without his theoretical and experimental knowledge, the material for this thesis certainly could not have been collected.

Special thanks go to Prof. Reinhard Kienberger and Zsuzsanna Major, my former direct supervisors, for their efforts.

I would like to thank my former Postdoc Yunpei Deng, who performed many the experiments with me. My doctoral work would have certainly not been possible without all of his support and endurance in the lab.

I should not forget the support from two former Postdocs that left the group quite some time ago; unfortunately the period spent with Xun Gu and Gilad Marcus in the lab was limited, but I learned a lot from both of them and enjoyed working and discussing with these real world-class researchers. Xun started (and later advised) the synchronization work described in this thesis and both helped compressing LWS 1.

I also enjoyed the first six months of my work at MPQ very much, working with Thomas Metzger on the pump laser of chapter 3 and learning a lot from him. Without his endless believe and effort in the thin-disk laser as a pump for OPCPA, LWS 1 would have never worked the way it performs today.

I would like to thank Hanieh Fattahi, the best colleague ever, for the time we worked together in the lab fixing the disk laser, on the amplification stages of LWS 1, the prototype of LWS pro and the broadening of both the disk laser and FP 2 spectra.

Sabine Keiber and Xiaotao Geng helped me perform both the current control experiment of chapter 6 and the superoctave continuum generation of chapter 7.

Moritz Ueffing and I also spent many long hours in the lab. His optical synchronization setup pathed the way for the OPCPA system of this thesis and probably for some more to come. I would like to thank him for all the efforts he invested as a diploma student in realizing this idea and assisting Yunpei and me at LWS 1.

Marcus Ossiander for being an incredibly patient, gifted and motivated working student in the lab, helping us at LWS 1 with LabView and Matlab programming and building some nice optical and electronic devices that we use every day.

Wolfgang Schweinberger, as the only other laser guy in the attosecond group, provided lots of advice on the HCF broadening and the Dazzler.

Very crucial was the support from Wolfi and Martin, getting FP 2 in great shape, supporting the broadening of FP 2 spectrum and the HHG experiment (that unfortunately could not be pursued in my thesis time any more).

Prof. Kienberger, Florian and Stefan for helping with drying the thin-disk laser after an unintended abundance of cooling water in it. Bidoor Al Saif, Lauryna Lötscher and Thomas Ganz for the time together in the lab working on the prototype of LWS pro and the broadening of the disk laser spectrum.

Patrick, Mohammad, Michael, Alexander, Daniel and Tim for being great office mates. Adrian Cavalleri, Elisabeth Magerl, Elisabeth Bothschafter, Markus Fieß, Rosi, Agustin, Konrad, Simon, Annkathrin, Tobias, Johann and Martin (in chronological order) for the nice working atmosphere in the lab.

Finally Manfred Fischer, Anton Horn, Harald Haas, Alois Böswald and Tobias Kleinhenz have given me great technical support.

For the illustrations, the component library of Alexander Franzen (http://www.gwoptics.org/component_library/) was used.

Curriculum Vitae of Alexander Schwarz

Personal

Date of birth 6th May 1984, Schrobenhausen, Germany
Citizenship German
Postal address Max Planck Institute of Quantum Optics
Hans Kopfermann Str. 1
85748 Garching
Telephone +49-89-32905-331
eMail alexander.schwarz@mpq.mpg.de

Education

- Summer 2008 –present PhD candidate in the group of Prof. F. Krausz in the framework of the International Max Planck Research School on Advanced Photon Science
Max Planck Institute of Quantum Optics, Garching, Germany
- Summer 2008 M.S. in Physics, GPA: 3.8
University of New Mexico, Albuquerque, NM, USA
Master thesis: "Femtosecond Laguerre-Gaussian beams"
directed by Professor W. Rudolph
- Fall 2006 –Summer 2008 graduate studies in Physics
University of New Mexico, Albuquerque, NM, USA
- Fall 2005 –Summer 2006 graduate studies in Physics
Universität Würzburg, Würzburg, Germany
- Fall 2003 –Summer 2005 Vordiplom in Physics
Universität Würzburg, Würzburg, Germany, grade: 1.25
- Summer 2003 Abitur at Gymnasium Donauwörth, grade: 2.0